

2020-01-01

Uranium Series Dating And Geochemistry Of Fault Zone Precipitated Secondary Carbonates: Insights Into Paleo Fluid Sources, Tectonics And Climate In The Rio Grande Rift

Victor Higareda Garcia
University of Texas at El Paso

Follow this and additional works at: https://scholarworks.utep.edu/open_etd



Part of the [Geochemistry Commons](#), and the [Geology Commons](#)

Recommended Citation

Garcia, Victor Higareda, "Uranium Series Dating And Geochemistry Of Fault Zone Precipitated Secondary Carbonates: Insights Into Paleo Fluid Sources, Tectonics And Climate In The Rio Grande Rift" (2020). *Open Access Theses & Dissertations*. 2968.
https://scholarworks.utep.edu/open_etd/2968

This is brought to you for free and open access by ScholarWorks@UTEP. It has been accepted for inclusion in Open Access Theses & Dissertations by an authorized administrator of ScholarWorks@UTEP. For more information, please contact lweber@utep.edu.

URANIUM SERIES DATING AND GEOCHEMISTRY OF FAULT ZONE PRECIPITATED
SECONDARY CARBONATES: INSIGHTS INTO PALEO FLUID SOURCES, TECTONICS
AND CLIMATE IN THE RIO GRANDE RIFT

VICTOR HIGAREDA GARCIA

Doctoral Program in Geological Sciences

APPROVED:

Lin Ma, Ph.D., Chair

Jason W. Ricketts, Ph.D., Co-Chair

Aaron A. Velasco, Ph.D.

Terry L. Pavlis, Ph.D.

Craig E. Tweedie, Ph.D.

Stephen L. Crites, Jr., Ph.D.
Dean of the Graduate School

Copyright ©

by

Victor Higareda Garcia

2020

Dedication

I dedicate this dissertation to my family, friends, and my wife.

URANIUM SERIES DATING AND GEOCHEMISTRY OF FAULT ZONE PRECIPITATED
SECONDARY CARBONATES: INSIGHTS INTO PALEO FLUID SOURCES, TECTONICS
AND CLIMATE IN THE RIO GRANDE RIFT

by

VICTOR HIGAREDA GARCIA, B.S., M.S.

DISSERTATION

Presented to the Faculty of the Graduate School of
The University of Texas at El Paso
in Partial Fulfillment
of the Requirements
for the Degree of

DOCTOR OF PHILOSOPHY

Department of Geological Sciences
THE UNIVERSITY OF TEXAS AT EL PASO
May 2020

Acknowledgements

This dissertation would not have been possible without the permission of the Pueblo of Laguna Reservation to access their land. In particular, I wish to thank Marlene Analla (Executive Assistant to Tribal Secretary), Gregory Jojolla (Environmental Program Manager), and Frank Cerno Jr. (Chief Judge). Next, I would like to give a very special thanks to the unsung heroes of our department Dr. Annette Veilleux, Christine Sanchez, Kristen Gonzalez, Carlos Montana, Amber Bruner, and Cynthia Salas-Santoyo for assisting, supporting, and putting up with me.

Funding for my projects was provided by National Earthquake Hazards Reduction Program, UTEP Dodson Research Grant, American Institute of Professional Geologist-TX Shoemaker Scholarship, Jornada Basin LTER Fellowship, and Geological Society of America Grant. Additional funding for laboratory work, field work, and tuition was provided by the West Texas Geological Society Scholarship, South Texas Academic Rising Scholars Scholarship, Association of Environmental and Engineering Geologists Scholarship, James Cearley Scholarship (twice), and the Bruce Davidson Award. Travel aid for conferences was provided by the Goldschmidt Travel Grant, GSA OTF Travel Grant, Earth Educators Rendezvous Grant, the Department of Geological Sciences at UTEP, and by Dr. Aaron Velasco. Finally, I wish to thank Dr. Diane Natalicio for financial support through the Natalicio Dissertation Fellowship.

I would like to thank my advisor's Dr. Lin Ma and Dr. Jason W. Ricketts. Thank you for your patience, continuous support, giving me space when I needed it, pushing me when I stalled, and for your mentorship. I would also like to thank my former advisor Dr. Peter Reiners for aiding in molding me into the scientist I am today. I also thank my committee members Dr. Terry L. Pavlis, Dr. Craig E. Tweedie, and especially, Dr. Aaron Velasco. Thank you Dr. Velasco for mentoring me all of these years and looking after me.

I would also like to thank all of the undergraduate students I got to work with. In particular, I thank Julieta Saucedo for keeping me entertained while doing column chemistry, Paola Soto-Montero for being a model student and friend, Guadalupe Alvarez Rodriguez (La Bestie), and every student in the AY-PREP program, the Fall 2018 Structure class, and Fall 2019 Mineralogy class. I hope I had a positive influence in all of your undergraduate careers. Thank you for allowing me to be your teaching assistant, mentor, friend, and helping me realize my passion for teaching.

To all the colleagues and friends I made during my time at UTEP, I thank you for your friendship. In particular, I wish to thank Zach Fleming for always keeping me alert in the office with your antics and strange stories, Joey Castro for your odd friendship, Anggito Sugihono for your child-like outlook on life that always brightened my day, Kat Salas for your endearing friendship and advise through the years, and finally, Jose Tonty Garcia, for reminding me of my upbringing and all those late nights at Hope and Anchor. Completion of this dissertation would not have been possible without the contributions to society from Benito Antonio Martinez Ocasio, Aubrey D. Graham, Arthur Guinness, Wilhelm Haase, Alberto Aldrete, Gerard Adriaan Heineken, Braulio Iriarte Goyeneche, and especially, Edgar Everaert.

I would also like to acknowledge the following people for their support, love, and friendship throughout the years: my dad, siblings, my nephews, niece, and my childhood best friends Ernesto (Crack), Felipe (Baloy), Chairez, Jose (Fat Joe), and Omar (Fatty). To conclude, I want to thank the four most important and influential people in my life. My mom for your intelligence, your strong-willed character, and morals you instilled in me. My Nina and tia Sara (my other moms) for their unconditional love and chipliandome my entire life. And finally, my wife Ale for your dorky humor, love, your support, and most importantly, for choosing me to be your partner in life.

Abstract

Fault zones in the shallow crust impact a variety of geological processes including mineral deposition, fluid flow patterns in shallow and deep groundwater aquifers, and most importantly seismic activity. The specific interplays of fault zones, seismicity, and groundwater flows are complex and not well understood despite the importance they have to society. The Rio Grande rift is a region impacted by seismic and volcanic activity that place the first order control on mineral formation and fluid flow patterns. It is also a region that is often disregarded as a seismic hazard due to its inferred low tectonic rates and long recurrence intervals for fault movement. Many studies of the Rio Grande rift have focused on the structure and stratigraphy of individual basins but few have focused on understanding the importance of fluid flow and fault interactions.

This dissertation aims at contributing to the study of Rio Grande rift by focusing on different aspects of fault and groundwater interactions throughout the rift. Specifically, secondary carbonate minerals found at or near fault zones are used to provide new insights on past and present climatic, hydrologic, and tectonic changes, as well as geochemical evidence for both deep and shallow fluid interaction near faults. In this study, we use various isotope signatures to determine the source of fluids and environmental conditions, and Uranium-series geochronology to constrain carbonate formation. This dissertation constrains fault movement along the East Franklin Mountain fault using pedogenic carbonates, constrains fault movement, paleo fluid flow patterns, and paleo-climate transitions in Laguna, New Mexico using travertine deposits that formed along the Santa Fe fault, and evaluates modern fluid flow and sources in central New Mexico. Additionally, a preliminary study is provided which attempted to constrain fault movement and fluid flow patterns in the Jornada Basin.

Table of Contents

Dedication.....	iii
Acknowledgements.....	v
Abstract.....	vii
Table of Contents.....	viii
List of Tables.....	xii
List of Figures.....	xiii
Chapter 1: Introduction.....	1
Chapter 2: Uranium-series dating of the East Franklin Mountains fault carbonates in El Paso, Texas: Implications for paleoseismic activity of the southern Rio Grande rift.....	3
2.1 ABSTRACT.....	3
2.2 INTRODUCTION.....	4
2.3 GEOLOGIC SETTING.....	6
2.4 METHODS.....	7
2.4.1 Trench Site.....	7
2.4.2 Geochronologic Samples.....	8
2.4.2.1 Radiocarbon.....	8
2.4.2.2 Optically-Stimulated Luminescence.....	9
2.4.2.3. U-series Disequilibrium.....	10
2.5 RESULTS.....	10
2.5.1 Radiocarbon.....	10
2.5.2 OSL.....	11
2.5.3 U-series.....	11
2.6 DISCUSSION.....	12
2.6.1 Unusually young radiocarbon ages.....	12
2.6.2 Colluvial wedges age interpretations.....	13
2.6.3 MRE age constraint.....	15
2.6.4 Age constraints in the northern EFMF trench.....	16
2.7 CONCLUSIONS.....	18

2.8 ACKNOWLEDGMENTS	19
2.9 SUPPLEMENTARY INFORMATION	19
2.9.1 BACKGROUND	19
2.9.1.1 Pedogenic Carbonates	19
2.9.1.2 Radiocarbon Dating	20
2.9.1.3 Optically Stimulated Luminescence	22
2.9.1.4 Uranium-series Dating	23
2.9.2 U-SERIES METHODS	24
2.10 REFERENCES	26
2.11 TABLES	37
2.12 FIGURES	39
 Chapter 3: Travertine deposits of the Lucero Uplift, New Mexico: Geochemical record of neotectonic and mantle activity in the Santa Fe fault zone.....	43
3.1 ABSTRACT	43
3.2 INTRODUCTION.....	44
3.3 BACKGROUND.....	45
3.3.1 Travertine Formation.....	45
3.3.2 Tectonic vs. Climate Controls on the Formation of Travertine.....	47
3.3.3 Geologic Setting of Rio Grande rift.....	48
3.3.4 Geological Setting of the Lucero Uplift.....	49
3.3.5 Uranium-series (U-series) Chronometer and Geochemical Tracers.....	51
3.3.5.1 U-series Dating and ($^{234}\text{U}/^{238}\text{U}$) _i ratios.....	51
3.3.5.2 Strontium Isotope Ratios ($^{87}\text{Sr}/^{86}\text{Sr}$).....	52
3.3.5.3 Carbon and O Isotope ratios ($\delta^{18}\text{O}$ and $\delta^{13}\text{C}$).....	53
3.4 METHODS	54
3.4.1 Travertine Sample Selection	54
3.4.2 U-series Isotope Analysis	54
3.4.3 Strontium Isotopes Analysis	56
3.4.4 Carbon and Oxygen Isotopes Analysis.....	57
3.5 RESULTS	58
3.5.1 U-series Isotope Ratios and Ages	58
3.5.2 Strontium Isotopes	59

3.5.3 Carbon and Oxygen Isotopes	59
3.6 DISCUSSION.....	60
3.6.1 Travertine Age Distribution and Formation Rates	60
3.6.2 Tectonic Implications: structural observations and age constraints	63
3.6.3 Paleo-fluid Sources and evolution history inferred from the travertine geochemical record of $\delta^{13}\text{C}$ and $\delta^{18}\text{O}$	65
3.6.4 Paleo-fluid Sources inferred from the travertine geochemical record of Sr and U isotopes.....	67
3.6.5 Sr and U isotope and concentration mixing	69
3.6.6 Regional Implications.....	70
3.7 CONCLUSIONS	73
3.8 REFERENCES	74
3.9 TABLES	89
3.10 FIGURES.....	94
Chapter 4: Hydrogeochemistry of travertine-precipitating springs of the Santa Fe fault zone ...	103
4.1 ABSTRACT	103
4.2 INTRODUCTION.....	104
4.3 BACKGROUND.....	105
4.3.1 Geologic Setting.....	105
4.3.2 Study Area Geology	106
4.3.3 Uranium-series Isotopes	107
4.3.4 Strontium Isotopes	108
4.4 METHODS	108
4.4.1 Sample Selection.....	108
4.4.2 U-series Analysis	109
4.4.3 Strontium Isotopes	110
4.4.4 Major Ions	111
4.5 RESULTS	111
4.5.1 U-series Ratios	111
4.5.2 Strontium Isotopes	111
4.5.3 Major Ions	112
4.6 DISCUSSION.....	113

4.6.1 U Isotope Sources and Implications	113
4.6.2 $^{87}\text{Sr}/^{86}\text{Sr}$ Sources and Implications	114
4.6.3 $^{234}\text{U}/^{238}\text{U}$ vs $^{87}\text{Sr}/^{86}\text{Sr}$ Mixing Model	115
4.6.4 Major Ion Chemistry	117
4.6.5 Regional Implications.....	118
4.7 SUMMARY AND CONCLUSIONS	120
4.8 REFERENCES	122
4.9 TABLES	132
4.10 FIGURES.....	134
Appendix	143
Vita	150

List of Tables

Table 2.1 Radiocarbon results of samples collected from unit CV within the BMC trench.....	37
Table 2.2 OSL results of sediment samples collected from various units within the BMC trench.	37
Table 2.3 U-series, C, and O Isotope results of sediment samples collected from various units within the BMC trench.	38
Table 3.1 Sample Locations and Descriptions.....	89
Table 3.2 Travertine Geochronology.....	90
Table 3.3 Travertine Isotope Data	91
Table 3.4 Travertine Growth Rates.....	93
Table 4.1 Spring and River Data.....	132
Table 4.2 Isotope Data.....	132
Table 4.3 Major Ion Chemistry (ppm).....	133

List of Figures

Figure 2.1 A) Regional map showing alluvial basins of the Rio Grande rift in yellow and location of study area. 1993/2003 trench site by Keaton and Barnes, 1996 and McCalpin, 2006. B) Digital elevation model of the Paso del Norte region with fault traces shown in various colors (refer to Relative Fault Ages legend; USGS Earthquake Hazards Program). Red dashed/solid line = trace of East Franklin Mountain fault (EFMF); TX = Texas; NM = New Mexico; CH = Chihuahua. C) Satellite image of trench location relative to EFMF. 39

Figure 2.2 A) Image of main fault zone exposed on the south wall. Shoring rails are 20 cm wide. Large yellow arrows = main fault, smaller yellow arrows = minor faults, CV = no pedogenic carbonates present; poorly sorted gravel, CIV = stage 3 pedogenic carbonates, CIII = stage 3 pedogenic carbonates; matrix supported pebbles, CII = stage 3 pedogenic carbonates; matrix supported gravel, CI = stage 3 pedogenic carbonates; contains boulders. B) Slickenside carbonates on main fault plane. 40

Figure 2.3 Log of the south wall of the Beaumont Medical Center trench showing locations of dated samples. Refer to Pavlis et al., 2017 for detailed unit descriptions and expanded log of the south wall. Red lines = faults and ---- = no sample collected on Geochronology of Trench Units table. Sample EFU2 (U-series) was collected but not dated. EFU3 was collected from the same unit and dated. 41

Figure 2.4 A) $(^{234}\text{U}/^{238}\text{U})$ vs $(^{232}\text{Th}/^{238}\text{U})$ and $(^{230}\text{Th}/^{238}\text{U})$ vs $(^{232}\text{Th}/^{238}\text{U})$ isochrons used to show the correction of detrital ^{230}Th in pedogenic carbonates collected from the fault zone. B) U-series evolution diagram with respective dated samples after detrital ^{230}Th correction (various colored circles). Approximate ages determined using $^{234}\text{U}/^{238}\text{U}$ initial and $^{230}\text{Th}/^{238}\text{U}$ initial from isochrons estimated in Fig. 4A. U-series ages determined using Berkeley Geochronology Center's Isoplot software v.3.75. 42

Figure 3.1 A) Regional digital elevation model showing location of travertine deposits in association with the Jemez Lineament, Rio Grande rift, Quaternary volcanism, and Quaternary faults (Barker et al., 1996). Travertine locations in the southern New Mexico (within the Rio Grande rift) were removed because the authors of this study visited those locations and determined they were not travertine deposits. Refer to Barker et al., 1996 for all location descriptions. B) Location of study area within the Jemez Lineament (red shaded region) on the western margin of the Rio Grande rift. Also shown is the Socorro magma body, which has been active since ~ 30 Ma. 94

Figure 3.2 A) Geologic map of study area showing location of travertine deposits and location of collected samples. B) Image of tilted Mesozoic units and younger horizontal travertine deposits forming at high elevations (older travertine deposits) and lower elevations (younger travertine deposits). C) Image of active travertine precipitation forming drapes and curtains. Red-orange color due to Fe-oxide material co-precipitating with travertine. D) Image of small travertine pool and dam structures that are active. E) Tilted Santa Fe group overlaid by undeformed travertine deposits. F) Cross section through study area showing Precambrian, Paleozoic, Mesozoic, and Quaternary units. 95

Figure 3.3 Images of collected travertine samples. Number on image refers to: 1 = travertine sample, 2 = drilling of hand sample, 3 and 4 = thin sections of travertine samples. A) Thin micritic layers in which textures are difficult to discern and many voids are present in the sample. B) Multiple thick botryoidal travertine layers (separated by yellow dashed line) with travertine growth indicated by radiating upward geometry of elongate calcite fibers. C) Chaotic

travertine growth from multiple layers radiating in many different directions. D) Thick botryoidal travertine layers with many voids showing easy dissolution of material..... 96

Figure 3.4 A) U-series travertine ages from this study plotted against $(^{234}\text{U}/^{238}\text{U})_i$. Kernel density estimate (KDE) and histograms of data shown. U-series ages determined using Berkeley Geochronology Center’s Isoplot software v.3.75. B) Travertine precipitation rates. C) U-series travertine ages, from other travertine studies in the Rio Grande rift and along the Jemez Lineament, plotted against $(^{234}\text{U}/^{238}\text{U})_i$. Kernel density estimate (KDE) and histograms of data shown. D) U-series travertine ages, from all other travertine/calcite vein studies in North America, plotted against $(^{234}\text{U}/^{238}\text{U})_i$. Kernel density estimate (KDE) and histograms of data shown. Vertical grey rectangles refer to glacial periods while white rectangles represent interglacial periods..... 97

Figure 3.5 Strontium isotope signatures of travertine vs. U-series determined ages (ka). Red = Qtr3 group (>400 ka), Green = Qtr2 group (100 ka – 400 ka), Yellow = Qtr1 group (< 100 ka). Error bars not shown where uncertainty (2sigma) is less than symbol size; uncertainty decreases with younger ages. Vertical grey rectangles refer to glacial periods while white rectangles represent interglacial periods. 98

Figure 3.6 Summary of $\delta^{13}\text{C}$ (A) and $\delta^{18}\text{O}$ (B) vs. U-series determined ages (ka). Our data is compared to regional ^{13}C and ^{18}O record analyses of Kampman et al. (2012) and Williams et al. (2017), whom argue in favor of climatic influences for travertine formation (Kampman study) and against climatic influences (Williams study; attribute local tectonics). Vertical grey rectangles refer to glacial periods while white rectangles represent interglacial periods. 98

Figure 3.7 Stable carbon and oxygen isotope compositions of the three travertine groups of this study in the Lucero Uplift. Error bars not visible due to uncertainty (2sigma) being less than symbol size. Light red shaded area is range of worldwide travertine isotopic compositions associated with thermal/endogenic fluid sources..... 99

Figure 3.8 $^{87}\text{Sr}/^{86}\text{Sr}$ vs. $(^{234}\text{U}/^{238}\text{U})_i$ isotopic compositions mixing model of samples from the three travertine groups of this study showing little variation in Sr isotopic signature. Purple and light blue squares indicate endmember isotopic compositions of the Sandia Granite (purple; Brookins and Majundir (1988), Brookins and Majundir (1982), Crossey et al., 2006) and Rio Grande water sample (light blue; this study). Light red shaded rectangle is the region in which endogenic derived fluids would lie on this model. Light blue shaded rectangle is the region in which epigenic (i.e. meteoric) fluids would lie. Various mixing lines of the two endmembers (i.e. Sandia Granite and Rio Grande) are shown as solid black lines; curve is dependent on the relative elemental concentrations of each endmember. Direct mixing of the two chosen endmembers should result in a fluid mixing trajectory with a concentration ratio of 25 (red dashed line). Sandia Granite (Endmember #1): $^{87}\text{Sr}/^{86}\text{Sr} = 0.748$, $[\text{Sr}] = 220$ ppm, $(^{234}\text{U}/^{238}\text{U})_i = 10$, $[\text{U}] = 4.7$ ppm; Rio Grande (Endmember #2): $^{87}\text{Sr}/^{86}\text{Sr} = 0.709$, $[\text{Sr}] = 0.490$ ppm, $(^{234}\text{U}/^{238}\text{U})_i = 1.69$, $[\text{U}] = 0.002$ ppm. 100

Figure 3.9 A) Mantle tomography from Schmandt and Humphreys (2010) showing s-wave velocities at 125 km depth overlaying a DEM of our study region. Also shown are Quaternary volcanics of the Jemez Lineament, Quaternary faults of the Rio Grande rift, seismic events in the last ~80 years, $^3\text{He}/^4\text{He}$ corrected ratios (Rc/Ra; green boxes; Newell et al., 2005; Williams et al., 2013), location of travertine studies with ages, and two cross section lines from Sosa et al. (2014). B) Cross section A-A’ at latitude 34° showing clear distinctions between the Socorro Magma Body (SMB), Rio Grande rift (white boundary lines), and Jemez Lineament (red anomaly). High velocity zones appear under the Rio Grande rift and continue into Arizona (AZ)

between depths of 200-300 km. Jemez Lineament volcanics are overlaid on this Vs-model as well as our study area and location of the SMB. 101

Figure 3.10 Top left: Tilted Santa Fe Group units overlaid by undeformed travertine deposits near the west bounding fault (Santa Fe fault) of the Rio Grande rift. Top right: Schematic cross section of travertine forming over the Santa Fe fault in our study area. Mantle derived gases and fluids are migrating up faults and coming in contact with different units. Middle: Conceptual model of the tectonic setting of the Rio Grande rift and Jemez Lineament after Williams et al. (2013) and Priewisch et al. (2014). The model show gases originating in the upper mantle and diffusing through the crust as well as magmatic systems. Magmatic fluids and mantle gases ascend along deep penetrating faults, like the Santa Fe fault, to the surface leading to travertine formation. Bottom: Cross section B-B' from Sosa et al. (2014) that crosses our study area. A high velocity zone underlies the Rio Grande rift, in particular in the area of the Jemez Lineament, which is termed the Jemez Upwelling. 102

Figure 4.1 Digital elevation model showing location of travertine-precipitating springs and river samples collected in this study. Also shown are faults associated with the Rio Grande rift (red lines), the Jemez Lineament (black blobs), and the outline of the Socorro Magma Body (faded grey circle). 134

Figure 4.2 Geologic cross-section line A-A' from map on Figure 1 showing asymmetrical basins bounded by major rift bounding faults as well as smaller intrabasin faults. Hypothesized fluid flow types are shown in red arrows to represent endogenic fluids, blue arrows represent epigenic fluids in shallow basins adjacent to major rift bounding faults, and green arrows represent epigenic fluids in deeper basins of the Rio Grande rift system. Potential lithology endmembers include Precambrian (crystalline basement), Paleozoic (mainly carbonates), Mesozoic (mix of sedimentary rocks), and Quaternary (rift fill) units. 135

Figure 4.3 Digital elevation map of study area depicting faults (red solid and dashed lines) of the Santa Fe fault system. Location of collected travertine-precipitating springs are represented by red circles while two river samples collected from the Rio Puerco are represented by blue circles. Three more river samples were collected but are not observable at the scale of this map. Refer to Figure 1 for location of other river samples of this study. White circles are river and spring samples from Williams et al., (2013). 136

Figure 4.4 Left: $^{234}\text{U}/^{238}\text{U}$ vs U (ppb) plot. Spring samples (red circles) tend to have higher $^{234}\text{U}/^{238}\text{U}$ ratios and U concentrations compared to river samples (blue and light blue circles). Right: $^{234}\text{U}/^{238}\text{U}$ vs 1/U (ppb) plot. 137

Figure 4.5 $^{87}\text{Sr}/^{86}\text{Sr}$ vs Sr (ppm) plot. Spring samples (red circles) tend to have higher $^{87}\text{Sr}/^{86}\text{Sr}$ ratios and Sr concentrations compared to river samples (blue and light blue circles). 137

Figure 4.6 Piper diagram of study area showing two distinct hydrogeochemical facies. Travertine-precipitating spring samples lie within an endogenic facies with high amounts of Na and Cl relative to other ions. River samples lie within a mixed cation group representing epigenic facies. 138

Figure 4.7 Cross section B-B' from Figure 3 showing lithology that hypothetical endogenic fluid flow paths would encounter in the Santa Fe fault system. Also shown are $^{234}\text{U}/^{238}\text{U}$ and $^{87}\text{Sr}/^{86}\text{Sr}$ signature of the different end members and lithologies located in our study. Sandia Granite (Endmember #1): $^{87}\text{Sr}/^{86}\text{Sr} = 0.748$, [Sr] = 220 ppm, $(^{234}\text{U}/^{238}\text{U})_i = 10$, [U] = 4.7 ppm; Rio Grande (Endmember #2): $^{87}\text{Sr}/^{86}\text{Sr} = 0.709$, [Sr] = 0.490 ppm, $(^{234}\text{U}/^{238}\text{U})_i = 1.69$, [U] = 0.002 ppm. Endmember #1 and #2 isotopic ratios and concentrations from Brookins and Majundir

(1988), Brookins and Majumdir (1982), Crossey et al., 2006, and this study. See text for references for other isotopic signatures. 139

Figure 4.8 $^{87}\text{Sr}/^{86}\text{Sr}$ vs. $(^{234}\text{U}/^{238}\text{U})_i$ isotopic compositions mixing model between travertine-precipitating springs, river, and travertine samples. Three endmembers were considered for mixing lines. Endmember #1 = highly radiogenic crystalline basement, #2 = shallow meteoric fluids, and #3 less radiogenic crystalline basement. A) Mixing lines are shown for endmember #1 and #2. B) Various mixing lines between endmembers #2 and #3 are shown. Light red shaded rectangle is the region in which endogenic derived fluids would lie on this model. Light blue shaded rectangle is the region in which epigenic (i.e. meteoric) fluids would lie. Crystalline basement (Endmember #1): $^{87}\text{Sr}/^{86}\text{Sr} = 0.748$, $[\text{Sr}] = 220$ ppm, $(^{234}\text{U}/^{238}\text{U})_i = 10$, $[\text{U}] = 4.7$ ppm; Rio Grande (Endmember #2): $^{87}\text{Sr}/^{86}\text{Sr} = 0.709$, $[\text{Sr}] = 0.490$ ppm, $(^{234}\text{U}/^{238}\text{U})_i = 1.69$, $[\text{U}] = 0.002$ ppm; Crystalline basement (Endmember #3): $^{87}\text{Sr}/^{86}\text{Sr} = 0.730$, $[\text{Sr}] = 220$ ppm, $(^{234}\text{U}/^{238}\text{U})_i = 10$, $[\text{U}] = 4.7$ ppm. 140

Figure 4.9 Water types of various spring, river, and well samples of the San Luis, Española, Albuquerque, and Socorro basin. Water types based on which hydrogeochemical facies data points plotted in on Figure 10. Classification scheme is very similar to those used by Goff and Shevenell, 1987, Williams et al., 2013, McGibbon et al., 2018, and Blomgren et al., 2019. Also pictured are $^3\text{He}/^4\text{He}$ ratios from Newell et al., 2005 showing anomalously high He ratios associated with localized mantle degassing underneath the Rio Grande rift. Travertine-precipitating springs all have endogenic signatures; different symbols are used to stand out their locations. 141

Figure 4.10 Piper diagram of water types from multiple studies of the Rio Grande rift. Color refers to which hydrogeochemical facies samples plot in (e.g. HF1-endogenic = red colors, HF2-volcanic = black colors, etc.) Shape refers to location. Top left: Water data from the San Luis, Española, and Socorro basin. HF1 facies tend to be located along the western margin of the Rio Grande rift (see Figure 9). Top right: Water data from the Albuquerque basin. HF1 facies are generally located near the western margin of the Rio Grande rift and along intrabasin faults near the western margin. Bottom left: Water data from Valles Caldera. HF1 data is from geothermal well data and from various springs of the Valles Caldera system. Bottom right: Travertine-precipitating springs of the Rio Grande rift. The majority of the springs plot in the HF1 facies with the exception of Ojo Caliente/La Madera springs, which have a bigger influence from meteoric fluids. Data from Goff and Shevenell, 1987; Crossey et al., 2011; Williams et al., 2013; McGibbon et al., 2018; Blomgren et al., 2019. 142

Chapter 1: Introduction

Fault zones in the shallow crust play an important role in a wide range of fluid related geological processes such as seismic activity, mineral deposition, hydrocarbon migration, and most importantly, govern fluid storage, fluid flow patterns, and fluid distribution (Deming, 1992; Fossen et al., 2010; Barton et al., 1995). For example, deformation of fault zones is recognized to be a critical element in the augmentation of permeability in the Earth's crust (Claesson et al., 2007). With increased permeability, faults act as conduits for fluid migration, which can result in the mixing of deep and shallow fluids. When these fluids are saturated in certain elements and/or ions they can begin to precipitate minerals (e.g. calcite, quartz, clay) that subsequently seal off the recently opened fractures (Parry, 1998; Claesson et al., 2007). Therefore, these minerals serve as a record of past fluid flow, seismic events, and potentially climate.

Field observations of exposed fault zones suggest that the hydrology in faults can vary strongly in space and time, that is, fault zones may undergo cycles of acting as both a conduit and barrier during deformation (Ngwenya et al., 2000). The specific interactions of fault zone activity and fluid flow are complex and not well understood despite the importance it has to society (e.g. hydrocarbon exploitation, contaminant transport, CO₂ storage, groundwater resource managements, etc.). To further complicate matters, fluid transport along fault zones can vary significantly on timescales ranging from seconds to hundreds of thousands of years, which are influenced by regional or global changes in tectonics and/or climate (Sibson et al. 1975; Eichhubl and Boles, 2000; Fulton et al., 2016; Minissale et al., 2002; Faccenna et al., 2008).

The Rio Grande rift, which separates the Colorado Plateau on the west from the Great Plains on the east, is a zone where the Earth's crust is being pulled apart (rifting), thus creating many basins and fault zones that offer excellent locations to investigate how tectonics and climate

impact fluids in the shallow crust. In the Rio Grande rift, rift-related normal faults appear to have a significant influence on fluid chemistry, which reflects the different sources.

This dissertation contributes to the study of Rio Grande rift by focusing on different aspects of fault and groundwater interactions throughout the rift. Specifically, carbonate minerals found at or near fault zones are used to provide new insights on past and present climatic, hydrologic, and tectonic changes, as well as geochemical evidence for both deep and shallow groundwater mixing near faults. Here we investigate carbonate minerals using mineralogic, geochemical, isotopic and geochronologic data from four study areas (East Franklin Mountains fault, El Paso, TX; Lucero Uplift, Pueblo of Laguna, NM; central New Mexico; Appendix: Jornada Basin, Las Cruces, NM) to constrain fault activity in some cases, derive paleo-climate information, calculate rates of carbonate formation, and interpret fluid-flow patterns.

Chapter 2: Uranium-series dating of the East Franklin Mountains fault carbonates in El Paso, Texas: Implications for paleoseismic activity of the southern Rio Grande rift

Victor H. Garcia^{1*}, Richard Alfaro¹, James P. McCalpin² Jose M. Hurtado¹, Terry L. Pavlis¹, Jason Ricketts¹, Lin Ma¹

¹Department of Geological Sciences, The University of Texas at El Paso, 500 West University Ave. El Paso, TX. 79968

²GEO-HAZ Consulting, Inc. 600 E Galena Ave, Crestone, CO. 81131

** Corresponding author vhgarcia4@miners.utep.edu*

2.1 ABSTRACT

The El Paso-Juarez region, with a combined population of ~2.3 million people, is traversed by the East Franklin Mountain fault (EFMF), yet its seismic risk is poorly understood. To better understand past tectonic activity in this region, a paleoseismic trench was excavated across the EFMF at the McKelligon Canyon step-over on the only undisturbed section of the fault. The excavation exposed the main fault surface as well as five fault-related colluvial wedges. Direct dating of associated events was done using radiocarbon, optically stimulated luminescence (OSL), and Uranium-series methods to constrain the timing of the most recent event as well as to understand the relationship and timing of pedogenic carbonate formation in the trench. Radiocarbon ages on charcoal material collected from the most recent event colluvial wedge range from 0.5 ka to 1.2 ka, indicating relatively young movement of the EFMF. However, we argue that the radiocarbon ages are possibly contaminated by younger carbon material, not representative of the most recent event due to observations based on stratigraphic position and lack of young fault scarps offsetting Holocene deposits. OSL ages indicate development of multiple stages of colluvial wedges, which range from 39.9 ± 7.4 ka to 82 ± 15.4 ka. However, U-series ages of the same

colluvial wedges are systematically younger, from 21.2 ± 5.7 ka to 32.9 ± 9.4 ka, while two fault precipitated calcite samples yield U-series ages of 10.6 ± 0.6 ka and 12.1 ± 3.5 ka. We interpret OSL ages as recording the last time sediments were exposed at the surface while U-series ages record progressive buildup of pedogenic carbonates within the colluvial wedges after the sedimentation. The young fault precipitated calcite U-series ages (~ 10 - 12 ka) most likely record the latest pulse of carbonate formation in the fault zone related to the most recent faulting event. We conclude that the last earthquake of the EFMF occurred 10-12 ka.

2.2 INTRODUCTION

Current earthquake hazard assessments include a number of factors, such as identifying and determining fault history, mapping soil type, determining infrastructure vulnerability, and determining the recent and historic seismicity. Obtaining a long enough historic record of seismicity remains difficult, since the instrumented record of earthquakes is just over 100 years, with more accurate estimates of earthquake location and size only occurring within the last 50-60 years due to standard global, regional, and local seismic networks. In regions considered to be tectonically active, we consider geologically recent seismic events to have occurred within 500 years, for example, in areas near plate boundaries where slip rates range from a few mm/year to several cm/year (Machette, 1998). For seismic hazard analysis, the challenge remains to compare and analyze short term records (i.e., recent historical seismicity) to long term records (i.e. paleoseismic evidence) (Machette, 1998), due mainly to this time gap in analysis for the seismic and geologic records. In active regions with lower displacement rates, such as the Rio Grande rift (Figure 1A) where slip rates are less than 1 mm/year, recurrence intervals (typically ~ 1 ka to 150 ka) from surface ruptures become difficult to assess due to a lack of historical evidence (i.e. inhabitants experienced seismicity), though there is abundant evidence for recent Quaternary

faulting (Von Hake, 1975; Machette, 1998; McCalpin et al., 2011; Williams et al., 2017). Thus, paleoseismic studies that can determine absolute time constraints on long term fault activity can be used to assess potential seismic activity and hazards.

The East Franklin Mountains fault (EFMF; Figure 1) traverses the El Paso-Juarez metropolitan area and is an example of a major Rio Grande rift fault that poses as a significant seismic hazard (Collins et al., 1996; Machette, 1998) to the Paso del Norte region (El Paso-Ciudad Juarez; ~2.3 million inhabitants). The EFMF has historically been viewed as a low-hazard fault but based on the length of the fault and Quaternary scarps (up to 60 m high), it has the potential to generate earthquakes in the magnitude range of 6.1-7.2 (Machette, 1998; Crone, 2009; USGS ref). Unfortunately, the paleo-seismologic record of this structure remains poorly studied, and the fault is essentially unknown to the local population. Previous studies reconstructed the slip history and timing for the most recent event (MRE; 12.7 ka) at the northern end of the EFMF (Figure 1B) (Keaton and Barnes, 1996; McCalpin, 2006). However, it is unknown whether the slip history and MRE are characteristic of the entire EFMF, or if instead, the fault is comprised of multiple fault segments that have the potential to generate much smaller earthquakes compared to one single and longer fault.

To constrain the timing of the MRE on the southern segment of the EFMF, a paleoseismic trench was excavated at the McKelligon Canyon step-over (Figure 1C), the largest geometric irregularity of the EFMF system. The purpose of this study is to assess the use of the Uranium-disequilibrium series (U-series) technique to directly date the timing of the last rupture event of the EFMF. This study combines U-series dating methods on pedogenic carbonates and fault precipitated calcite material with radiocarbon (^{14}C) and optically-stimulated luminescence (OSL) dating techniques on charcoal and bulk sediments, respectively. The application of these diverse

geochronologic techniques provides an opportunity to date and compare different aspects of ages related to shallow fault zones, a multi-age dating approach that we utilize to explore in this paper to better understand the EFMF system in Rio Grande rift.

2.3 GEOLOGIC SETTING

The Rio Grande rift extends from Leadville, Colorado south to the Mexican states of Chihuahua and Sonora (~1,000 km long; Figure 1A) and is estimated to have had at least 22 large earthquakes ($M > 6.25$) associated with surface ruptures in the last 10,000 years (Machette, 1998). In recent times, the largest felt earthquake ($M 6.25$) in the rift occurred near Valentine, Texas in 1931 (Doser, 1987). The Rio Grande rift is made up of a series of half-grabens and asymmetrical horst blocks resulting in nine basins and 16 sub-basins that are linked by accommodation zones (Mack and Seager, 1990; Chapin and Cather, 1994; Machette, 1998; Hudson and Grouch, 2013; Armour, 2014). Major Quaternary faults are primarily restricted to major rift uplifts, such as the Sangre de Cristo Mountains (southern Colorado-northern New Mexico) in the north to the Franklin Mountains (west Texas; study area) in the southern portion of the Rio Grande rift (Machette and Hawley, 1996; Machette, 1998).

The Franklin Mountains are a normal fault bounded, west-tilted homocline exposing Paleozoic strata unconformably overlying Proterozoic crystalline basement (Stacey, 1991; Fetzner, 1992; Sharman, 2005; McCalpin, 2006; Armour-Finch, 2014). Uplift of the range was accomplished during development of the Rio Grande rift through movement along the east—dipping EFMF that bounds the entire eastern edge of the uplift. The EFMF separates the Proterozoic Red Bluff Granite in the footwall from Quaternary-Tertiary rift fill formations in the hanging wall (Collins and Raney, 1991). The last rupture of the EFMF occurred 12.7 ka based on radiocarbon dating of inorganic carbonate material in a tension fissure from a 2003 trench study

in the northern segment of the EFMF system (McCalpin, 2006). This study concluded that the EFMF has had 3-4 large earthquake events in the last ~64 kyrs. Earlier studies (Keaton and Barnes, 1996; Machette, 1998) have estimated that the entire EFMF zone is comprised of 2-5 fault segments with recurrence intervals of 10-20 kyrs with individual segment ruptures every 2-10 kyrs. However, Armour et al. (2018) showed that terrace offsets along the EFMF approach zero near the northern and southern boundaries of the Franklin Mountains and mimic the summit elevations of the range. This observation is potentially critical to seismic hazard assessments because it implies the present trace of the EFMF may rupture as a single fault segment, creating a larger earthquake, instead of individual fault segments as previously believed. In addition, gravity data along the southern edge of the Franklin Mountains suggest that the EFMF continues south for an additional 30 km and terminates along the eastern edge of the Sierra de Juarez range (Avila et al. 2015).

2.4 METHODS

2.4.1 Trench Site

The trench site was located in the least disturbed surface rupture near Beaumont Medical Center (31.821687°N, 106.454405°W) in El Paso, TX within the McKelligon Canyon stepover on a piedmont scarp about 1 km east of the Franklin Mountains (Fig. 1C). This area lies on an alluvial fan deposited by McKelligon Creek and correlates morphologically to the Jornada II (75-150 ka) geomorphic surfaces (Monger et al., 2009). This was a key site for direct comparison to the previous paleoseismic studies located 20 km further north (i.e. Keaton and Barnes, 1996; McCalpin, 2006) as well as locations in New Mexico along the Rio Grande rift (Fig. 1).

The footwall trench was a 21 m-long single slot 1.5 m deep, transitioning in the middle of the scarp face to a benched design 4.5 m wide that extended another 18 m east into the hanging wall. Obvious geologic contacts were marked with colored surveyors tape nailed to the walls.

Mapped units were defined either as stratigraphic units or as soil horizons developed in stratigraphic units of the fault zone (Fig. 2). Upon data collection, the trench was backfilled due to permit restrictions. Refer to Alfaro et al. (2019) for a detailed description of the trench and stratigraphic units.

2.4.2 Geochronologic Samples

2.4.2.1 Radiocarbon

Radiocarbon dating samples were collected from a colluvium unit (CV; Figs. 2, 3), deposited immediately after the MRE within the fault zone. Unit CV consists of poorly sorted gravel, host the modern surface soil, and was not engulfed by pedogenic carbonates. This was the only unit that contained charred botanics and visible charcoal that was suitable for radiocarbon dating. Bulk sample EFC-1 was collected 0.4 m below modern ground surface (bmgs) from moderately organic gravelly sand and yielded 41 small charcoal fragments weighing 0.0011 grams for C-14 dating. Bulk sample EFC-2 was collected 0.65 m bmgs from moderately organic gravelly sand and yielded 26 charred monocot/herbaceous dicot stem fragments weighing 0.0017 grams. Bulk sample EFC-3 was collected 1.3 m bmgs from slightly organic sand lens in a fissure fill and yielded a single charcoal fragment too insufficient in mass (< 0.0001 grams) for radiocarbon age determination. Sample preparation and C-14 analysis were performed by the PaleoResearch Institute in Golden, CO (refer to Appendix 2 in Pavlis et al., 2017 for detailed methodology). Radiocarbon age calibration was performed with OxCal4.2.4 (Bronk and Ramsey, 2009; Bronk et al., 2013), which is a probability-based method for converting ages in radiocarbon years into calibrated calendar years (CAL yr BP).

2.4.2.2 Optically-Stimulated Luminescence

In total, eight samples were collected for OSL dating methods, 5 from the colluvial wedge sequence (units CI-CIV; Fig. 3) and 3 from pre-faulting alluvial fan gravels (units H14, H16, and 14; Fig. 3) following sampling procedures of Nelson et al. (2015). Sample EFL1 was collected 3.3 m bmgs from within the alluvial fan package (Unit H14) of well-sorted granule to very small pebble gravel. Samples EFL2 (collected 1.9 m bmgs) and EFL3 (collected 1.6 m bmgs) from colluvial wedge unit CI were identified as possibly being the earliest wedge to have formed and is made up of boulders. Sample EFL4 was collected 1.2 m bmgs from colluvial wedge unit CII, consisting of a much harder matrix supported gravel with clasts broken in half. Sample EFL5 was collected 0.7 m bmgs from colluvial wedge unit CIII consisting of matrix supported small to large pebbles engulfed in stage 3 pedogenic carbonates. Sample EFL6 was collected 0.35 m bmgs from colluvial wedge CIV consisting small to large pebbles, similar to unit CV but engulfed by stage 3 pedogenic carbonates. Samples EFL7 (1.9 m bmgs) and EFL8 (0.55 m bmgs) were collected from within the alluvial fan package (H13a and 14, respectively). Unit H13a consists of well-sorted medium to large pebble gravel while unit 14 is composed of well sorted granule gravel containing a thin sand bed.

All samples collected for OSL dating came from units completely impregnated with secondary pedogenic carbonates (stages III-IV of Gile et al., 1981). Pedogenic carbonate impregnation is so complete that it has nearly obscured depositional contacts between the different units. OSL samples were dated by the Utah State University Luminescence Laboratory in North Logan, UT using the latest single-aliquot regenerative dose procedures (refer to Appendix 3 in Pavlis et al., 2017 for detailed methodology) for OSL dating of quartz sand. Dose-rate calculations

were determined by chemical analyses of U, Th, K, and Rb content using ICP-MS and ICP-AES techniques and conversion factors from Guerin et al. (2011).

2.4.2.3. U-series Disequilibrium

Seven soil/sediment samples (EFU-1 through EFU-7) were collected in a 1.6 m high vertical transect located approximately 6 m east of the main fault. The samples extend from unit CV (modern ground surface), down through units CIV (two samples collected 0.2 and 0.4 m bmgs, respectively), CIII (0.7 m bmgs), CII (two samples collected 0.9 and 1.3 m bmgs, respectively), and H15 (collected 1.6 m bmgs; Fig. 3). All units, with the exception of unit CV, are completely impregnated by pedogenic carbonate material. Sample EFU-7 was collected from unit H15 but could possibly be part of the very eastern tip of colluvial wedge unit CI.

Samples EFU-9 and EFU-10 were collected on either side of the main fault plane exposed on the lower north trench wall near its top (Fig. 3). Sample EFU-10 came from the carbonate impregnated gouge zone of the fault while sample EFU-9 came from a fissure fill between the main fault plane and a forward-toppled block of alluvial fan strata. This poorly sorted fissure fill was completely engulfed with Stage IV pedogenic carbonates. The pedogenic carbonates in these samples were analyzed at the Center for Earth and Environmental Isotope Research at the University of Texas at El Paso (UTEP). Refer to 'Supplementary Information' for detailed U-series analytical methods.

2.5 RESULTS

2.5.1 Radiocarbon

Bulk sample EFC-1 (0.4 m bmgs from unit CV) yielded an age of $1,213 \pm 27$ radiocarbon years before present (RCYBP) and an age range of 1260-1060 calendar years before present (CAL yr. BP) at the 2σ level (Table 1; Fig. 3). EFC-1 consisted of uncharred floral remains including a

single *Amaranthus* (amaranth) and two *Chenopodium* (goosefoot) seeds, and rootlets reflecting modern plants growing in the area. Uncharred insect chitin fragments, rodent fecal pellets, and snail shells indicate limited subsurface disturbance. Bulk sample EFC-2 was collected 0.65 m bmg from unit CV and yielded an age 512 ± 24 years (RCYBP) with a 2σ calibrated age range of 560-500 CAL yr. BP (Table 1; Fig. 3). EFC-2 consisted of charred monocot/herbaceous dicot stem fragments, indicative of grasses, sedges, and/or non-woody member of the Dicotyledonae class of Angiosperms. Bulk sample EFC-3, collected 1.3 mbgs from unit CV, yielded an insufficient mass for AMS radiocarbon dating.

2.5.2 OSL

Samples EFL-2 through EFL-6, collected 0.20 to 1.60 m bmg within the colluvial wedge sequence in the hanging wall, yielded OSL ages increasing systematically from top to bottom in stratigraphic order (Unit CIV = 39.89 ± 7.36 ka to Unit CI = 82.04 ± 15.35 ka; Table 2; Figure 3). In the pre-faulted alluvial fan section (~1 m thick colluvial wedge sequence on hanging wall; Unit H14), sample EFL-1 yielded an age of 107.96 ± 19.02 ka. On the pre-faulted alluvial fan section of the footwall, samples EFL-7 (Unit H13a) and EFL-8 (Unit 14) yielded ages of 62.86 ± 8.59 ka and 78.05 ± 11.00 ka, respectively (Table 2; not shown on Fig. 3).

2.5.3 U-series

U-series ages in pedogenic carbonates of the collected samples were derived using ($^{230}\text{Th}/^{232}\text{Th}$), ($^{238}\text{U}/^{232}\text{Th}$), and ($^{234}\text{U}/^{238}\text{U}$) ratios in co-genetic samples (i.e. bulk, leachate, residue) to construct isochrons and to infer ($^{234}\text{U}/^{238}\text{U}$) and ($^{230}\text{Th}/^{238}\text{U}$) ratios of the pure authigenic carbonate for age calculations (Osmond et al., 1970; Rosholt, 1976; Ludwig, 2003). The isochron diagrams for the five pedogenic carbonates (EFU3-7) show strong linearity ranging from $R = 0.898$ to $R = 0.999$ (Table 3; Fig. 4). Fault precipitated calcites (EFU 9-10) show strong

linearity as well (Table 3; Figure 4). Ages, and associated errors, were then calculated using Isoplot 3, which determines ages from radioactive decay equations using the measured and detrital corrected ($^{234}\text{U}/^{238}\text{U}$) and ($^{230}\text{Th}/^{238}\text{U}$) activity ratios (Ludwig, 2003).

Samples EFU-1 through EFU-7, which were collected within the colluvial wedge sequence ~6 m east of the main fault plane, yielded five ages in stratigraphic order ranging from Unit CIV = 21.2 ± 5.7 ka to Unit H15 = 36.3 ± 4.1 ka (Table 3; Fig. 3). An age could not be determined in sample EFU-1 or EFU-2 due to very little carbonate material available and high Th contamination from soil material.

Samples EFU-9 (hanging wall) and EFU-10 (foot wall), which were collected at the stratigraphic equivalent level of unit CI, yielded systematically younger ages (Table 3; Figure 3). Sample EFU-9, located in a fissure fill, yielded an age of 12.1 ± 3.6 ka, much younger than all the colluvial units with the exception of unit CV (radiocarbon age). Sample EFU-10, from the carbonate impregnated gouge zone of the fault, yielded a similarly younger age of 10.6 ± 0.6 ka.

2.6 DISCUSSION

2.6.1 Unusually young radiocarbon ages

The importance of the two radiocarbon dates in this study pertain to the most recent event (MRE), identified as unit CV (graben fill), which contains no pedogenic carbonates. No datable carbon was found in any of the other colluvial wedge units. The oldest radiocarbon date came from an unidentifiable charcoal (Sample EFC-1) reflecting deposition during the calibrated range of 1260-1250 CAL yr. BP. The youngest radiocarbon date came from charred stem fragments of sample EFC-2, representing deposition that occurred within the calibrated age range of 560-500 CAL yr. BP. These ages could potentially imply that the MRE on the EFMF, at the McKelligon Canyon stepover, occurred 0.5 to 1.25 ka. However, the stratigraphic position of samples EFC-1

(0.4 m bmg) and EFC-2 (0.65 m bmg) raise stratigraphic issues because the deeper sample has a younger age (EFC-2; ~0.5 ka) in comparison to the shallower sample (EFC-1; ~1.2 ka). This discrepancy indicates contamination by younger soil carbon, reworking of soil by fauna, or infiltration of roots at this level.

Furthermore, these ages are unlikely to represent the MRE due to the lack of young fault scarps offsetting Holocene deposits along the EFMF. All maps of Quaternary deposits along the EFMF (Raney and Collins, 1994a, 1994b; Scherschel, 1995; Keaton and Barnes, 1996) show that Holocene alluvial deposits cross the fault zone but contain no scarps, indicating that the latest rupturing event is pre-Holocene ($> \sim 10$ ka). The lack of steep fault scarps on multi-event scarps on the EFMF also serves as evidence for a relatively old MRE. If the MRE was truly 0.5-1.25 ka then we would expect to observe prominent steep fault scarps, yet none are found along the EFMF. The fault scarp in our study area is a broad smooth scarp face with no evidence of a young reactivation, which is inconsistent for a seismic event that would have occurred ~ 1 ka.

2.6.2 Colluvial wedges age interpretations

The down-dropped block of a normal fault is generally the site of sediment accumulation, burying previously developed soils after faulting events (Machette, 1978). Hence, we interpret OSL samples as possibly constraining the timing of the MRE because luminescence dating determines the last time materials were exposed to light. Indeed, ages in the critical colluvial wedge transect (samples EFL-2 to EFL-6) are in correct stratigraphic order (~ 40 to 82 ka), indicating the presence of 4-5 colluvial wedges (refer to Pavlis et al., 2017 for explanation of wedges).

Sample EFL-1, collected approximately 1 m below the colluvial wedge transect from within the pre-faulted alluvial fan (unit H14), yielded the oldest date at 108 ± 19 ka. The second oldest OSL age of 78 ± 11 ka was from the same unit 14 but located in the foot wall. Despite the

relatively large age uncertainties, the ~30 kyr difference between the two samples, which were thought to have been collected from the same stratigraphic unit, is problematic. The simplest explanation is that the unit in the footwall was incorrectly identified as unit 14 when in fact it was more likely the overlying and younger unit 15. Both of these ages are consistent with the age range of the estimated Jornada II geomorphic surface (75-150 ka; Monger et al., 20019).

Based on mapping by Pavlis et al. (2017), we expected the oldest alluvial unit to be unit H13a located at the extreme east end of the trench. However, sample EFL-7 yielded an age of 63 ± 8 ka, which is younger than the OSL ages from the oldest colluvial wedge (unit CI; 70-82 ka). Pavlis et al. (2017) suspected during logging that the lens of sandy gravel sampled might have been an inter-event local alluvium deposited at the toe of a ~1.4 m high fault scarp, which separated tabular fan strata on the west with lenticular strata on the east. A more detailed discussion on the stratigraphic order can be found in Alfaro et al. (2019).

Since pedogenic carbonates progressively accumulate in soils through multiple events of dissolution and reprecipitation overtime (Monger et al., 1998) we must consider that U-series ages should be interpreted as representing averages for several periods of carbonate growth. Additionally, the observation of the typical stage III and stage IV pedogenic carbonates in the trench likely indicate formation timescales ranging from centuries to millennia on a stable landscape (Zammanian et al., 2016).

U-series ages, acquired from pedogenic carbonates collected from within the same colluvial wedge transect (samples EFU-3 to EFU-6), were also in correct stratigraphic order (~21 to 33 ka). However, the U-series ages are approximately half as old as the OSL ages (~40-80 ka) acquired from the same colluvial units. The systematic difference in the two groups of ages reflects the nature of the event that each analytical technique is dating. OSL dates the last time sediments

were exposed to light before any soil formation or diagenetic processes affected the colluvial wedges. In other words, OSL generally should closely align with the age of paleo-seismic events if hanging-wall burial is rapid. In contrast, U-series ages of the colluvial wedges represent soil waters, saturated in Ca^{2+} and HCO_3^- ions, migrating down the soil profile to form pedogenic carbonates at depth through evapotranspiration (Monger et al., 2015). This observation suggests that burial rates are high enough that deeper pedogenic carbonates get buried quickly. Thus, the pedogenic carbonate U-series ages of the colluvial wedges potentially represent minimum ages for wedge formation, and thus faulting. This is indeed the case in our study since we found no evidence of fractures or fissures, which would allow fluids to migrate within these colluvial wedges.

2.6.3 MRE age constraint

The youngest U-series ages surprisingly come from samples EFU-9 (12.1 ± 3.6 ka) and EFU-10 (10 ± 0.6 ka). We expected these ages to be much older based on the stage IV pedogenic carbonates present and locations corresponding to the stratigraphically older unit CI (~70-80 ka). Moreover, these two fault zone dates are younger than colluvial wedge units CI-CIV, which range from 39.9 ± 7.4 to 82 ± 15.4 ka (OSL ages), and also younger than the pedogenic carbonate formation ages in colluvial wedge units of 21.2 ± 5.7 to 32.9 ± 9.4 ka (U-series ages). Disregarding these fault zone carbonate ages would result in the MRE event being constrained by either colluvial wedge unit CV or CIV.

Unit CV, which is stratigraphically related to the MRE, contains structures that provide the best evidence for interpretation of the fault damage zone. For example, unit CV is the noticeable darker-colored material in Figure 2 and has a prominent V-shaped base centered in the hanging wall of the main fault slip surface. The fill material was comprised of organic rich soil material and loose cobbles, but unfortunately contained no carbonate material to date. Consequently, age

constraints for unit CV rely on two charcoal samples with suspicious radiocarbon ages ranging from 0.5 to 1.25 ka; too young to represent the MRE as discussed above. The other constraint is provided by unit CIV, which has an OSL date of ~40 ka (seismic event prior to development of unit CIV) and a U-series age of ~20 ka (minimum age of unit CIV). This information constrains the MRE event from 0.5 ka to 20 ka. Although useful, this variation in dates is too large for most paleoseismic analyses.

Finally, the two U-series ages were collected from within the fault zone where a distinct sub-vertical fissure, within the V-shaped fill that splays into smaller subordinate fractures, is located (Figs. 2, 3). We conclude that these structural relationships within the fault damage zone are direct products of surface rupturing during the last seismic event, which created a network of open voids (i.e. fissures) for downward infiltration and precipitation of carbonate material. This leads us to interpret the ~10 to 12 ka U-series ages as recording the minimum age of the MRE. Hence, the MRE is constrained to be most likely between 10-12 ka and 20 ka by comparing ages determined from multiple methods in this study.

2.6.4 Age constraints in the northern EFMF trench

In 1993, Keaton and Barnes (1996) dug a trench across an 8 m high fault scarp north of the present study area and concluded that the MRE on the EFMF must be older than 8 ka because younger Organ units (<8 ka) were clearly unfaulted. Based on soil carbonate development in their area, scarp morphology, and alluvium deposits, they estimated that the MRE occurred between 9 and 22 ka. Additionally, they obtained a radiocarbon age of $10,880 \pm 70$ RCYBP (equivalent to 12.7 CAL yr. BP) from carbonates that formed in the youngest colluvium wedge, in a tension fissure of the main fault.

In 2003, McCalpin (2006) re-excavated the Keaton and Barnes (1996) trench to conduct a more detailed study to constrain faulting on the EFMF using radiocarbon and OSL techniques. McCalpin (2006) was unable to find datable material in the most recent colluvium unit. Instead, they dated a bulk carbonate sample from a block of soil that was down thrown into the main graben during what they identified to be the MRE. The sample yielded a radiocarbon age of $9,720 \pm 70$ RCYBP (11,120-12,200 CAL yr. BP) and an OSL age of 17.7 ± 2.3 ka. The OSL age was much younger than the underlying unit, which had an OSL age of 41.3 ± 4.2 ka with no apparent unconformities between the two units. McCalpin (2006) attributed this difference in OSL ages to partial re-zeroing of the block during deposition into the graben ~ 10 ka. Using these constraints, McCalpin (2006) inferred an age of 13-17 ka for the MRE.

In our study, the pair of U-series ages from the fault zone provide constraints on the MRE of the EFMF. Coincidentally, these two U-series ages (12.1 ± 3.6 and 10.6 ± 0.6 ka) are very similar, and within analytical error, to the radiocarbon age (~ 12.7 ka) from Keaton and Barnes (1996), as well as the radiocarbon age (~ 9.7 ka) from McCalpin (2006) on the 1993/2003 trench in the northern section of the EFMF. Such a similarity between two different dating techniques on two different samples, from different sections (20 km apart) of the 58 km long EFMF system, is likely not a coincidence. Constraining the MRE of the EFMF from ~ 10 to 13 ka would explain why there are no fault scarps in Holocene deposits (< 8 ka) along the EFMF and also the lack of a steep Holocene bevel on both trenches (i.e. the 2016 BMC trench and the 1993/2003 trench in the north). The similar ages between both trenches for the MRE and the similarity in OSL ages for previous events (i.e. colluvial wedge units) indicate that the EFMF likely ruptures as a single segment instead of 4-5 smaller individual segments. Pavlis et al. (2017) estimated average displacements per event for both the 1993/2003 and 2016 trenches (1.6 m and 2.6 m, respectively),

which indicate a 35-40 km long rupture. Approximating a fault width of 10 km, a fault length of 40 km, a crustal shear modulus of 3.0×10^{11} dyne/cm², and a slip of 2.5 m, we can calculate the moment ($M_o = \mu AD$, where μ is the shear modulus, A is the area of the fault, D is the slip) and the moment magnitude ($M_w = 2/3M_o - 10.7$), which results in a M_w 7.0 earthquake for this event.

2.7 CONCLUSIONS

Our excavation of the EFMF at the McKelligon Canyon stepover resulted in similar interpretations for the age of the MRE as the 1993/2003 trench studies (Keaton and Barnes, 1996; McCalpin, 2006). Beginning around 82 ka, the development of multiple colluvial wedges occurred along the EFMF and range from 82 ± 15.4 ka in unit CI (deeper; older) to 39.9 ± 7.4 ka to CIV (shallow; younger), similar to the 1993/2003 trench. U-series ages of those same colluvial wedges are much younger than the OSL ages and range from 32.9 ± 9.4 ka in CII (deeper; older) to 21.2 ± 5.7 ka in units CIV (shallow; younger). We interpret the OSL ages as approximate ages for the strata formation prior to faulting while U-series ages record the formation of pedogenic carbonates in the wedges (post-faulting).

The youngest ages are a pair of radiocarbon ages on charcoal material collected from the youngest colluvial wedge unit CI, which lacks development of pedogenic carbonates compared to the other colluvial wedges. The radiocarbon ages range from ~0.5 to 1.2 ka, indicating the potential youngest age and MRE on the EFMF. However, we argue that the radiocarbon ages are not representative of the MRE.

The best age controls for the MRE in our study area are the pair of U-series ages of 12.1 ± 3.6 ka and 10.6 ± 0.6 ka from carbonates collected from within the fault zone. These ages likely record the latest pulse of carbonate migration down the fault zone, which was created during the MRE. Coincidentally, these ages overlap with the age range of the MRE at the 1993/2003 trench

located 20 km north of our trench. Taken together with the OSL ages from both trenches, which are quite similar, and the MRE ages, we conclude that the EFMF is composed of a single 35-40 km long segment, which last ruptured ~10-12 ka. The results presented here confirm that the slip history and age for the MRE at the northern 1993/2003 trenches is indeed characteristic for the entire EFM system. This study also illustrates the need for more trenching studies in the southern portions of the EFMF system to have a better understanding of this seismic hazard in the vastly populated Paso del Norte region.

2.8 ACKNOWLEDGMENTS

We wish to thank Ft. Bliss for permission to dig a trench on their property, as well as John Kipp and Yvette Waychus of the Ft. Bliss Environmental Division for assisting with permits. We also wish to thank all the students, in particular Ian Capella, and UTEP faculty who helped at the trench site. We could not have completed all our work under the short time restrictions, which were imposed by the DOD. We also thank Galen Kaep for assistance with heavy equipment operation. Galen Kaep, along with Dr. Marianne Karplus, also helped in organizing the geophysical surveys at the trench site. We would also like to thank Dr. Peter Kovacik (PaleoResearch Institute Inc.) and Dr. Tammy Rittenour (USU Luminescence Lab) for geochronologic analyses of samples, which aided in our interpretation of the trench site.

2.9 SUPPLEMENTARY INFORMATION

2.9.1 BACKGROUND

2.9.1.1 Pedogenic Carbonates

Pedogenic carbonates form in a range of climatic zones but their dominant presence in soils generally signifies low annual rainfall and high evapotranspiration environments, characteristic of arid to semi-arid climates around the world (Birkeland, 1999; Eswaran et al. 2000; Srivastava et

al., 2002; Monger et al., 2006; Tanner, 2010; Violette et al., 2010). Formation of pedogenic carbonates in soils is dependent on the availability of Ca^{2+} and HCO_3^- ions in soil waters, where they are leached down the soil profile to form CaCO_3 at depth through evapotranspiration (Lal and Kimble, 2000; Monger et al., 2015). Factors affecting concentrations of these ions in soil waters include local topography, rainfall, soil texture, and mineralogy (Eswaran et al., 2000; Hirmas et al., 2010; Laudicina et al., 2013).

Pedogenic carbonates typically form parallel to the land surface and can form 1-2 m below the surface in semi-arid areas. Pedogenic carbonates occur as various types such as root casts, bands, beds, joint fillings, cylindroids, pendants on bottom of clasts, and form progressively into various morphogenetic stages (I-VI) that correlate with soil age (Gile et al., 1966; Brock and Buck, 2005; Monger et al., 2015). They include stage I pebble coatings and filaments, stage II nodule and inter-pebble fillings, stage III calcic horizons with carbonate plugged zones, stage IV laminar layers overlying plugged horizons, stage V calcretes with cemented pisoliths and laminae, and stage VI calcretes with multiple generations of recemented breccia, pisoliths, and laminae (Monger et al., 1991; Monger et al., 2015).

2.9.1.2 Radiocarbon Dating

Radiocarbon dating is a method that is generally used to determine the age of organic material but can also be applied to inorganic materials such as pedogenic carbonates. Materials up to ~60,000 years can be dated with precision typically in the order of +/- 100 years for the last ~1,000 years rising to the order of +/- 1,000 years at its limit (Ramsey, 2014). This technique is based on measuring the ratio of two carbon isotopes (i.e. stable carbon-12 and radioactive carbon-14). Radiocarbon is a cosmogenic isotope that is produced in the upper atmosphere primarily from the interaction of cosmic rays with nitrogen-14 (Libby, 1946). Once created, radiocarbon is rapidly

oxidized to CO₂ in the atmosphere, where it quickly diffuses throughout the atmosphere and oceans (Alves et al., 2018). Radiocarbon is then metabolically assimilated by primary producers via photosynthesis, ultimately reaching higher trophic levels via the food chain (Aitken, 1990). Consequently, the entire biosphere shares the same radiocarbon content as the atmosphere of that time period with the exception of marine plants or animals whose radiocarbon content reflects that of the oceans. Equilibrium, within the biosphere and hydrosphere, is maintained through continuous assimilation of radiocarbon from the atmosphere and the counteracting process of radioactive decay (Alves et al., 2018).

Upon death of an organism (i.e. plant or animal), carbon exchange with the atmosphere and/or ocean ceases resulting in the loss of radiocarbon through radioactive decay in a now closed system. Therefore, measuring the ratio of radiocarbon to stable carbon-12 determines how long it has been since a given sample stopped exchanging carbon with the atmosphere or ocean (Tspenyuk, 1997). Samples that relate directly to seismic events (e.g. short-lived plant material found within fault zones) can be dated using the radiocarbon technique. However, association between the dated material and seismic event must be clear (e.g. material pre- or post-dates seismic event).

Complications arise in radiocarbon dating because of variability over time in the initial ratio of radiocarbon to carbon-12 due to changes in solar and geomagnetic fields that modulate the cosmic-ray flux (Reiners et al., 2018). Because of this, radiocarbon dating is not considered an absolute dating technique and must be calibrated by measuring the ¹⁴C/¹²C ratio in samples whose age is known by other dating methods, and back calculating the initial ratio (Stuiver and Polach, 1977; Reiner et al., 2013; Ramsy, 2014).

2.9.1.3 Optically Stimulated Luminescence

Luminescence is a dating technique used to date the last time surficial sediments, which contain common naturally occurring minerals, were exposed to light and/or heat (Huntley et al., 1985; Aitken, 1998; Rhodes, 2011). Luminescence dating relies on the principle that minerals (e.g. quartz and feldspar) can store ionizing energy produced both by cosmic rays and the radioactive decay of K, Rb, U, Th, including their daughter products, within mineral grains and in their surroundings (Nelson et al., 2015; Smedley, 2018). When minerals are stimulated by light, heat or pressure, the crystal structure does not hold on to ionizing energy (i.e. electrons) and is considered to be free of any previous luminescence signal. Upon burial, radiation excites electrons causing some to become trapped, in defects or impurities, within the crystal lattices of a mineral (Rhodes, 2011). The subsequent gradual increase in trapped charges provides the basis for luminescence dating, assuming that the accumulation of energy (i.e. dose rate) resulting from environmental radiation flux has been constant (Smedley, 2018). Scarp derived colluvial wedge deposits can be dated using this method if depositional processes are slow enough to permit re-zeroing of minerals in the deposit.

Mineral grains can then be exposed to an external stimulus (i.e. light or heat) and the trapped electrons will be released (Aitken, 1998). The released electrons emit a photon of light, hence the name OSL, upon recombination at a similar site. In order to determine an age, the natural dose rate emitted from the mineral and the equivalent dose (i.e. radiation dose delivered in the laboratory) must be known (Murray and Wintle, 2000; Nelson et al., 2015). Dividing the equivalent dose by the dose rate yields the time that has passed since the mineral grain was last exposed to light or heat.

2.9.1.4 Uranium-series Dating

The U-series dating technique relies on the relationship between the radioactive decay of the parent isotope ^{238}U (half-life $t_{1/2} = \sim 4.5$ Ga), and ingrowth of the relatively short-lived daughter isotope ^{234}U ($t_{1/2} = \sim 245$ ka) that subsequently decays to ^{230}Th ($t_{1/2} = 76$ ka) (Cheng et al., 2000; Dickin, 1995). What makes this decay chain important and useful is that the radioactive parent isotope (^{238}U) has a much longer half-life than all the other intermediate nuclides. This allows secular equilibrium (i.e. daughter decay rate is equal to daughter isotope being produced from decay of parent isotope) to be attained for a period longer than 1.25 Ma. In other words, secular equilibrium conditions are met when daughter/parent activity ratio, herein indicated by parenthesis, is equal to one (i.e. unity). The activity ratios towards secular equilibrium allows for the calculation of ages and initial U activity ratios ($(^{234}\text{U}/^{238}\text{U})_0$), which are inherited from fluids from which minerals originally precipitated from (Chabaux et al., 2003).

Disequilibrium within the U-series system occurs when nuclides in the decay chain fractionate due to chemical (solubility, redox conditions, partitioning, crystallization, etc.) and physical (alpha recoil) processes (Vigier et al., 2001; Bourdon et al., 2003; Chabaux et al., 2003; Chabaux et al., 2008; Dosseto et al., 2008; Nyachoti et al. 2016). Due to high solubility of U in oxidizing environment and preferential leaching of ^{234}U into weathering fluids, which are easily released into solutions due to production by alpha recoil mechanisms, groundwater usually has both high U concentrations and high ($^{234}\text{U}/^{238}\text{U}$) ratios. In comparison, Th's low solubility, in similar environments to U, results in groundwater's with very low Th concentrations and low ($^{230}\text{Th}/^{238}\text{U}$) ratios (Langmuir and Herman, 1980). However, in the case of pedogenic carbonates, U and Th from detrital silicate sources are often included and produce ^{230}Th , which must be

corrected for U-series dating (Bischoff and Fitzpatrick, 1991; Edwards et al., 2003; Neymark, 2011).

The isochron technique is commonly employed for correction of detrital ^{230}Th in pedogenic carbonates (Ku et al., 1979; Edwards et al., 2003; Sharp et al., 2003; Paces et al., 2012). This method requires the use of co-genetic samples (e.g. total sample dissolution, leachate, and residue) in bulk pedogenic carbonates (Bischoff and Fitzpatrick, 1991; Edwards et al., 2003; Neymark, 2011). It is important to note that this correction technique takes the following assumptions into consideration: 1) pure carbonates precipitating from soil water contain no detrital Th (low solubility), 2) there are only two isotopically homogeneous end members: detrital materials and authigenic carbonates, and 3) U and Th do not enter the closed system after formation of pedogenic carbonates (Bischoff and Fitzpatrick, 1991; Luo and Ku, 1991). In general, ($^{230}\text{Th}/^{232}\text{Th}$), ($^{238}\text{U}/^{232}\text{Th}$), and ($^{234}\text{U}/^{238}\text{U}$) ratios in co-genetic samples are used to construct isochrons and to infer ($^{234}\text{U}/^{238}\text{U}$) and ($^{230}\text{Th}/^{238}\text{U}$) ratios of the pure authigenic carbonate for age calculations (Osmond et al., 1970; Rosholt, 1976; Ludwig, 2003). The application of U-series methods provides an opportunity to date shallow fault zones where calcite is precipitated in the fault zone and adjacent soils; an opportunity we explore in this paper.

2.9.2 U-SERIES METHODS

Bulk soil/sediment samples were crushed using a porcelain mortar and pestle, taking care to avoid crushing noncarbonate material. Nonetheless, to correct for detrital ^{230}Th incorporated by detrital material in pedogenic carbonates we used a set of co-genetic samples by the acid-residue approach (Ku et al., 1979). Total sample and leachate-residue digestion procedures were applied to bulk pedogenic carbonate samples. Samples were processed in batches of 12, which includes one Basalt Columbia River (BCR-2) standard reference material. For each sample, two 100-200

mg aliquots were weighed into 15 mL centrifuge tubes, then dissolved using 6 mL of 1N acetic acid (pure) and 15 mg of sodium citrate. If the majority of the sample had not fully dissolved, then 3 mL of additional 1N acetic acid were added. Samples were then allowed to settle for 10 minutes. While samples settled, $^{233}\text{U}/^{229}\text{Th}$ spike was added into 30 mL Teflon® beakers to determine U and Th concentrations using the isotope dilution method. Samples were then transferred into the spiked 30 mL Teflon® beakers. Bulk samples were completely emptied into the beakers while leachate-residue samples were put into separate beakers (i.e. solutions were poured into beakers and labeled as leachate while remaining material were poured into beakers labeled residue using de-ionized water to rinse all particles into the beaker. Samples were then placed on a hot plate at 100 °C.

Acid digestion was carried out by adding 1 mL of concentrated HNO_3 and 3 mL of HF to further dissolve materials. Samples were placed on the hot plate for one day to digest and then beaker caps were removed to dry the samples. Once dry, 1 mL of H_3BO_3 , 2 mL of 6N HCl, and 3 mL of Millipore ultrapure water (18.2M Ω) were added to each beaker (to dissolve possible fluoride precipitants created during previous digestion step) and allowed to digest for 4-8 hours or until beakers were no longer had solid material. Once completely clear of particles, samples were dried at 90 °C, dissolved in 1 mL of 7.5N HNO_3 , place into 1.5 mL vials that were centrifuged for 5 minutes at 4500 rpm.

Samples were separated and purified for U and Th using ion chromatography procedures similar to Chabaux et al., (1995). Samples, which were previously dissolved in 1 mL of 7.5N HNO_3 , were loaded into columns containing AG 1-X8 anion exchange resin (200-400 mesh). Different concentrations of HNO_3 , HCL, and HCL + Acetone Optima were used as eluents to separate, collect, and purify U and Th in the samples. Isotopic ratios ($^{234}\text{U}/^{238}\text{U}$, $^{233}\text{U}/^{238}\text{U}$,

$^{235}\text{U}/^{238}\text{U}$, $^{230}\text{Th}/^{232}\text{Th}$, and $^{229}\text{Th}/^{232}\text{Th}$) were measured using a multi-collector inductively coupled plasma mass spectrometer (MC-ICP-MS) at UTEP. A NBL U145B solution and a 229-230-232Th in-house solution were used as the bracketing standards to correct for mass fractionation and ion counter gains for U and Th isotope measurements. U and Th concentrations were calculated using measured $^{233}\text{U}/^{238}\text{U}$ and $^{229}\text{Th}/^{232}\text{Th}$ isotope ratios by the isotope dilution method, respectively (Nyachoti, 2016). Activity ratios for ($^{234}\text{U}/^{238}\text{U}$) and ($^{230}\text{Th}/^{232}\text{Th}$) were calculated from measured $^{234}\text{U}/^{238}\text{U}$ and $^{230}\text{Th}/^{232}\text{Th}$ isotope ratios.

The accuracy of U and Th concentrations were assessed relative to the measured BCR2 standard reference material. The measured ($^{234}\text{U}/^{238}\text{U}$)_a and U concentrations for BCR2 were ($^{234}\text{U}/^{238}\text{U}$)_a = 1.003 ± 0.001 and U = 1.691 ± 0.005 ppm (n = 6; 2σ). The results are consistent with the reference values of ($^{234}\text{U}/^{238}\text{U}$)_a = 1.004 ± 0.004 and U = 1.683 ± 0.0017 ppm (Sims et al., 2008; Jochum et al., 2015). The measured ($^{230}\text{Th}/^{232}\text{Th}$)_a and Th concentrations for BCR2 were ($^{230}\text{Th}/^{232}\text{Th}$)_a = 0.868 ± 0.01 and Th = 5.849 ± 0.003 ppm (n = 6; 2σ). The results are in agreeance with the reference values of ($^{230}\text{Th}/^{232}\text{Th}$)_a = 0.877 ± 0.003 and Th = 5.828 ± 0.05 ppm (Sims et al., 2008; Jochum et al., 2015). Age calculations were determined using ISOPLOT 3.75 (Ludwig, 2012) and manually checked using a graphical solution of the $^{230}\text{Th}/^{234}\text{U}$ dating equation: plot of ($^{234}\text{U}/^{238}\text{U}$)_a vs ($^{230}\text{Th}/^{234}\text{U}$)_a for closed systems of varying initial ($^{234}\text{U}/^{238}\text{U}$) (Figure 4.; Ivanovich, 1994).

2.10 REFERENCES

Aitken, M., 1990, Science-based dating in archaeology (294 pp.). London: Longman.

Aitken, M.J., 1998, An introduction to optical dating: The dating of Quaternary sediments by the use of photon-stimulated luminescence: Oxford, University Press, 267 p.

- Alves, E.Q., Macario, K., Ascough, P. and Bronk Ramsey, C., 2018. The worldwide marine radiocarbon reservoir effect: definitions, mechanisms, and prospects. *Reviews of Geophysics*, 56(1), pp.278-305.
- Armour-Finch, L., 2014, Long term deformation in the Rio Grande Rift as inferred from topography and uplifted terraces. The University of Texas at El Paso, United States – Texas.
- Armour, L.K., Langford, R.P., and Ricketts, J.W., 2018, Pliocene—Holocene deformation in the southern Rio Grande rift as inferred from topography and uplifted terraces of the Franklin Mountains, southern New Mexico and western Texas: *Geosphere*, v. 14, p. 1677-1689, <https://doi.org/10.1130/GES01572.1>.
- Avila, V.M., Doser, D.I., Dena-Ornelas, O.S., Moncada, M.M., and Marrufo-Cannon, S.S., 2015, Using geophysical techniques to trace active faults in the urbanized northern Hueco Bolson, West Texas, USA, and northern Chihuahua, Mexico: *Geosphere*, v. 12, p. 264-280, <https://doi.org/10.1130/GES01228.1>.
- Barton CA, Zoback MD, Moos D (1995) Fluid flow along potentially active faults in crystalline rock. *Geology*, 23, 683–868.
- Birkeland, P.W., 1999, *Soils and Geomorphology*. Oxford University Press, New York, 430
- Bischoff, J.L. and Fitzpatrick, J.A., 1991, U-Series Dating of Impure Carbonates - an Isochron Technique Using Total-Sample Dissolution. *Geochimica Et Cosmochimica Acta*, 55(2): 543-554.
- Bourdon, B., Turner, S., Henderson, G. Lundstrom, C., 2003, Introduction to U-series Geochemistry: doi:10.2113/0520001.

- Brock, A. L. and Buck, B. J., 2009, Polygenetic development of the Mormon Mesa, NV petrocalcic horizons: geomorphic and paleoenvironmental interpretations. *Catena*, 77(1), 65-75.
- Bronk-Ramsey, C. (2009). Bayesian analysis of radiocarbon dates. *Radiocarbon*, 51(1), 337–360.
- Bronk-Ramsey, C., & Lee, S. (2013). Recent and planned developments of the Program OxCal. *Radiocarbon*, 55(2), 720–730.
- Bronk-Ramsey, C. and Beer, M., 2014. Radiocarbon dating in paleoseismology. *Encyclopedia of earthquake engineering*: Springer Berlin Heidelberg, pp.1-11.
- Chabaux F., A.S. Cohen, R.K. O’Nions, and J.R. Hein, 1995. ^{238}U - ^{234}U - ^{230}Th chronometry of Fe- Mn crusts. *Geochimica et Cosmochimica Acta* 59, 633–638.
- Chabaux, F., Riotte, J., and Dequincey., O., 2003, U-Th-Ra fractionation during weathering and river transport: *Reviews in Mineralogy and Geochemistry*, v. 52, p. 533–576.
- Chabaux, F., Bourdon, B., and Riotte, J., 2008, U-series geochemistry in weathering profiles, river waters and lakes. *Radioactivity in the Environment* 13, 49-104.
- Chapin, C.E., Cather, S.M. and Keller, G.R., 1994, Tectonic setting of the axial basins of the northern and central Rio Grande rift, in Keller, G. R., S. M. eds, *Rio Grande rift: Structure, stratigraphy, and tectonic setting*, Geological Society of America Special Paper 291, p.5-25
- Cheng, H., Edwards, R.L., Hoff, J., Gallup, C.D., Richards, D.A., Asmerom, Y., 2000, The half-lives of uranium- 234 and thorium-230. *Chem. Geol.* 169, 17-33.
- Collins, E.W., and Raney, J.A., 1991, Tertiary and Quaternary structure and paleotectonics of the Hueco Basin, Trans—Pecos Texas and Chihuahua, Mexico: The University of Texas at

- Austin, Bureau of Economic Geology Geological Circular 91-2, 44p., <https://doi.org/10.23867/GC9102D>.
- Collins, E. W., Raney, J. A., Machette, M. N., Haller, K. M., and Dart, R. L., 1996, Map and data for Quaternary faults in West Texas and adjacent parts of Mexico: U.S. Geological Survey Open File Report 96-002, ii + 74 p., 1 folded plate, scale 1:750,000.
- Crone, A.J., Haller, K.M. and Maharrey, J.Z., 2009. Evaluation of Hazardous Faults in the Intermountain West Region: Summary and Recommendations of a Workshop (No. 2009-1140). US Geological Survey.
- Dickin, A.P., 1995, Radiogenic Isotope Geology. Cambridge University Press, Cambridge. 490.
- Doser, D.I., 1987, The 16 August 1931 Valentine, Texas, earthquake: evidence for normal faulting in west Texas. Bulletin of the Seismological Society of America, 77(6), pp.2005-2017.
- Dosseto, A., Turner, S.P., and Chappell, J., 2008, The evolution of weathering profiles through time: New insights from uranium-series isotopes. Earth and Planetary Science Letters 274, 359–371.
- Edwards, R.L., Gallup, C.D. and Cheng, H., 2003, Uranium-series Dating of Marine and Lacustrine Carbonates. Reviews in Mineralogy and Geochemistry, 52: 363-405.
- Eswaran, H., Reich, P. F., Kimble, J. M., Beinroth, F. H., Padmanabhan, E., Moncharoen, P., 2000, In: J.M.K. R. Lal and B.A. Stewart. (Editors), Global Climate Change and Pedogenic Carbonates. CRC/Lewis Press, Boca Raton, Fla, 15–26.
- Fetzner, Keith, 1992, The interpretation of principal strains from calcite twins in the Franklin Mountains, Texas, M.S. Thesis, University of Texas at El Paso, El Paso, TX 79968, 51p.

- Gile, L.H., Peterson, F.F., Grossman, R.B., 1966, Morphological and genetic sequences of carbonate accumulation in desert soils. *Soil Science* 101, 347–360.
- Gile, L.H., Hawley, J.W., Grossman, R.B., 1981. *Soils and Geomorphology in the Basin and Range Area of Southern New Mexico—Guidebook to the Desert Project*. New Mexico Bureau of Mines and Mineral Resources, Memoir 39, Socorro, NM.
- Guérin, G., Mercier, N. and Adamiec, G, 2011. Dose rate conversion factors: update. *Ancient TL*, 29 (1), 5-8.
- Hirmas, D.R., Amrhein, C., Graham, R.C., 2010, Spatial and process-based modeling of soil inorganic carbon storage in an arid piedmont. *Geoderma* 154, 486-494.
- Hudson, M.R., and Grauch, V.J.S., eds, 2013, *New Perspectives on Rio Grande Rift Basins: From Tectonics to Groundwater*: Geological Society of America Special Paper 494, 500 p.
- Huntley, D.J., Godfrey-Smith, D.I., Thewalt, M.L.W., 1985, Optical Dating of Sediments. *Nature* 313:105–107.
- Ivanovich, M., 1994. Uranium series disequilibrium: concepts and applications. *Radiochimica Acta*, 64(2), pp.81-94.
- Jochum, K.P., Weis, U., Schwager, B., Stoll, B., Wilson, S.A., Haug, G.H., Andreae, M.O. and Enzweiler, J., 2016. Reference values following ISO guidelines for frequently requested rock reference materials. *Geostandards and Geoanalytical Research*, 40(3), pp.333-350.
- Keaton, J.R, and Barnes, J.R, 1996, Paleoseismic evaluation of East Franklin Mountains fault, El Paso, Texas: Technical report to U.S. Geological Survey, under Contract 1434-94-G-2389, May 10, 1996, 45 p.

- Ku, T.L., Bull, W.B., S.T., F. and Knauss, K.G., 1979, Th²³⁰ -U²³⁴ dating of pedogenic carbonates in gravelly desert soils of Vidal Valley, southeastern California. *Geological Society of America Bulletin*, 90(11): 1063- 1073.
- Langmuir, D. and Herman, J.S., 1980, The Mobility of Thorium in Natural-Waters at Low-Temperatures. *Geochimica Et Cosmochimica Acta*, 44(11): 1753-1766.
- Lal, R. and Kimble., J.M., 2000, Pedogenic carbonates and the global carbon cycle. In: R. Lal, J.M. Kimble, H. Eswaran and B.A. Stewart (Editors), *Global climate change and pedogenic carbonates*. Lewis Publishers, Boca Raton, 1-14.
- Laudicina, V.A., Scalenghe, R., Piscoiotta, A., Parello, F., Dazzi, C., 2013, Pedogenic carbonates and carbon pools in gypsiferous soils of a semiarid Mediterranean environment in south Italy. *Geoderma* 192, 31-38.
- Libby, W. F. (1946). Atmospheric helium three and radiocarbon from cosmic radiation. *Physical Review*, 69, 671–672.
- Lovejoy, E.M.P., 1975, An interpretation of the structural geology of the Franklin Mountains, Texas, in Seater, W. R., Clemons, R. E., and Callender, J. F., eds., *Las Cruces Country: New Mexico Geological Society 26th Annual Field Conference Guidebook*, p. 261–268.
- Ludwig, K.R., 2003, Mathematical-statistical treatment of data and errors for Th-230/U geochronology. *Uranium- Series Geochemistry, Reviews in Mineralogy and Geochemistry*, 52: 631-656.
- Ludwig, K. R. (2012). *Isoplot 3.75: A geochronology toolkit for Microsoft Excel*. Berkeley
- Luo, S.D. and Ku, T.L., 1991, U-Series Isochron Dating - A Generalized-Method Employing Total-Sample Dissolution. *Geochimica Et Cosmochimica Acta*, 55(2): 555-564.

- Machette, M.N., 1978. Dating Quaternary faults in the southwestern United States by using buried calcic paleosols. *J. Res. US Geol. Surv.*, 6(3), pp.369-381.
- Machette, M.N. and Hawley, J.W., 1996, Neotectonics of the Rio Grande rift, New Mexico: Geological Society of America Abstracts with Programs, v. 28, no. 7, p.A-271.
- Machette, M.N., 1998, Contrasts between short- and long-term records of seismicity in the Rio Grande rift—important implications for seismic-hazard assessments in areas of slow extension, in Lund, W.R. (ed.) Basin and Range Province Seismic-Hazards Summit, Proceedings: Utah Geological Survey, Miscellaneous Publication 98-2, p. 84-95.
- Mack, G.H., and Seager, W.R., 1990, Tectonic control on facies distribution of the Camp Rice and Palomas Formations (Pliocene–Pleistocene) in the southern Rio Grande rift: Geological Society of America Bulletin, v. 102, p. 45–53, [https://doi.org/10.1130/0016-7606\(1990\)102<0045: TCOFDO>2.3.CO;2](https://doi.org/10.1130/0016-7606(1990)102<0045: TCOFDO>2.3.CO;2).
- McCalpin, J.P., 2006, Quaternary Faulting and Seismic Source Characterization in the El Paso–Juarez Metropolitan Area: Final Technical Report: Collaborative Research with the University of Texas at El Paso, Program Element II: Evaluate Urban Hazard and Risk, and National Earthquake Hazards Reduction Program. US Geological Survey. (<http://earthquake.usgs.gov/research/external/reports/03HQGR0056.pdf>)
- McCalpin, J.P., Harrison, J.B.J., Berger, G.W., and Tobin, H.C., 2011, Paleoseismicity of a lowslip-rate normal fault in the Rio Grande rift, USA; The Calabacillas fault, Albuquerque, New Mexico, in Audemard, F.A., Michetti, A.M. and McCalpin, J.P. (eds.), Geological Criteria for Evaluating Seismicity Revisited: Forty Years of Paleoseismic Investigations

- and the Natural Record of Past Earthquakes: Geological Society of America Special Paper 479, p. 23-46.
- Monger, H.C., Daugherty, L.A., Lindemann, W.C. and Liddell, C.M., 1991, Microbial precipitation of pedogenic calcite. *Geology*, 19(10), pp.997-1000.
- Monger, H.C., Cole, D.R., Gish, J.W., Giordano, T.H., 1998, Stable carbon and oxygen isotopes in Quaternary soil carbonates as indicators of ecogeomorphic changes in the northern Chihuahuan Desert, USA. *Geoderma* 82(1- 3),137-172
- Monger, H. C., 2006, Soil development in the Jornada Basin. Structure and function of a Chihuahuan Desert ecosystem: The Jornada Basin Long Term Ecological Research site. Oxford Univ. Press, New York, 81-106.
- Monger, H.C., Cole, D.R., Buck, B.J., Gallegos, R.A., 2009, Scale and the isotopic record of C4 plants in pedogenic carbonate: from the biome to the rhizosphere. *Ecology* 90 (6), 1498-1511.
- Monger, H. C., Kraimer, R. A., Cole, D. R., Wang, X., Wang, J., 2015, Sequestration of inorganic carbon in soil and groundwater. *Geology*, 43(5), 375-378.
- Murray, A.S., Wintle, A.G., 2000, Luminescence dating of quartz using an improved single-aliquot regenerative- dose protocol. *Radiation Measurements* 32: 57-73
- Nelson, M.S., Rittenour., T.M., 2015, Using Grain-size Characteristics to Model Soil Water Content: Application to Dose-rate Calculation for Luminescence Dating. *Radiation Measurements*, doi.org/10.1016/j.radmeas.2015.02.016
- Neymark, L.A., 2011, Potential effects of alpha-recoil on uranium-series dating of calcrete. *Chemical Geology*, 282(3-4): 98-112.

- Nyachoti, S.K., 2016, Application of uranium and strontium isotopes as salinity and paleo-environmental conditions tracers: Insight from the Rio Grande River and pedogenic carbonates in drylands soils of Southwest, USA. The University of Texas at El Paso.
- Osmond, J.K., May, J.P., and Tanner, W.F., 1970, Age of the Cap Kennedy barrier-and-lagoon complex. *J. Geophys. Res.* 75, 5459-5468.
- Paces, J.B., and Whelan, J.F., 2012, The paleohydrology of unsaturated and saturated zones at Yucca Mountain, Nevada, and vicinity, in Stuckless, J.S., ed., *Hydrology and Geochemistry of Yucca Mountain and Vicinity, Southern Nevada and California: Geological Society of America Memoir 209*, p. 219-276, doi:10.1130/2012.1209(05).
- Pavlis, T.L., Hurtado, J.M., Alfaro-Diaz, R., Garcia, V.H., McCalpin, J.P., 2017, Quaternary faulting and urban seismic hazards in the El Paso metropolitan area. Final Technical Report: Collaborative Research with the University of Texas at El Paso, Program Element II: Evaluate Urban Hazard and Risk, and National Earthquake Hazards Reduction Program. US Geological Survey.
- Raney, J.A., and Collins, E.W., 1994a, Geologic map of the El Paso quadrangle, Texas: The University of Texas at Austin, [Texas] Bureau of Economic Geology Open-File Map, 1 sheet, scale 1:24,000.
- Raney, J.A., and Collins, E.W., 1994b, Geologic map of the North Franklin Mountain quadrangle, Texas: The University of Texas at Austin, [Texas] Bureau of Economic Geology Open-File Map, 1 sheet, scale 1:24,000.

- Reimer, P., Bard, E., Bayliss, J., Beck, A., Blackwell, J. W., Bronk Ramsey, P. G., et al., 2013, IntCal13 and Marine13 radiocarbon age calibration curves 0–50,000 years cal BP–50,000. *Radiocarbon*, 55(4), 1869–1887.
- Reiners, P.W., Carlson, R.W., Renne, P.R., Cooper, K.M., Granger, D.E., McLean, N.M. and Schoene, B., 2017, Cosmogenic nuclides. In *Geochronology and Thermochronology* (eds P.W. Reiners, R.W. Carlson, P.R. Renne, K.M. Cooper, D.E. Granger, N.M. McLean and B. Schoene). doi:10.1002/9781118455876.ch13
- Rhodes, E.J., 2011, Optically stimulated luminescence dating of sediments over the past 200,000 years. *Annual Review of Earth and Planetary Sciences*, 39, pp.461-488.
- Rosholt, J.N., 1976, $^{230}\text{Th}/^{234}\text{U}$ dating of travertine and caliche rinds, GSA abstr. Prog. 8, 1076.
- Roths, P.J. and Soegaard, K., 1993, Geochemical and geochronological studies of the Grenville-age (1250–1000 Ma) Allamoore and Hazel Formations, Hudspeth and Culberson counties, west Texas. Geological Society of America, Field Trip Guidebook, pp.11-35.
- Scharman, Mitchell R., 2006, Structural constrains on Laramide shortening and Rio Grande rift extension in the central Franklin Mountains, El Paso County, Texas, M.S. Thesis, University of Texas at El Paso, El Paso, TX 79968, 70p.
- Scherschel, C.A., 1995, Quaternary geologic and geomorphic framework for Neotectonic analysis of the northeastern Franklin Mountains, El Paso, Texas: unpublished MS thesis, Texas A&M University, College Station, TX.
- Sharp, W.D., Ludwig, K.R., Chadwick, O.A., Amundson, R. and Glaser, L.L., 2003, Dating fluvial terraces by the $^{230}\text{Th}/\text{U}$ on pedogenic carbonate, Wind River Basin, Wyoming. *Quaternary Research* 59:139–150.

- Sims, K.W.W., J.B. Gill, A. Dosseto, D.L. Hoffmann, C.C. Lundstrom, R.W. Williams, L. Ball, D. Tollstrup, S. Turner, J. Prytulak, J.J.G. Glessner, J.J. Standish, and T. Elliott, 2008. An Inter-Laboratory Assessment of the Thorium Isotopic Composition of Synthetic and Rock Reference Materials. *Geostandards and Geoanalytical Research*, 32 (1), 65-91.
- Smedley, R.K., 2018. Telling the time with dust, sand and rocks. *Elements: An International Magazine of Mineralogy, Geochemistry, and Petrology*, 14(1), pp.9-14.
- Srivastava, P., Bhattacharyya, T. and Pal, D.K., 2002, Significance of the formation of calcium carbonate minerals in the pedogenesis and management of cracking clay soils (Vertisols) of India. *Clays and Clay Minerals*, 50(1), pp.111-126.
- Stacy, John K., 1991, Structural and tectonic history of McKelligon Canyon, El Paso County, Texas, M.S. Thesis, University of Texas at El Paso, El Paso, TX 79968, 75p.
- Stuiver, M., & Polach, H., 1977, Reporting of ^{14}C data. *Radiocarbon*, 19(3), 355–363.
- Tanner, L., 2010, Continental carbonates as indicators of paleoclimate. *Developments in sedimentology*, 62, 181 – 188. ISSN 0070-4571, DOI 10.1016/S0070-4571 (09) 06204-9
- Tsipenyuk, Yuri M., 1997, *Nuclear Methods in Science and Technology*. Bristol, UK: Institute of Physics Publishing.
- Vigier, N., Bourdon B., Turner S., and Allegre, C.J., 2001, Erosion timescales derived from U-decay series measurements in rivers. *Earth and Planetary Science Letters* 193, 485–499.
- Violette, A., Riotte, J., Braun, J., Oliva, P., Marechal, J., Sekhar, M., Jeandel, C., Subramanian, S., Prunier, J., Barbiero, L. and Dupre, B., 2010, Formation and preservation of pedogenic carbonates in Southern Indian, links with paleo-monsoon and pedological conditions:

Clues from Sr isotopes, U-Th series and REEs. *Geochimica et Cosmochimica Acta* 74, 7059-7085.

Von Hake, C.A., 1975, Earthquake history of New Mexico. *Earthquake Information Bulletin* (USGS), 7(3), pp.23-26.

Williams, R.T., R.T., Goodwin, L.B., Sharp, W.D., and Mozley, P.S., 2017, Reading a 400,000-year record of earthquake frequency for an intraplate fault: *Proceedings of the National Academy of Sciences*, v.114, p. 4893- 4898.

Zamanian, K., Pustovoytov, K. and Kuzyakov, Y., 2016. Pedogenic carbonates: Forms and formation processes. *Earth-Science Reviews*, 157, pp.1-17.

2.11 TABLES

Table 2.1 Radiocarbon results of samples collected from unit CV within the BMC trench.

Sample Name	Stratigraphic Unit	Depth (mbmgs)	AMS 14C Date (RCYBP)	$\pm 1\sigma$ (RCYBP)	Calibrated Date (1σ CAL yr. BP)	Calibrated Date (2σ CAL yr. BP)	$\delta^{13}C$ (‰)
EFC-1	CV	0.40	1213	27	1180-270	1260-1060	-15.4
EFC-2	CV	0.65	512	24	540-510	560-500	-12.1

Note: Samples dated PaleoResearch Institute, Crestone, Colorado USA

mbgs = meters below modern ground surface

RCYBP = radiocarbon years before present

CAL yr. BP = calendar years before present

Table 2.2 OSL results of sediment samples collected from various units within the BMC trench.

Sample Name	Stratigraphic Unit	Depth (mbmgs)	Number of Aliquots ¹	Dose Rate (Gy/ka)	\pm	De ² (Gy)	\pm (2 σ)	OD ³ (%)	\pm	OSL Age (ka)	\pm (2 σ)
EFL01-A	H14	3.30	22 (32)	1.55	0.07	166.82	24.67	30.3	5.8	107.96	19.02
EFL02-A	CI	1.90	17 (24)	1.41	0.07	115.33	18.54	30.5	6.1	82.04	15.35
EFL03-A	CI	1.60	17 (28)	1.88	0.09	132.51	14.9	16.4	5	70.41	10.39
EFL04-A	CII	1.20	19 (27)	2.24	0.1	122.48	15.02	23.1	4.9	54.68	8.51
EFL05-A	CIII	0.70	16 (33)	1.15	0.06	50.6	9.89	35.5	7.5	43.82	9.52
EFL06-A	CIV	0.35	19 (28)	1.52	0.07	60.61	9.59	15.1	4.4	39.89	7.36
EFL07-A	H16	1.90	16 (35)	2.54	0.11	159.47	15.52	11.7	4.8	62.86	8.59
EFL08-A	14	0.55	19 (38)	1.77	0.08	138.47	14.48	11.2	6.3	78.05	11.00

Note: Samples dated at Utah State University Luminescence Laboratory; North Logan, Utah USA

¹Age analysis using the single-aliquot regenerative dose procedure of Murray and Wintle (2000) on 1 mm small aliquots of quartz sand. Number of aliquots used in age calculation and number of aliquots analyzed in parentheses.

²Equivalent dose (DE) calculated using the Central Age Model (CAM) of Galbraith and Roberts (2012), unless otherwise noted.

³Overdispersion (OD) represents variance in DE data beyond measurement uncertainties, OD >20% may indicate significant scatter due to depositional or post-depositional processes.

⁴DE calculated using the Minimum Age Model (MAM) of Galbraith and Roberts (2012).

Table 2.3 U-series, C, and O Isotope results of sediment samples collected from various units within the BMC trench.

TABLE 3. U-SERIES RESULTS

Sample Name	Stratigraphic Unit	Depth (mbmgs)	²³⁸ U	²³² Th	Measured Activity Ratios						²³⁴ U/ ²³⁸ U _i ± 2se		Age (ka)	± (2σ) (‰; VPDB)	δ ¹³ C (‰; VPDB)	±	δ ¹⁸ O (‰; VPDB)	±	
			(ppm)	(ppm)	²³⁴ U/ ²³⁸ U _m	±	²³⁰ Th/ ²³⁸ U _m	±	²³² Th/ ²³⁸ U _m	±	nd	nd							
EFU-01O	CV	0.00	nd	nd	nd	nd	nd	nd	nd	nd	nd	nd	nd	nd	nd	nd	nd	nd	nd
EFU-02O	CIV	0.20	nd	nd	nd	nd	nd	nd	nd	nd	nd	nd	nd	nd	nd	nd	nd	nd	nd
EFU-03O			1.23	2.66	1.309	0.007	0.819	0.008	0.705	0.008									
EFU-03L	CIV	0.40	0.36	0.42	1.831	0.009	0.657	0.007	0.385	0.005	2.57	0.43	21.2	5.7	-5.00	0.01	-6.71	0.02	
EFU-03R			0.80	1.98	1.099	0.005	0.905	0.009	0.816	0.010									
EFU-04O			1.27	2.24	1.369	0.007	0.767	0.008	0.575	0.007									
EFU-04L	CIII	0.70	0.48	0.46	1.786	0.009	0.609	0.006	0.314	0.004	1.73	0.47	22.9	6.8	-5.26	0.01	-7.19	0.04	
EFU-04R			0.77	1.87	1.086	0.005	0.885	0.009	0.800	0.010									
EFU-05O			0.80	0.87	1.400	0.007	0.578	0.006	0.357	0.004									
EFU-05L	CII	0.90	0.48	0.27	1.605	0.008	0.476	0.005	0.182	0.002	2.18	0.33	24.3	3.8	-6.38	0.01	-8.96	0.03	
EFU-05R			0.36	0.79	1.077	0.005	0.812	0.008	0.720	0.009									
EFU-06O			1.20	2.87	1.278	0.006	0.612	0.010	0.379	0.009									
EFU-06L	CII	1.30	0.24	0.54	1.486	0.008	0.557	0.014	0.235	0.009	1.60	0.12	32.9	9.4	-6.00	0.01	-8.06	0.01	
EFU-06R			0.97	2.42	1.197	0.006	0.776	0.010	0.619	0.010									
EFU-07O			0.77	3.24	1.180	0.006	0.505	0.022	0.347	0.025									
EFU-07L	H15/CI	1.60	0.44	1.28	1.314	0.008	0.416	0.005	0.182	0.002	1.31	0.34	36.3	4.1	-4.72	0.01	-6.34	0.01	
EFU-07R			0.52	2.34	1.057	0.005	0.654	0.009	0.893	0.012									
EFU-09O			1.18	0.37	1.690	0.008	0.296	0.003	0.102	0.001									
EFU-09L	Fissure Fill	-	0.85	0.08	1.779	0.009	0.186	0.002	0.030	0.000	1.80	0.28	12.1	3.6	-5.63	0.01	-8.49	0.01	
EFU-09R			0.30	0.44	1.479	0.007	0.550	0.006	0.480	0.006									
EFU-10O			0.99	0.53	1.665	0.008	0.441	0.004	0.176	0.002									
EFU-10L	Gouge Zone	-	0.65	0.10	1.788	0.009	0.245	0.002	0.048	0.001	1.85	0.06	10.6	0.6	-5.60	0.01	-7.82	0.03	
EFU-10R			0.35	0.47	1.421	0.007	0.843	0.008	0.436	0.005									

Note: Samples dated at Center for Earth and Environmental Isotope Research, El Paso, Texas USA
O = original/bulk, L = leachate, R = residue
mbmgs = meters below modern ground surface

2.12 FIGURES

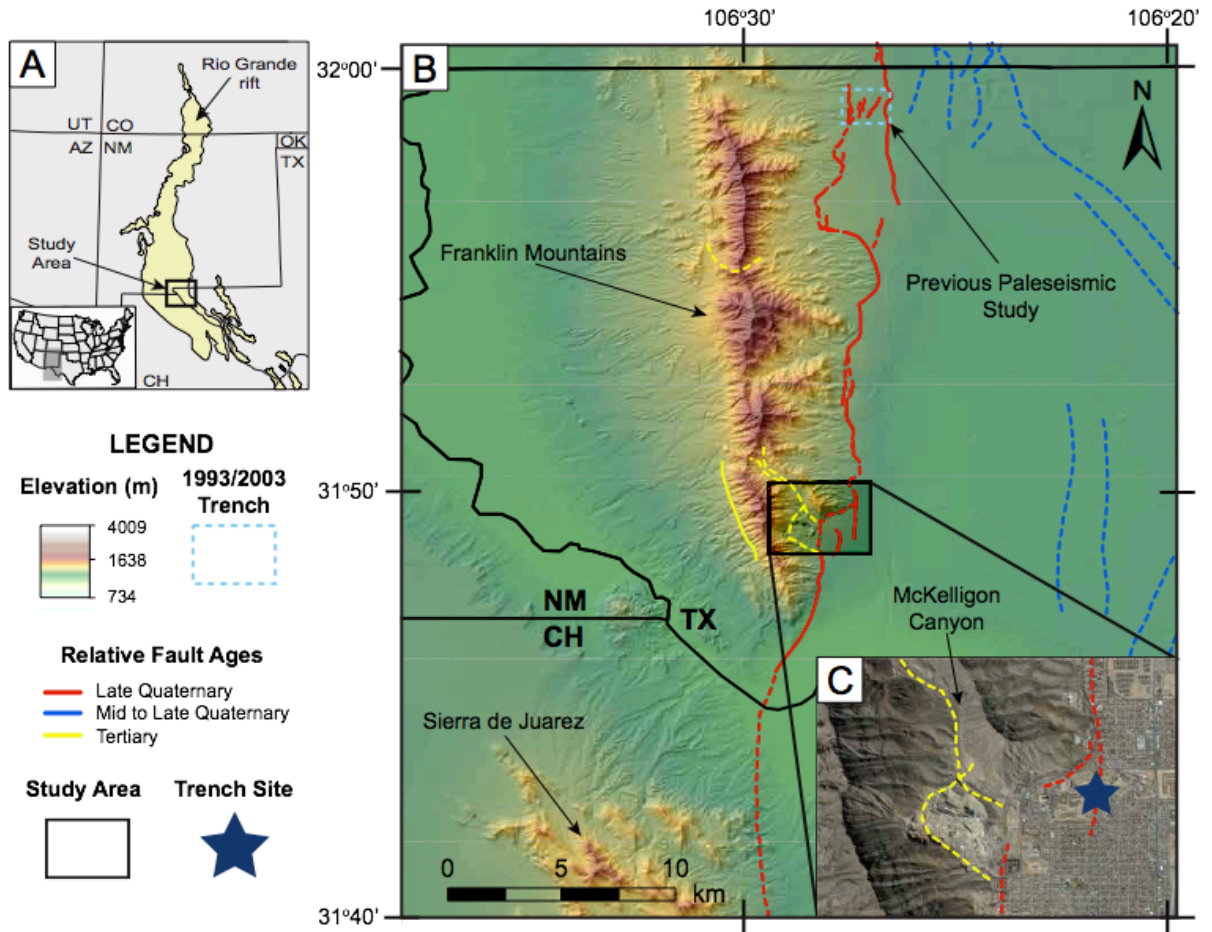


Figure 2.1 A) Regional map showing alluvial basins of the Rio Grande rift in yellow and location of study area. 1993/2003 trench site by Keaton and Barnes, 1996 and McCalpin, 2006. B) Digital elevation model of the Paso del Norte region with fault traces shown in various colors (refer to Relative Fault Ages legend; USGS Earthquake Hazards Program). Red dashed/solid line = trace of East Franklin Mountain fault (EFMF); TX = Texas; NM = New Mexico; CH = Chihuahua. C) Satellite image of trench location relative to EFMF.

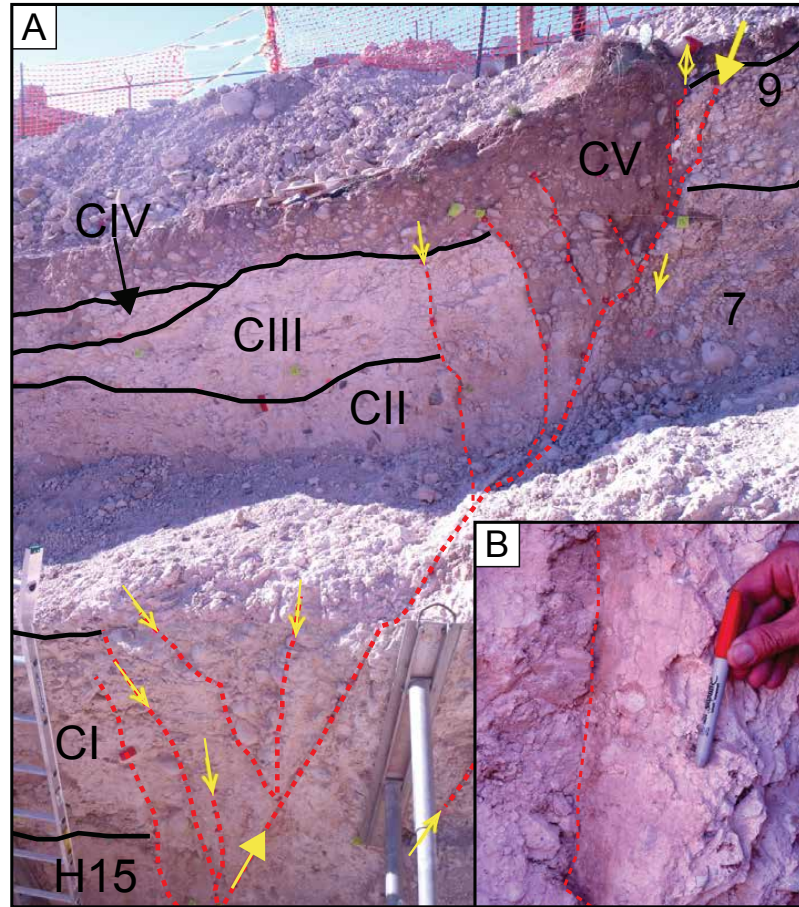


Figure 2.2 A) Image of main fault zone exposed on the south wall. Shoring rails are 20 cm wide. Large yellow arrows = main fault, smaller yellow arrows = minor faults, CV = no pedogenic carbonates present; poorly sorted gravel, CIV = stage 3 pedogenic carbonates, CIII = stage 3 pedogenic carbonates; matrix supported pebbles, CII = stage 3 pedogenic carbonates; matrix supported gravel, CI = stage 3 pedogenic carbonates; contains boulders. B) Slickenside carbonates on main fault plane.

East Franklin Mountain Fault Log of South Wall Trench

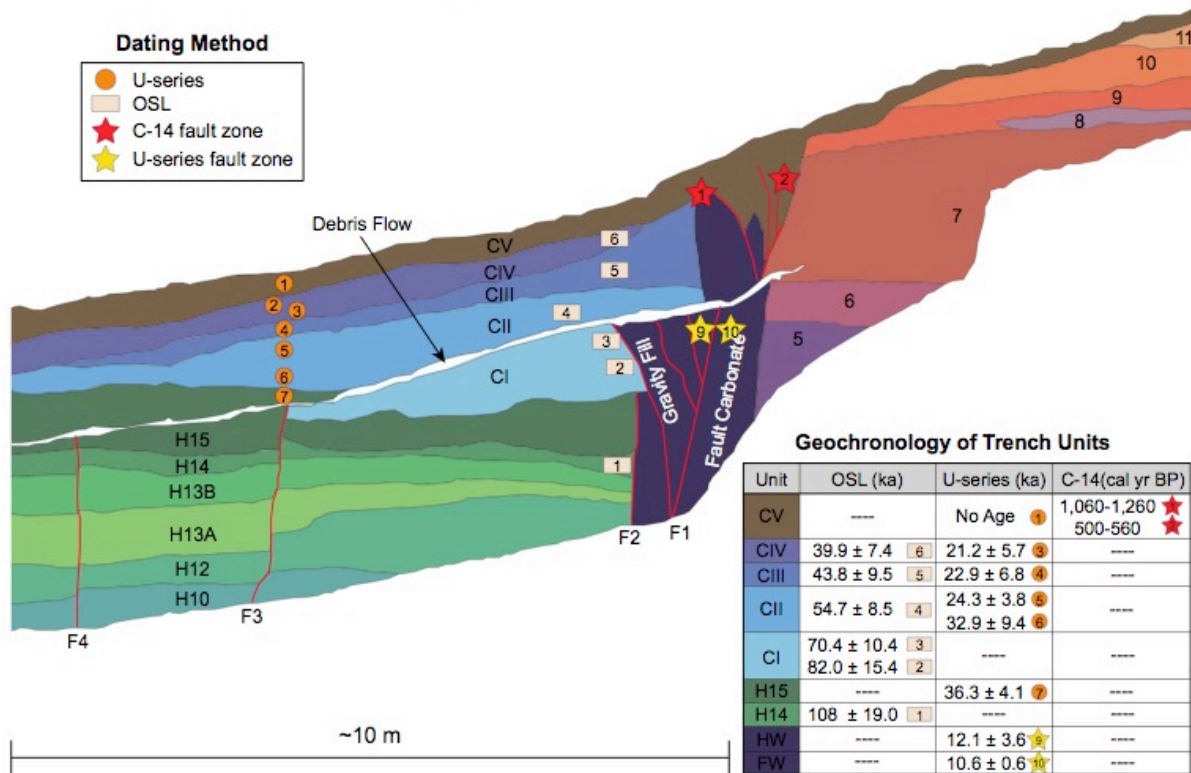


Figure 2.3 Log of the south wall of the Beaumont Medical Center trench showing locations of dated samples. Refer to Pavlis et al., 2017 for detailed unit descriptions and expanded log of the south wall. Red lines = faults and --- = no sample collected on Geochronology of Trench Units table. Sample EFU2 (U-series) was collected but not dated. EFU3 was collected from the same unit and dated.

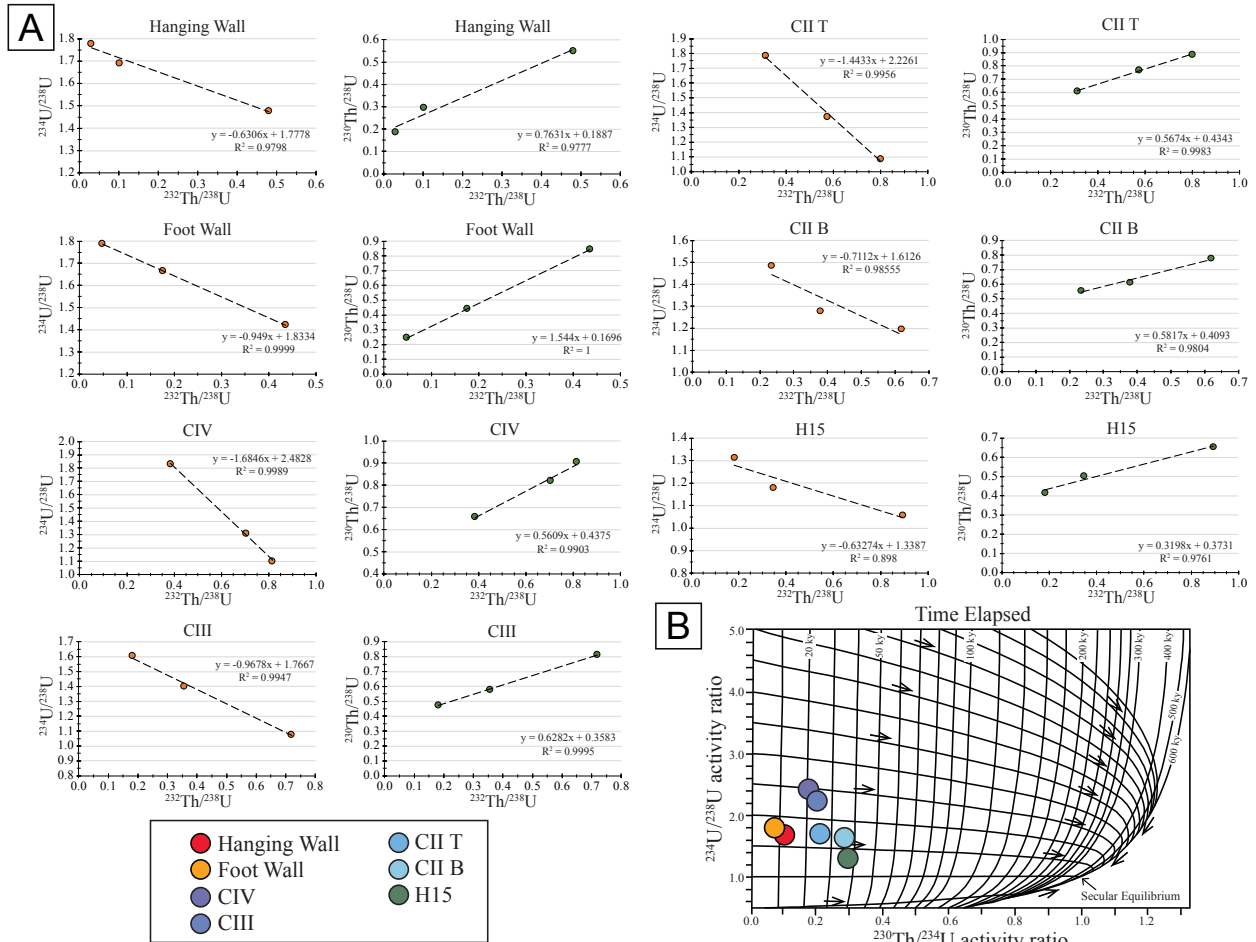


Figure 2.4 A) ($^{234}\text{U}/^{238}\text{U}$) vs ($^{232}\text{Th}/^{238}\text{U}$) and ($^{230}\text{Th}/^{238}\text{U}$) vs ($^{232}\text{Th}/^{238}\text{U}$) isochrons used to show the correction of detrital ^{230}Th in pedogenic carbonates collected from the fault zone. B) U-series evolution diagram with respective dated samples after detrital ^{230}Th correction (various colored circles). Approximate ages determined using $^{234}\text{U}/^{238}\text{U}$ initial and $^{230}\text{Th}/^{238}\text{U}$ initial from isochrons estimated in Fig. 4A. U-series ages determined using Berkeley Geochronology Center's Isoplot software v.3.75.

Chapter 3: Travertine deposits of the Lucero Uplift, New Mexico: Geochemical record of neotectonic and mantle activity in the Santa Fe fault zone

Victor H. Garcia^{1*}, Lin Ma¹, and Jason Ricketts¹

¹Department of Geological Sciences, The University of Texas at El Paso, 500 West University Ave. El Paso, TX. 79968

** Corresponding author vhgarcia4@miners.utep.edu*

3.1 ABSTRACT

Fluids in fault zones contain a mixture of shallow and deeply derived sources, making the flow patterns highly variable in time and space. Determining the relative influences of tectonic and climate activity on fluid flow in fault systems is therefore a great challenge. Travertine deposits preserve an invaluable record of past and current fluid flow in the Rio Grande rift. Travertine deposits and travertine-precipitating springs are especially abundant along the western margin of the Rio Grande rift in central New Mexico. The goal of this study was to reconstruct spatial and temporal patterns in travertine deposition associated with tectonic and climatic influences along the Lucero Uplift (~30 km west of Los Lunas, NM).

U-series ages of travertine deposits in the Lucero Uplift indicate that formation has been active since at least ~600 ka. Travertine ages range from 0.94 ± 0.01 to 592 ± 110 ka. The Santa Fe fault has not been active since at least 490 ± 52 to 592 ± 110 ka (2σ) based on undeformed travertine deposits overlying tilted Santa Fe Group units in two sections of our study area. The majority of the travertine deposits in our study formed during both glacial and interglacial periods. We find minimal evidence to attribute paleoclimate cycles to travertine formation in the Lucero Uplift. This is supported by varying travertine precipitation rates (0.08- 53 mm/ka), which show no correlation with climatic cycles. However, we do not fully dismiss the role of paleoclimate on travertine

formation due to the need of fluids in the subsurface, which are controlled by paleo-hydrologic conditions.

$\delta^{13}\text{C}$ values range 2‰ to 9‰, $^{87}\text{Sr}/^{86}\text{Sr}$ values range from 0.714 to 0.717, and $(^{234}\text{U}/^{238}\text{U})_i$ values range from 3.6 to 9.3, indicative of fluid-rock interaction during deep crustal circulation in more radiogenic basement rock. Our data and interpretations suggest that travertine formation is driven by tectonic (Rio Grande rift) and regional mantle/magmatic (Jemez Upwelling) controls. The results presented here confirm that travertine deposits provide important insights into paleo-fluid sources along major fault zones.

3.2 INTRODUCTION

Travertine is a chemically precipitated terrestrial calcite mineral (CaCO_3) that forms through the evasion of CO_2 from Ca-rich fluids (Pentecost, 2005). Travertine deposits and actively precipitating travertine springs are ubiquitously found along faults, fractures, and/or magmatically active regions around the world (Pentecost, 2005; Faccena et al., 2008; Zentmyer et al., 2008; Brogi et al., 2009; Uysal et al., 2009; De Filippis et al., 2013). Consequently, in many cases, travertine formation is attributed to tectonic and/or magmatic controls, where deep faults and fractures act as conduits allowing deeply derived fluids, rich in CO_2 , to reach the surface and precipitate as travertine (Crossey et al., 2006; Uysal et al., 2007; Brogi et al., 2010; Crossey et al., 2011). Some studies also attribute travertine formation, at both global and regional scales, to variability in climate conditions (e.g. glacial vs interglacial), suggesting that travertine-precipitating systems may be linked to water availability (e.g., Ricketts et al., 2019). However, this hypothesis is problematic because the linkage between water availability and travertine formation is ambiguous: some authors find evidence for high travertine precipitation rates during wetter interglacial periods (Frank et al., 2000; Faccenna et al., 2008; Kampman et al., 2012; Priewisch et

al., 2014; Priestley et al., 2018), whereas others note high travertine precipitation rates during dryer glacial periods (Uysal et al., 2009, 2011; Brogi et al., 2010; Özkul et al., 2013), or high travertine deposition rates during glacial to interglacial transitions (Ricketts et al., 2019).

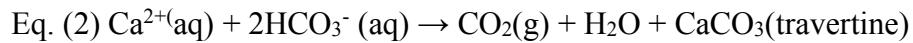
Regardless of their tectonic, magmatic, or climatic origins, travertine deposits serve as valuable records of paleo-fluid flow that operate on various timescales in the upper crust. Paleo and modern fluid flow systems are highly important but challenging to understand, due to the interactions and feedbacks between tectonics and climate, as well as their relative influences on sub-surface flow paths and rates. In this study, we use uranium-series (U-series) dating techniques to determine ages of travertine deposits within the Lucero Uplift, located at the margin of the Rio Grande rift and Colorado Plateau in central New Mexico, USA, and to improve our understanding of the relative influences of tectonic and climate controls on travertine formation. Additionally, we use geochemical isotope tracers (i.e. U, Sr, C, and O isotopes) to investigate fluid sources (shallow vs deep) and how they might change through time. We find that travertine precipitation is dependent on mantle derived CO₂ and deep penetrating faults associated with the Jemez Lineament and Rio Grande rift, respectively.

3.3 BACKGROUND

3.3.1 Travertine Formation

Fluids capable of forming travertine generally originate at depth and are highly concentrated in CO₂, as well as other dissolved inorganic carbon species (HCO₃⁻ and CO₃²⁻). Along their flow paths towards the surface, carbonic acid (H₂CO₃) is produced when CO₂ combines with water, which enables these fluids to leach Ca²⁺ ions from Ca-rich units (e.g. limestone units; Equation 1). Subsequent degassing of CO₂ follows as fluids reach near surface environments with

lower $p\text{CO}_2$, leading to oversaturation of Ca^{2+} and HCO_3^- ions, which in turn facilitate the formation of travertine (Equation 2; after Pentecost, 2005; Crossey et al., 2011):



$\text{CO}_2(\text{g})$ from Equation (1) is externally derived and commonly obtained from deep geologic sources and/or in association with shallow geothermal systems, and transported along fault systems (Newell et al., 2005; Pentecost, 2005; Crossey et al., 2006; Crossey et al., 2011; Priewisch et al., 2014).

It is the travertine formation process (Eq. 1 and 2) and its association with fault zones that makes studying travertine deposits an important topic in a variety of fields in the geosciences. In particular, dating travertine deposits not only provides information on the timing of formation but can also provide information on paleo-fluid conditions, such as fluid sources and pathways, which can be influenced by tectonics and/or climate. In addition, the study of travertine deposits allows for detailed investigations into sources of fluids through time, which can also be used to study links between magmatism, mantle degassing, modern groundwater systems, denudation rates, incision rates, and climate change transitions (Pentecost, 1995; Pentecost, 2005; Faccenna et al., 2008; Uysal et al., 2009; Crossey et al., 2011; Kampman et al. 2012, De Filippis et al. 2013; Priewisch et al., 2014; Berardi et al., 2016; Ricketts et al., 2019). Many dated travertine deposits around the world range from 0.21 to 730 ka (Ricketts et al., 2019), spanning multiple glacial cycles and coinciding with some regional tectonic events. Older travertine deposits (> 730 ka) exist but their ages cannot be accurately determined because the vast majority of travertine studies employed the U-series dating method, which has an upper age limit of ~ 600 ka.

3.3.2 Tectonic vs. Climate Controls on the Formation of Travertine

Travertine deposits are often layered, reflecting systematic deposition through time. Thus, each individual layer is an important record of past fluid flow that is intricately linked to tectonics, climate, or both through time. Currently, two end-member models are used for explaining temporal and spatial changes in travertine precipitating fluid sources zones.

The first model attributes tectonics as the major control of travertine precipitation, where its formation is due to the degassing of CO₂ along deeply penetrating faults that transport CO₂ rich fluids to the surface (Hancock et al., 1999; Temiz et al., 2009; Uysal et al., 2009; Frery, 2012). For example, in central New Mexico, numerous authors have documented fault-controlled travertine deposition (Ricketts et al., 2014; Williams et al., 2015; Williams et al., 2017a; Williams et al., 2017b; Williams et al., 2018). In particular, Williams et al. (2017) documented differences in $\delta^{18}\text{O}$, $\delta^{13}\text{C}$, and $^{87}\text{Sr}/^{86}\text{Sr}$ ratios from fault zone calcite cements, which form in a similar manner to travertine, in different regions of the Rio Grande rift. These authors suggest that deeply-penetrating faults act as conduits for more isotopically evolved deep fluids while shallow intra-basinal faults generally transmit fluids from shallow meteoric origin reservoirs. In addition, Williams et al. (2017) were able to quantify the earthquake history (spanning 400 kyrs) of the Loma Blanco fault in New Mexico fault using calcite veins. Stable isotope data ($\delta^{18}\text{O}$ and $\delta^{13}\text{C}$) from that study indicated rapid CO₂ degassing during seismic events.

Alternatively, other studies suggest that climate may be the main control on travertine precipitation, where formation can be linked with global climate cycles that control water availability and hydrodynamic conditions (Szabo et al., 1990; Crossey et al., 2011; Kampman et al., 2012; Priewisch et al., 2014). For example, Kampman et al. (2012) utilized a $\delta^{18}\text{O}$ and $\delta^{13}\text{C}$ Rayleigh distillation model to infer how fluids evolved through time related to climate cycles, but

failed to address how these systems might vary spatially with respect to fault locations. To further address this issue, Ricketts et al. (2019) compiled 1649 published travertine ages from around the globe to test the climate hypothesis that global (and/or regional) changes in climate regulate travertine formation. They observed higher peaks of travertine formation, at both global and regional scales, during glacial terminations or interglacial periods and attribute this observation to the higher groundwater recharge rates during wetter conditions.

In addition to the above two end-member travertine formation models, many travertine-depositing systems may be controlled by a combination of tectonics, climate and magmatism (Pentecost, 2005; Brogi et al., 2010; Ozkul et al., 2013; Priewisch et al., 2014).

3.3.3 Geologic Setting of Rio Grande rift

Many travertine deposits in New Mexico occur along two major tectonic features, the Rio Grande rift and the Jemez lineament (Figure 1A; Barker et al., 1996; Dunbar, 2005). Travertine deposits and active travertine precipitating springs are especially abundant in the central portion of the Rio Grande rift near active magmatism (e.g. Socorro magma body), past volcanism (e.g. Valles Caldera and other Jemez Lineament volcanics) and are associated with active major rift bounding faults (e.g., Santa Fe fault; Figure 1; Goff and Shevenell, 1987; Crossey et al., 2011; Priewisch et al., 2014; Ricketts et al., 2014). Magmatic and tectonic activity in the Rio Grande rift is thought to provide a source for both mantle-derived CO₂ and ³He and the conduits necessary for travertine formation at the surface (Newell et al., 2005; Williams et al., 2013; Priewisch et al., 2014).

The Rio Grande rift consists of a belt of north-south trending asymmetrical *en echelon* basins, bounded by normal faults, that stretch ~1000 km from central Colorado, USA to northern Chihuahua, Mexico (e.g. Chapin, 1979; Baldrige et al., 1984; Sharman et al., 2006;). Based on

patterns in magmatism and sedimentation, the Rio Grande rift was actively extending by 30-32 Ma (Morgan et al., 1986) and extension is ongoing today at relatively slow rates of ~0.1 mm/kyr (Berglund et al., 2012).

In north-central New Mexico, where many travertine deposits are located, the Rio Grande rift intersects the Jemez Lineament, a northeast-trending belt of late Cenozoic volcanic fields. The Jemez Lineament is attributed to the presence of a long-lived, northeast-trending intercontinental tectonic and magmatic zone that may have initially formed as a Proterozoic accretionary boundary; although that the exact origin of the Jemez Lineament is still under debate (Figure 1; Aldrich, 1986; Shaw and Karlstrom, 1999; Chapin et al., 2004; Dunbar, 2005; Channer et al., 2015). Additionally, Sosa et al. (2014) identified a low velocity zone, which they term the Jemez Upwelling, beneath the Jemez Lineament that likely feeds the volcanic features in the region. The most notable volcanic feature located at this intersection (~120 km north of our study area) is Valles Caldera, which was produced by a series of rhyolitic-pyroclastic eruptions at 1.6 and 1.2 Ma (Dunbar, 2005). In south-central New Mexico, the Rio Grande rift is intersected by the Socorro magma body, a thin~20 km deep mid-crustal magma sheet. This distinct feature is associated with numerous small magnitude earthquakes events per year, locally known as the Socorro seismic anomaly (Sanford et al., 1977; Reiter et al., 2010).

3.3.4 Geological Setting of the Lucero Uplift

The study area is located ~30 km west of Los Lunas, New Mexico in a region known as the Lucero Uplift (Figure 1 and 2). The Lucero Uplift is a transitional, 1-2 km wide, north-south trending zone along the boundary of the Colorado Plateau and the Rio Grande rift in central New Mexico (Duschatko, 1953). Extension in the area is mainly concentrated along the east-dipping Santa Fe fault, which marks the western edge of the Rio Grande rift. The Santa Fe fault separates

the relatively undeformed Paleozoic and Mesozoic strata of the Colorado Plateau to the west from the Cenozoic Santa Fe Group rift fill units to the east (May and Russell, 1994; Priewisch et al., 2014; Ricketts et al., 2014). Numerous synthetic and antithetic faults to the Santa Fe fault emerge in the northern section of our study area (Ricketts and Karlstrom, 2014).

Active travertine precipitating springs and thick travertine deposits are located along a 10 km trace of the Lucero Uplift (Figure 1B, 2; Ricketts and Karlstrom, 2014). These travertine deposits and springs straddle the Santa Fe fault and cover much of the older strata and structure as well. The close association of these travertine deposits with rift-related structures, and the existence of nearby active travertine-depositing springs within arroyos along multiple fault strands, suggests that these platforms were deposited from spring waters emanating from the Santa Fe fault system (Ricketts and Karlstrom, 2014). Large volume travertine deposits of the Lucero Uplift are currently inactive but smaller actively precipitating travertine springs are generally found at low elevations (Figure 2B). At some locations, active precipitation is occurring along the margins of older and larger travertine deposits (Figure 2C). Both active and inactive travertine deposits have similar dams, coatings, drapes, and travertine facies (Figure 2C and 2D). Extensional calcite-filled veins are also observed in these travertine deposits, suggesting that deformation related to continued movement along the Santa Fe fault system is younger than ~250 ka (Ricketts et al., 2014).

Recent work on fault-precipitated calcite, travertine deposits, and travertine precipitating springs near our study area indicate that source fluids are a mixture of meteoric and deeply sourced fluids (Goff and Shevenell, 1987; Crossey et al., 2011; Williams et al., 2015). Previous studies show that these fluids are transported to the surface along basement penetrating faults such as the Santa Fe fault (Crossey et al., 2006; Crossey et al., 2009; Williams et al., 2013). These travertine-

forming fluids are rich in dissolved CO₂ and some contain ³He. These gases, specifically ³He, are interpreted to be primordial and isotopically abundant in the mantle (Newell et al., 2005; Crossey et al., 2011). Their large presence in non-air contaminated fluids at spring vents indicate these volatiles are likely sourced from the lower crust and mantle and are brought to the surface through seismic events or along deeply-penetrating faults (Ballentine et al, 2001; Priewisch et al., 2014; Ricketts et al., 2014; Williams et al., 2015; Williams et al., 2017).

3.3.5 Uranium-series (U-series) Chronometer and Geochemical Tracers

3.3.5.1 U-series Dating and (²³⁴U/²³⁸U)_i ratios

The U-series dating technique is a conventional and reliable method for constraining the formation ages of Ca-carbonate materials that have high U/Th elemental ratios (Goff and Shevenell, 1987; Hancock et al., 1999; Uysal et al., 2007; Faccenna et al., 2008; Crossey et al., 2011; Nuriel et al., 2012; Priewisch et al., 2014; Williams et al., 2017). This method relies on the decay series of ²³⁴U to ²³⁰Th, both of which have relatively short half-lives (²³⁴U_{1/2T} = 245 kyr, ²³⁰Th_{1/2T} = 75 kyr) compared to the parent isotope ²³⁸U in this long decay chain (Dickin, 1995; Cheng et al., 2000). The decay sequence of ²³⁸U-²³⁴U-²³⁰Th reaches secular equilibrium (i.e. daughter decay rate is equal to daughter isotope being produced from decay of parent isotope) if the system remains undisturbed or closed for longer than 1.25 Myr (Edwards et al., 1987). Hence the disequilibrium of the ²³⁸U-²³⁴U-²³⁰Th will allow for calculating time information of the system since its last disturbance or formation of new carbonates within the last 1.25 Ma. Correction procedures of detrital Th inputs for U-series dating are generally not necessary if detrital ²³⁰Th and ²³²Th was not present in the material at the time of formation (U/Th ratio is high) (Luo and Ku, 1991; Ivanovich and Harmon, 1992). The changes of activity ratios towards secular equilibrium allows for the calculation of both ages (upper limit ~600 ka under current analytical precision) and

initial U activity ratios, herein referred as $(^{234}\text{U}/^{238}\text{U})_i$, the ratio of $(^{234}\text{U}/^{238}\text{U})$ at the time of formation (Bourdon et al., 2003; Chabaux et al., 2003).

Due to the high solubility of U in oxidizing environments and preferential leaching of ^{234}U over ^{238}U into weathering fluids, which are easily released into solutions due to production by alpha recoil mechanisms and damaged mineral lattices, deep crustal fluids and groundwater usually have high $(^{234}\text{U}/^{238}\text{U})$ ratios greater than 1 (Kronfeld et al., 1975; Fleisher, 1980). Hence, Ca-carbonate materials that precipitate from these fluids will inherit the same $(^{234}\text{U}/^{238}\text{U})_i$ of the environment from which they formed at the time of formation. After formation, $(^{234}\text{U}/^{238}\text{U})$ ratios in Ca-carbonate materials will change with time toward the secular equilibrium but the initial $(^{234}\text{U}/^{238}\text{U})$ ratios can be back calculated from the U-series dating procedure. As deeper fluid sources normally carry distinctively higher $(^{234}\text{U}/^{238}\text{U})$ ratios than shallow fluids (Chabaux et al., 2003; Durand et al., 2005), $(^{234}\text{U}/^{238}\text{U})_i$ is an ideal tracer to distinguish between shallow fluid sources (surface water and shallow groundwater; e.g., $(^{234}\text{U}/^{238}\text{U})_i < 3$) and deep fluid sources (e.g., $(^{234}\text{U}/^{238}\text{U})_i > 3$), as well as changes of contributing fluid sources with time.

3.3.5.2 Strontium Isotope Ratios ($^{87}\text{Sr}/^{86}\text{Sr}$)

The $^{87}\text{Sr}/^{86}\text{Sr}$ ratios in Ca-carbonate materials reflect the sources of the fluids from which they precipitate (Crossey et al., 2006; Williams et al., 2015; Garcia, 2017). This is because Sr is highly soluble and readily substitutes for Ca in Ca-rich minerals. Furthermore, $^{87}\text{Sr}/^{86}\text{Sr}$ isotopic ratios do not fractionate by weathering or mineral precipitation (Pett-Ridge et al., 2009, Paces and Wurster, 2014; Crossey et al., 2015; Zielinski et al., 2016). Sr is released into fluid systems naturally through the weathering of bedrock or sediment sources. More specifically, different rocks develop different $^{87}\text{Sr}/^{86}\text{Sr}$ ratios due to differences in ages, Rb/Sr ratios, and water-rock interactions through flowing water (Bullen et al., 1996). For instance, $^{87}\text{Sr}/^{86}\text{Sr}$ ratios can be used

to distinguish between silicate and carbonate formation waters (Clark and Fritz, 1997; Pett-Ridge et al., 2009). The differing rock types found in our study area make Sr isotopes ideal tracers to identify different geologic and fluid sources.

3.3.5.3 Carbon and O Isotope ratios ($\delta^{18}\text{O}$ and $\delta^{13}\text{C}$)

Stable $\delta^{13}\text{C}$ and $\delta^{18}\text{O}$ isotope compositions for travertines, and most other geological materials such as corals and cave carbonates, reflect the source of CO_2 , fluids, and precipitation conditions of the fluids from which they form (Epstein et al., 1953). In travertine deposits, the $\delta^{13}\text{C}$ and $\delta^{18}\text{O}$ compositions exhibit the widest range of isotopic compositions of any geologic material (Pentecost, 2005; Sharp et al., 2007). For example, the carbon component in travertines is mainly derived from external CO_2 (e.g. mantle or deep crustal CO_2 in Equation 1) and primary carbonate material (e.g. limestone in Equation 1) resulting in a wide range of possible compositions; other sources of carbon are also possible (e.g. addition of soil CO_2 , atmospheric CO_2 , and organic carbon). Interpretation of $\delta^{18}\text{O}$ compositions in travertines are generally less straightforward than $\delta^{13}\text{C}$ compositions but still provide useful information regarding precipitation conditions such as sources of fluid including meteoric, magmatic, and crustal fluids (Pentecost, 2005; Giustini et al., 2018). In addition to tracing the different sources of fluids, both $\delta^{13}\text{C}$ and $\delta^{18}\text{O}$ compositions in travertine deposits reflect precipitation history or possible outgassing history during which the open system C and O fractionation (such as Rayleigh fractionation) generates additional variability for $\delta^{13}\text{C}$ and $\delta^{18}\text{O}$ compositions as commonly recorded in carbonate materials such as travertine deposits (e.g., Kampman et al., 2012).

3.4 METHODS

3.4.1 Travertine Sample Selection

A total of 45 individual travertine samples were collected along a 10 km trace of the Santa Fe fault. Travertine samples in the northern section of the study area were collected from low (basin floor) and high (Lucero Uplift) elevation areas along east- and west-dipping faults within the Santa Fe fault zone (Figure 2). Travertine samples in the southern section of our study area were collected from low and high elevation areas located at or near the main exposure of the Santa Fe fault. Travertine samples collected at lower elevations are generally near the vicinity of active travertine precipitating springs. Travertine samples collected at higher elevations are typically from older travertine platforms that are not associated with travertine precipitating springs. Of these 45 samples, 26 representative samples were selected for geochronological and geochemical analyses. These samples consist of dense mm- to cm-scale layered travertine made up of either micritic or sparry calcite (Fig. 3). Layers varied from opaque to milky white in color with little to no observed detrital material (Table 1). Travertine layers were micro-drilled to provide enough powder (~1 g) for U-series age analysis, $(^{234}\text{U}/^{238}\text{U})_i$, $^{87}\text{Sr}/^{86}\text{Sr}$, $\delta^{13}\text{C}$, and $\delta^{18}\text{O}$ isotope analyses. In general, two to four individual travertine layers were analyzed for certain representative travertine samples (Figure 3), which resulted in a total of 58 individual data points.

3.4.2 U-series Isotope Analysis

Travertine samples were analyzed at the Center for Earth and Environmental Isotope Research at the University of Texas at El Paso for U-series isotopic compositions. Samples were processed in batches of 12, which included one Basalt Columbia River (BCR-2) standard reference material and 11 travertine samples. For each sample, 100-200 mg powders were weighed into 15 mL centrifuge tubes, then dissolved using 6 mL of 1 N acetic acid (pure) and 15 mg of sodium

citrate to prevent possible adsorption of U and Th during dissolution. If the majority of the sample had not fully dissolved then 3 mL of additional 1 N acetic acid was added. Samples were then allowed to settle for 10 minutes. While samples settled, $^{233}\text{U}/^{229}\text{Th}$ spike was added into 30 mL Teflon® beakers to determine U and Th concentrations using the isotope dilution method. Samples were then transferred into the spiked 30 mL Teflon® beakers. Samples were then emptied into the beakers and were then placed on a hot plate at 100 °C. Acid digestion was carried out by adding 1 mL of concentrated HNO_3 and 3 mL of HF to completely dissolve materials. Sample beakers were placed on the hot plate for one day to digest and then beaker caps were removed to dry the samples. Once dry, 1 mL of concentrated H_3BO_3 solution, 2 mL of 6 N HCl, and 3 mL of Millipore ultrapure water (18.2M Ω) were added to each beaker, to dissolve possible fluoride precipitants created during previous digestion step, and allowed to digest for 4-8 hours or until beakers were no longer had solid material. Once completely clear and free of particles, sample solutions were dried at 90 °C, re-dissolved in 1 mL of 7.5 N HNO_3 , place into 1.5 mL vials that were centrifuged for 5 minutes at 4500 rpm before column chemistry procedures.

Samples were separated and purified for U and Th using ion chromatography procedures similar to Chabaux et al., (1995). Samples, which were previously dissolved in 1 mL of 7.5N HNO_3 , were loaded into columns containing AG 1-X8 anion exchange resin (200-400 mesh). Different concentrations of HNO_3 , HCL, and HCL + Acetone Optima were used as eluents to separate, collect, and purify U and Th in the samples. After column chemistry, U and Th isotopic ratios ($^{234}\text{U}/^{238}\text{U}$, $^{233}\text{U}/^{238}\text{U}$, $^{235}\text{U}/^{238}\text{U}$, $^{230}\text{Th}/^{232}\text{Th}$, and $^{229}\text{Th}/^{232}\text{Th}$) were measured using a Nu Plasma multi-collector inductively coupled plasma mass spectrometer (MC-ICP-MS). A NBL U145B solution and a $^{229-230-232}\text{Th}$ in-house solution were used as the bracketing standards to correct for mass fractionation and ion counter gains for U and Th isotope measurements,

respectively. U and Th concentrations were calculated using measured $^{233}\text{U}/^{238}\text{U}$ and $^{229}\text{Th}/^{232}\text{Th}$ isotope ratios by the isotope dilution method, respectively. Activity ratios for ($^{234}\text{U}/^{238}\text{U}$) and ($^{230}\text{Th}/^{232}\text{Th}$) were calculated from measured $^{234}\text{U}/^{238}\text{U}$ and $^{230}\text{Th}/^{232}\text{Th}$ isotope ratios, respectively.

The accuracy of U and Th concentrations were assessed relative to the measured BCR2 standard reference material. The average measured ($^{234}\text{U}/^{238}\text{U}$)_a and U concentrations for BCR2 were ($^{234}\text{U}/^{238}\text{U}$)_a = 1.005 ± 0.001 and U = 1.669 ± 0.008 ppm (n = 9; 2σ). The results are consistent with the reference values of ($^{234}\text{U}/^{238}\text{U}$)_a = 1.004 ± 0.004 and U = 1.683 ± 0.0017 ppm (Sims et al., 2008; Jochum et al., 2015). The average measured ($^{230}\text{Th}/^{232}\text{Th}$)_a and Th concentrations for BCR2 were ($^{230}\text{Th}/^{232}\text{Th}$)_a = 0.877 ± 0.001 and Th = 5.818 ± 0.002 ppm (n = 12; 2σ). The results are in agreement with the reference values of ($^{230}\text{Th}/^{232}\text{Th}$)_a = 0.877 ± 0.003 and Th = 5.828 ± 0.05 ppm (Sims et al., 2008; Jochum et al., 2016). Age calculations were determined using ISOPLOT 3.75 (Ludwig, 2012) and was also manually checked using a graphical solution of the $^{230}\text{Th}/^{234}\text{U}$ dating equation: plot of ($^{234}\text{U}/^{238}\text{U}$)_a vs ($^{230}\text{Th}/^{234}\text{U}$)_a for closed systems of varying initial ($^{234}\text{U}/^{238}\text{U}$) (Ivanovich, 1994).

3.4.3 Strontium Isotopes Analysis

Travertine samples for strontium isotope analyses were conducted at the Center for Earth and Environmental Isotope Research at the University of Texas at El Paso. Samples were processed in batches of 16, which included one Basalt Columbia River (BCR-2) standard reference material, one blank, and 14 travertine samples. The travertine digestion procedure for Sr isotope analyses also involves ion chromatography, however, no Sr spike was required as Sr concentrations were not measured in this study. For each sample, 100-200 mg powders were weighed into 15 mL centrifuge tubes, then dissolved using 1 mL of 3.5 N HNO₃, and then placed into 1.5 mL vials that were centrifuged for 5 minutes at 4500 rpm. Dissolved samples were then

loaded into chromatography columns, filled with Eichrom® Sr-resin, to separate and purify for Sr following similar procedures by Konter and Storm (2014). The columns were eluted in a series of steps by adding different amounts of 3.5 N HNO₃. Sr was then collected in clean 15 mL Teflon® beakers by adding 0.05 N HNO₃ to the columns. Isotopic ratios of ⁸⁷Sr/⁸⁶Sr were measured using a Nu Plasma MC-ICP-MS using the standard sample bracketing method with the strontium standard NIST SRM 987. The USGS rock standard BCR-2 was measured to assess accuracy of our measurements. The measured ⁸⁷Sr/⁸⁶Sr isotope ratios for BCR2 were $^{87}\text{Sr}/^{86}\text{Sr} = 0.70503 \pm 0.00001$ (n = 10; 2σ). Our results are consistent with the accepted reference values of ⁸⁷Sr/⁸⁶Sr ratio of BCR-2 is 0.70502 ± 0.00001 (2σ) (Jweda et al., 2015).

3.4.4 Carbon and Oxygen Isotopes Analysis

Carbon and oxygen isotope ($\delta^{13}\text{C}$ and $\delta^{18}\text{O}$) analyses were conducted at the University of Kansas' KECK-NSF Paleoenvironmental and Environmental Laboratory. Approximately 100 ug of sample was weighed into a stainless steel boat using a Mettler Toledo microbalance. Stainless steel boats were placed in a brass convoy and samples were vacuum-roasted at 200 °C for 1 hour to remove volatiles. Samples were analyzed and sample CO₂ generated by reaction with 3 drops of 105% H₃PO₄ at 70 °C for 540 seconds using a Thermo Scientific Kiel IV Carbonate Device interfaced to the inlet of a ThermoFinnigan MAT 253 dual inlet mass spectrometer. Carbonate $\delta^{13}\text{C}$ and $\delta^{18}\text{O}$ isotope data are reported relative to VPDB. $\delta^{18}\text{O}$ isotope data were converted to VSMOW for data comparison and discussion. Precision was monitored through the daily analysis of NBS-18 and NBS-19 and is better than 0.10‰ for both $\delta^{13}\text{C}$ and $\delta^{18}\text{O}$.

3.5 RESULTS

3.5.1 U-series Isotope Ratios and Ages

Analyzed travertine samples have ^{238}U concentrations of 0.44 ppm to 30.85 ppm, ^{232}Th concentrations of 0.001 ppm to 0.956 ppm, $(^{234}\text{U}/^{238}\text{U})_{\text{measured}}$ activity ratios of 1.13 ppm to 5.30, $(^{230}\text{Th}/^{238}\text{U})$ of 0.06 to 4.29, and $(^{232}\text{Th}/^{238}\text{U})_{\text{measured}}$ less than 0.20. The low $(^{232}\text{Th}/^{238}\text{U})_{\text{measured}}$ values justify the date determination of travertine samples without detrital Th corrections (Table 2). U-series ages of travertine samples collected from the Lucero Uplift were acquired using Isoplot 3.75 (Ludwig, 2012) and range from 0.94 ± 0.01 ka to 592 ± 110 ka (2σ errors; Table 2; Figure 4A). Ages for six sub-samples (TPL10-Middle, TPL10-Top, TPL23-T, TPL23-M, TPL23-B, and TPL26-T) could not be determined due to samples being older than the upper limit of U-series dating ($> \sim 600$ ka) and/or containing too much detrital ^{232}Th . Three additional data points were considered inaccurate due to relatively high $(^{232}\text{Th}/^{238}\text{U})_{\text{measured}}$ values greater than 0.2 (resulted in abnormally low $(^{234}\text{U}/^{238}\text{U})_i$ compared to the rest of the data) and are not presented here.

For purposes of discussion, travertine ages are binned into three groups referred to as Qtr1, Qtr2, and Qtr3. The three bins were determined using Jenks Natural Breaks classification classes, which identifies class breaks based on identifying best group similar values and that maximize the differences between classes. Samples that fall within Qtr1 range in age from 0.94 ± 0.01 to 84.6 ± 1.3 ka, samples in Qtr2 range from 137.9 ± 2.7 to 355 ± 18 ka, and samples in Qtr3 range from 420 ± 28 to 592 ± 110 ka (Figure 4A). These breaks imply that travertine formation in the study area occurred in three main intervals. Additionally, U-series ages in our study area show a rough correlation but not completely in agreement with mapped stratigraphic position, which is based on elevation of the sample location (e.g. low elevation travertines tend to have younger ages).

The U-series dated travertine samples have high $(^{234}\text{U}/^{238}\text{U})_i$ initial ratios ranging from 3.6 ± 0.02 to 9.4 ± 0.68 . The oldest travertine samples dated (group Qtr3) tend to have the highest $(^{234}\text{U}/^{238}\text{U})_i$ values. The $(^{234}\text{U}/^{238}\text{U})_i$ values show a general decreasing trend with decreasing travertine ages. In our study, variability in travertine ages and $(^{234}\text{U}/^{238}\text{U})_i$ appears to have no correlation with glacial cycles. There is no apparent relationship between travertine ages and their spatial location. Instead, travertine ages are mainly attributed to elevation. Similarly, there is no clear relationship between sample location (i.e. away or near faults) and $(^{234}\text{U}/^{238}\text{U})_i$ initial ratios.

3.5.2 Strontium Isotopes

$(^{87}\text{Sr}/^{86}\text{Sr})$ isotope ratios in all travertine samples range from 0.714 to 0.717 (Table 3; Figure 5). Strontium isotope ratios are fairly consistent across the three age groups, with no major correlation between $^{87}\text{Sr}/^{86}\text{Sr}$ ratios and travertine ages (i.e. Qtr1, Qtr2, and Qtr3). There is, however, a slight increase to more radiogenic values in travertine samples that formed < 20 ka during the current interglacial period while the lowest values occur ~ 90 ka. Similar to U-series data, $^{87}\text{Sr}/^{86}\text{Sr}$ ratios have no spatial relationships with sample location.

3.5.3 Carbon and Oxygen Isotopes

Values for $\delta^{13}\text{C}$ in dated travertine samples range from 2.51 ± 0.00 ‰ to 8.28 ± 0.01 ‰ (VPDB) while $\delta^{18}\text{O}$ values range from 20.84 ± 0.02 ‰ to 25.91 ± 0.02 ‰ (VSMOW; Table 3; Figure 6). Values for $\delta^{13}\text{C}$ are variable across glacial cycles and show three prominent positive peaks of $\delta^{13}\text{C}$ values at 351 ka, 195 ka, and 6 ka as well as a sharp excursion to a lower value at 65 ka. Values for $\delta^{18}\text{O}$ are also variable across glacial cycles (Figure 6) but contain less prominent peaks: positive peaks of $\delta^{18}\text{O}$ values at 432 ka and 195 ka; negative peaks at 424 ka, 305 ka, 65 ka, 12 ka, and 4 ka. Additionally, data from Williams et al., (2017) and Kampman et al., (2012) are used to compare our dataset and test competing models (Figure 6).

3.6 DISCUSSION

Travertine deposits are important records of the complex interplay between tectonics (i.e. seismicity, faults, magmatism, mantle degassing) and climatic changes (glacial-interglacial cycles; water availability) through time in terrestrial settings (Crossey et al., 2011; Williams et al., 2013; Priewisch et al., 2014; Ricketts et al., 2019). The relationship of travertine formation to tectonic and/or climatic influences is mainly based on the hypothesis that travertine systems are either CO₂ or water limited (Crossey et al., 2011; Ricketts et al., 2019). If travertine formation is limited by available CO₂, then a tectonic model in which increase of CO₂ flux is episodic due to either seismicity, magmatism/volcanism, and/or mantle degassing, would be a reasonable approach to interpret travertine records (Williams et al., 2013; Williams et al., 2015). Alternatively, if CO₂ flux is considered constant with time from deep crustal or mantle degassing, formation of travertine formation may be controlled by water availability to transport Ca and bicarbonate ions for travertine formation. For example, in regions where glacial periods correspond to cooler and wetter conditions, travertine formation rates would increase due to the increased availability surface recharge, leading to a water-controlled system. In regions where interglacial periods correspond to generally warmer and dryer conditions, water-controlled systems would produce less travertine (Tafoya, 2012; Priewisch et al., 2014; Ricketts et al., 2019). This study attempts to evaluate these competing models for episodic travertine formation along the Santa Fe fault in New Mexico, USA, a region that features both tectonic activity and climate changes.

3.6.1 Travertine Age Distribution and Formation Rates

Many previous studies have determined that travertine formation in the Rio Grande rift is episodic at 100 ky time scales (e.g. Goff and Shevenall, 1987; Formento-Trigilio and Pazzaglia, 1998; Embid, 2009; Cron, 2011; Crossey et al., 2011; Tafoya, 2012; Kolomaznik et al., 2013;

Priewisch et al., 2014; Ricketts et al., 2014). These episodes of travertine formation are attributed to variable paleohydrologic conditions influenced by changes of climate and/or tectonics (e.g. Ricketts et al., 2014). Many studies argue that paleoclimate may be the main influence of travertine formation but tectonic controls are also commonly proposed (e.g. Brogi et al., 2010; Pigati et al., 2011; Kampman et al., 2012).

Based on our age kernel density estimations (Figure 4A), no clear correlation between travertine ages in our study area and glacial and interglacial periods can be observed to infer for the paleoclimate model as the main influence of travertine formation at the Lucero Uplift, similar to the observations in Priewisch et al. (2014). Qtr2 and Qtr3 travertines (100-600 ka) formed during both glacial and interglacial periods while the Qtr1 travertines (0-100 ka) primarily formed during interglacial periods. In the Qtr1 group (0-100 ka), the biggest peak occurs within the current interglacial period. The occurrence of the biggest peak in the youngest group may be due to a sampling bias associated with decreased preservation potential for travertine deposits with increasing age and not with gradual increase in travertine formation over time (Ricketts et al., 2019). Additionally, in this study, certain samples were not dated due to the fact that they might have been too old (>600 ka) for U-series dating, based on their high stratigraphic position. In this way we might artificially create a sampling bias toward young and recent samples.

Similarly, we observe no correlation with climate cycles in other travertine studies in the Rio Grande rift and Jemez Lineament (Figure 4C). In comparison, a compilation of travertine ages from the rest of North American (i.e. minus travertines associated with the Rio Grande rift and Jemez Lineament; Figure 4D) suggests that they may be influenced and/or correlated with climatic cycles. For example, large peaks in travertine ages from North America (Figure 4D) occur during glacial to interglacial transitions, a conclusion that Ricketts et al. (2019) made. Such comparison

highlights the possible link of travertine formation to the activity of the Rio Grande rift and Jemez Lineament, i.e., as a possible tectonic model.

In addition to general age distributions from these travertine samples, growth rates in individual samples were calculated using regressions of the ages and distance of multiple dated sample layers along their direction of growth. Travertine growth rates were determined in this study for 14 individual samples that had multiple available growth layers for dating and varied from 0.06 mm/kyr to 53 mm/kyr (Figure 4B). Interestingly, previous studies in central New Mexico and eastern Arizona estimated travertine formation rates that are generally orders of magnitude higher, ranging from ~0.1 m/kyr to 1 m/kyr (Embid, 2009; Priewisch et al., 2014). Several studies at other locations estimate, modern travertine formation rates at 1 m/kyr to 1,000 m/kyr but those rates are most likely overestimated due to the short time scales of observations as compared to long time scales in the field studies (Pentecost, 2005). Furthermore, the observed difference in travertine formation rates between this study and the previous field studies is attributed to the spatial scale at which these rates were inferred from. For example Embid (2009) and Priewisch et al. (2014), the authors dated travertine layers collected from the bottom and top of thick travertine deposits in the field, with thicknesses generally varying from 8 to 22 m. Calculating rates using this method assumes that travertine deposition was constant from the bottom to the top of the deposit through time. However, travertine deposition rate is often not constant, a situation commonly observed in our samples, nor do layers systematically young upwards. In some of our samples, younger mm-scale veins can be seen cutting into older travertine layers. This is confirmed by the vastly different U-series ages in layers located only mm away from other dated layers in the same travertine sample (Table 2). In other cases, crosscutting relationships are not easily observed visually but are apparent when middle layers are much

younger than the surrounding layers, based on our dated U-series ages, indicating a later growth event along a pre-existing fracture. Based on observations made in our mm-scale analyses, and those made by Ricketts et al. (2014), we can infer that many of the thick (> 1 m) travertine deposits are likely crosscut by multiple younger travertine layers that can lead to an overestimation of the deposition rates. Hence, based on our results, we argue that the most reliable travertine rates are most likely from dating multiple growth layers at a hand sample scale, not from thick exposures in the field.

The travertine formation rates determined in our study appear to have no correlation with climate cycles (Figure 4B). However, an argument can be made that the highest formation rates occur within the youngest travertine group (Qtr1) possibly due to increased availability of meteoric water in the subsurface when there was high hydrologic head (Priewisch et al., 2014). Such a correlation is not observed in the older travertine groups in this study.

Hence, based on our detailed travertine study with high-resolution age distributions in the Lucero Uplift, we conclude that travertine formation is not dependent on climatic influences. This leads us to explore the possibility of tectonic activity as the primary control in the formation of travertine deposits, where faults and associated seismicity control the movement of CO₂ (magmatically or mantle derived) towards the surface. The age distribution and precipitation rates of our travertine samples, across climate cycles, lead us to infer that travertine deposits of within our study region are more dependent on factors other than climate.

3.6.2 Tectonic Implications: structural observations and age constraints

In New Mexico, travertine precipitating springs and travertine deposits are commonly associated with major fault networks and/or with magmatism (Figure 1 and 2). Of great importance in our study area is the Santa Fe fault, a ~60° east dipping normal fault, which trends N-S along

the entire length of our study area and is estimated to have accumulated more than 3,060 m of throw (Russell and Snelson, 1994; Ricketts and Karlstrom, 2014). The Santa Fe fault has been active since the Oligocene, with the main phase of extension occurring during the middle Miocene (~16 Ma; Chapin and Cather, 1994). A recent field study of extensional calcite filled veins in travertine quarries, preserved several km south of our study area (Mesa Aparejo), suggested that extension related to continued movement along the Santa Fe fault system has continued from ~2 Ma to at least ~250 ka (Ricketts et al., 2014).

The latest stage of extension of the Santa Fe fault overlaps with our data. In the southern section of our study area (Figure 2), travertine samples were collected from the base of a large travertine deposit overlying tilted Santa Fe Group deposits. These samples consist of travertine veins cutting into a transition zone (i.e. unlayered travertine units with varying detrital material) between the tilted Santa Fe Group and overlying horizontal travertine deposits, a layered horizontal travertine layer above the transition zone material, and two samples from the top of the thick travertine deposit (Figure 2E). Additionally, two samples were collected at the base of this same angular unconformity and the top of a thick travertine deposit in the central portion of our study area (near image in Figure 2C). The U-series age in the transition zone sample in the south is 592 ± 110 ka, travertine ages in the layered bases overlying the transition zone (from both the south and central portion of the study) range from 309 ± 13 ka to 351 ± 19 ka, while ages in the top portions range from 424 ± 1.4 ka to 490 ± 52 ka in the south and 355 ± 18 ka to 466 ± 39 ka in the central region. Based on the transition zone sample age, it is clear that this portion of the Santa Fe fault has not slipped within the 490 ± 52 to 592 ± 110 ka (2σ). It is also likely that travertine formation continued immediately after the last seismic event further constraining fault movement to ~490 ka. Furthermore, we found no field evidence of travertine deformation (i.e. no folding, no

offset, and no faulting in travertine deposits) within our study area, where large travertine deposits conceal numerous underlying faults that may have acted as potential conduits for CO₂-rich fluids.

3.6.3 Paleo-fluid Sources and evolution history inferred from the travertine geochemical record of $\delta^{13}\text{C}$ and $\delta^{18}\text{O}$

Faults that extend to deep depths in the crust are capable of transporting epigenic fluids derived from surface recharge and endogenic fluids that carry very high mineral loads and high levels of exotic gases from deep within the Earth (Crossey et al., 2011). The geochemical signatures of these paleo-fluids can be preserved in travertine deposits and provide a window into paleo subsurface origins and pathways for both epigenic and endogenic fluids.

For travertine deposits in our study area, their $\delta^{13}\text{C}$ and $\delta^{18}\text{O}$ values vary systematically through time and are highly correlated, indicating that both isotope systems are modified by similar physical processes (Figure 6 & 7). There is no temporal trend in $\delta^{13}\text{C}$ and $\delta^{18}\text{O}$ compositions associated with climate cycles nor with isotopic values from other studies near our study area (Figure 6). Additionally, we were not able to correlate high $\delta^{13}\text{C}$ compositions with seismic events. Four major increases in high $\delta^{13}\text{C}$ compositions at ~20 ka, 70 ka, 190 ka, and 350 ka are followed by suppressions in $\delta^{13}\text{C}$ and $\delta^{18}\text{O}$ (Figure 6). The sharp depressions in $\delta^{13}\text{C}$ and $\delta^{18}\text{O}$ compositions likely correspond to periods marked by an increase in unfractionated CO₂ to the fluid system or, more likely, decrease in CO₂ input into the shallow fluid system from deeper crustal reservoirs (Kampman et al., 2012).

The $\delta^{13}\text{C}$ values from this study are highly positive (2 ‰ to 9 ‰; VPDB; Figure 6), compared to low temperature carbonates such as marine carbonates or soil carbonates, suggesting endogenically sourced carbon (likely high temperature water-rock reactions) that has experienced extensive fractionation due to rapid degassing of CO₂ (Rayleigh fractionation) during seismic

events or travertine precipitation (Pentecost, 2005; Williams et al., 2015; Williams et al., 2018). $\delta^{18}\text{O}$ compositions generally reflect the fluid source (i.e. meteoric vs. deep fluids or mixing of both) but in these travertines, Rayleigh fractionation of $\delta^{18}\text{O}$ values is also driven by the degassing of CO_2 and precipitation of travertine resulting in isotopically heavier $\delta^{18}\text{O}$ compositions in fluids, as recorded in travertines precipitated in later stages (Figure 6).

In Equation 2, the degassing of CO_2 from HCO_3^- and Ca^{2+} saturated fluids is reflected in the evolving $\delta^{13}\text{C}$ and $\delta^{18}\text{O}$ compositions of precipitated travertines. Due to the preferential loss of ^{12}C and ^{16}O during degassing, the fluid and future precipitated travertine should inherit increasingly enriched $\delta^{13}\text{C}$ and $\delta^{18}\text{O}$ compositions with time. That trend is not easily observed in our data within the three travertine groups (i.e. Qtr1, Qtr2, and Qtr3; Figure 7). However, there is a slight enrichment of $\delta^{13}\text{C}$ compositions from older travertine (i.e. Qtr3) to younger travertine (i.e. Qtr1) groups. In general, individual travertine groups do not show progressive enrichment in $\delta^{13}\text{C}$ nor $\delta^{18}\text{O}$ compositions with time. Nonetheless, the high $\delta^{13}\text{C}$ (2‰ to 9‰) and $\delta^{18}\text{O}$ (21‰ to 26‰) compositions lead us to infer a magmatic/mantle source.

Magmatic/mantle fluids have $\delta^{13}\text{C}$ values of approximately -6‰ but kinetic isotope modeling indicates that carbonates precipitated during CO_2 degassing may be enriched by as much as 10‰ in $\delta^{13}\text{C}$ values above equilibrium values, as is documented in our travertines and those of other studies (Pentecost, 2005; Crossey et al., 2009; Tafoya, 2011; Williams et al., 2017). This information, coupled with the highly positive $\delta^{13}\text{C}$ compositions in our travertine samples, lead us to infer CO_2 is derived from magmatic/mantle sources.

Magmatic/mantle sources of travertine precipitating fluids is further supported by accompanying high $^3\text{He}/^4\text{He}$ (CO_2 is inferred as the main carrier gas for He), which is widely accepted as a tracer of primordial ^3He from the mantle (Ballentine et al., 2001; Newell et al., 2005;

Crossey et al., 2011). Similar conclusions (i.e. likely influence of magmatic/mantle fluids) have been reached by analyses of travertine deposits, travertine depositing springs, and fault related calcite veins along the Rio Grande rift margins and Jemez Lineament, where low velocity zones and regional Quaternary volcanism are prominent (Embid, 2009; Tafoya, 2011; Crossey et al., 2011; Williams et al., 2013; Williams et al., 2018; Blomgren et al., 2019).

3.6.4 Paleo-fluid Sources inferred from the travertine geochemical record of Sr and U isotopes

Sr isotope data provide useful information on the source of fluids in fault zones, because they do not fractionate and typically reflect the lithologies from which fluids pass through. In our study, travertine deposits have $^{87}\text{Sr}/^{86}\text{Sr}$ values ranging from 0.714 to 0.717 (Figure 5), similar to the wide range of $^{87}\text{Sr}/^{86}\text{Sr}$ values of travertines and travertine-precipitating springs (0.711-0.734) documented in other studies near our study area (Goff et al., 1983; Crossey, 2006; Williams et al., 2013). The $^{87}\text{Sr}/^{86}\text{Sr}$ values in natural water, and in different rock lithologies in the Rio Grande rift vary greatly. Head waters of the Rio Grande river have $^{87}\text{Sr}/^{86}\text{Sr}$ values of ~ 0.709 (Hogan et al., 2007), very similar to $^{87}\text{Sr}/^{86}\text{Sr}$ values of ~ 0.709 at Elephant Butte Reservoir (Garcia, 2016). Basalts in the Rio Grande rift and Jemez Lineament typically have $^{87}\text{Sr}/^{86}\text{Sr}$ values of 0.703-0.708 (Allen and Foord, 1991; Thompson et al., 1991; McMillan et al., 2000), Mesozoic carbonates range from 0.706-0.709 (Kirkland et al., 1995), Paleozoic carbonates vary from 0.706-0.711 (Mukhopadhyay and Brookins, 1976; Burke et al., 1982; McArthur et al., 2001; Van der Hoven and Quade 2002; Young and Chan, 2017; Williams et al., 2018), and Proterozoic basement has the most radiogenic values at 0.735-0.748 (Taggart and Brookins, 1975; Goff and Gardner, 1994; Crossey et al., 2006).

$^{87}\text{Sr}/^{86}\text{Sr}$ values of travertines in this study are significantly radiogenic (0.714 to 0.717) and incompatible with previous hydrologic models, where the majority of the fluids are believed to originate from surface recharge in the Lucero Uplift with unradiogenic $^{87}\text{Sr}/^{86}\text{Sr}$ ratios (Goff et al., 1983). Instead, these highly radiogenic values are compatible with hydrologic models where mixing of meteoric and deep fluids occurs along deep faults (Williams et al., 2013).

The relatively high $^{87}\text{Sr}/^{86}\text{Sr}$ values of travertine samples in our study (0.714 to 0.717) suggest fluid-rock interaction during deep crustal circulation in more radiogenic granitic basement (~0.740). We infer that deeply sourced fluids initially acquire the signature of the highly radiogenic basement materials, ascend along deep basement penetrating faults mixing with Paleozoic carbonates (0.706-0.711), and further mixing with shallow meteoric fluids (~0.709) near the surface to reach their current $^{87}\text{Sr}/^{86}\text{Sr}$ isotopic values. Fluid mixing calculations (Crossey et al., 2006; Williams et al., 2018) suggest that travertine, travertine-precipitating springs, and fault-precipitated calcites with $^{87}\text{Sr}/^{86}\text{Sr}$ values of ~0.715 are attainable with mixing of approximately 1-20% of highly radiogenic fluids with low non-radiogenic shallow meteoric fluids.

Similarly, the $(^{234}\text{U}/^{238}\text{U})_i$ values from travertine in our study range from 3.57 to 9.29 (Figure 4A), which is consistent with the hypothesis that deeply derived fluids mix with shallow meteoric fluids. Generally, fluids that originate from deep sources can be distinguished from shallow sources due to their higher $(^{234}\text{U}/^{238}\text{U})_i$ values (Kronfeld, 1975; Kronfeld et al., 1994; Chabaux et al., 2003). River waters typically have $(^{234}\text{U}/^{238}\text{U})_i$ values ranging from 1.0-2.6 (Chabaux et al., 2003). In the Rio Grande, $(^{234}\text{U}/^{238}\text{U})_i$ values in river water range from 1.18 to 2.31 (Nyachoti, 2016), much lower than $(^{234}\text{U}/^{238}\text{U})_i$ values in our travertine deposits. Of particular interest are the older travertine deposits in our study, which have the highest $(^{234}\text{U}/^{238}\text{U})_i$ values with an average initial ratio of 6.22 (range 4.23-9.29) compared to the youngest travertine group

with an average initial ratio of 4.51 (range 3.57-5.41). The high ($^{234}\text{U}/^{238}\text{U}$)_i ratio in these fluids likely indicates fluids were derived from basement rocks. Basaltic magmas are typically depleted in U, which means magmatic fluids would likely have a limited effect on fluid ($^{234}\text{U}/^{238}\text{U}$)_i values (Williams et al., 2018). Alternatively, Paleozoic carbonates and shallow fluids have slightly higher U concentrations but lower ($^{234}\text{U}/^{238}\text{U}$) ratios that would still not explain the values observed in our travertine samples. We infer the higher ($^{234}\text{U}/^{238}\text{U}$)_i values in older travertine as recording the last episode of seismicity, which allowed these highly radiogenic fluids to reach the surface. This is supported by evidence constraining the last seismic event > 350 ka. Over time, deep fluids transported along the Santa Fe fault continued and mixed with shallow and less radiogenic fluids, which has resulted in a decreasing trend with average ($^{234}\text{U}/^{238}\text{U}$)_i values of 4.78.

3.6.5 Sr and U isotope and concentration mixing

Variations in geochemical data can be distinguished by using a mixing plot of two endmember compositions (Vollmer, 1976). In our case, the data being modeled are $^{87}\text{Sr}/^{86}\text{Sr}$ vs $^{234}\text{U}/^{238}\text{U}$ isotopic ratios, and their respective elemental ratios, of two commonly found endmembers (i.e. Sandia Granite and shallow aquifers of the Rio Grande). Mixtures of two endmembers follow hyperbolic trends with curvatures that depend on relative elemental concentrations (Langmuir, 1977). Mixing of two components with different Sr and U isotopic compositions and concentrations will result in a hyperbola in the form of:

$$\text{Eq. 3 } Ax + Bxy + Cy + D = 0$$

where

$$A = a_2b_1Y_2 - a_1b_2Y_1$$

$$B = a_1b_1 - a_2b_1$$

$$C = a_2b_1X_1 - a_1b_2X_2$$

$$D = a_1b_2X_2Y_1 - a_2b_1X_1Y_2$$

and x is $^{234}\text{U}/^{238}\text{U}$ isotopic ratio, y is the $^{87}\text{Sr}/^{86}\text{Sr}$ isotopic ratio, a is the $[\text{Sr}]$, and b is the $[\text{U}]$ in the two endmembers (subscript 1 refers to endmember #1 and subscript 2 refers to endmember #2). The mixing curve is defined by the concentration ratio of $c = (\text{Sr}/\text{U})_1/(\text{Sr}/\text{U})_2$ of Sohn et al. (2015), which is derived from $c = (\text{Sr}_1 \times \text{U}_2)/(\text{Sr}_2 \times \text{U}_1)$ of Vollmer et al. (1976), the latter which is used in this study.

The two endmembers, Sandia Granite and Rio Grande, have a concentration ratio of 25 ($c = (\text{Sr}_1 \times \text{U}_2)/(\text{Sr}_2 \times \text{U}_1)$) and would have a mixing curve (dashed red line) as shown on Figure 8. Only two samples lie with range of the direct mixing curve of these two endmembers. In contrast, the majority of the travertine samples, from the three separate groups, plot along a single horizontal line (Figure 8). This straight line implies a scenario where a small percentage of highly radiogenic endogenic fluids mixes with a larger volumetric less radiogenic epigenic fluid. However, we must consider the possibility of an endmember that is isotopically more radiogenic than our Rio Grande endmember #2.

For example, Vuataz et al. (1988) analyzed core samples from Valles Caldera where altered limestones were found to have $^{87}\text{Sr}/^{86}\text{Sr}$ ratios ranging from 0.715 to 0.720. It is possible that in our study area the shallow limestone aquifers (not well constrained) have slightly higher isotopic signatures compared to basinal meteoric fluids. Additionally, it is unlikely that these deep fluids (located along the western margin of the rift; Figure 2) mix with shallow meteoric fluids similar to those of the Rio Grande (located 35 km east of study area).

3.6.6 Regional Implications

Travertine deposits represent paleo fluid flow; thus they record information pertaining to changes in tectonic, magmatic, or climatic changes through time. Previous studies have proposed correlations between travertine formation and climate cycles (Pigati et al., 2011; Kampman et al.,

2012; Ricketts et al., 2019). Others studies (e.g. Ozkul et al., 2013; Brogi et al., 2016; Giustini et al., 2018; Miocic et al., 2019) attribute travertine formation to tectonic activity due to the formation of travertine deposits through multiple glacial cycles. However, multiple studies attribute travertine formation to both tectonic, climatic, and in some cases magmatic origins (Faccenna et al., 2008; Brogi et al., 2010; DeFilippis et al., 2013; Priewisch et al., 2014). In our view, the simplest explanation for travertine formation in our study area mainly involves tectonic controls (i.e. deep penetrating faults) and localized magmatic/mantle degassing.

Travertine precipitating springs and travertine deposits in our study area and region are intimately associated with major fault systems (Figure 1). Additionally, there appears to be a spatial relationship with travertine deposits and volcanism associated with the Jemez Lineament, in particular along the western margin of the Rio Grande rift (Figure 1). This close association with deep fault systems, volcanism, and clear indication that paleo-fluids are derived from endogenic sources (based on geochemistry results of this study) demonstrates the involvement of tectonic and magmatic controls on travertine formation in the Rio Grande rift.

Furthermore, our study area, and those of other travertine studies along the western margin of the rift, are underlain by a prominent low mantle velocity zone believed to be associated with the Jemez Lineament (Figure 9; e.g. Schmandt and Humphreys, 2010; Sosa et al., 2014). The Socorro magma body and Valles Caldera are also underlain by this zone. This low velocity zone is the likely source of mantle derived mantle ^3He and CO_2 (the latter which is critical for the formation of travertine; see Eq. 1 and 2) identified by previous studies in active travertine-precipitating springs (green boxes on Figure 9; Newell et al., 2005; Williams et al., 2013). However, climatic controls cannot fully be dismissed due to their effects on paleo-hydrologic conditions. Nonetheless, based on our study and other travertine studies in the region, we attribute

travertine formation to tectonic (Rio Grande rift faults) and mantle/magmatic (low velocity zone of Jemez Lineament) controls based on observed close associations with fault zones, low velocity mantle zones, active magmatism, mantle CO₂ flux, accompanying high ³He/⁴He, ⁸⁷Sr/⁸⁶Sr, and (²³⁴U/²³⁸U); (Figure 9).

A conceptual model, based on work by Williams et al. (2013) and Priewisch et al. (2014), for travertine formation (along cross-section line B-B' on Figure 9) is shown on Figure 10. In this model, we show a cross-section by Sosa et al. (2014) that begins in the Colorado Plateau, crosses near our study area, passes through the Socorro magma body and Rio Grande rift, and ends just past the eastern margin of the Rio Grande rift in Texas. In this model, the low velocity zone beneath the Jemez Lineament, which Sosa et al. (2014) termed the Jemez Upwelling, can be clearly seen and is the likely source for the volcanic centers of the Jemez Lineament and mantle derived gases (i.e. ³He and CO₂). In the center model of Figure 10, we hypothesize the ascent of mantle derived gases through the crust where they accumulate along volcanic feeders and deep basement penetrating faults of the Rio Grande rift. These faults then act as conduits for the concentration and migration of mantle/magmatic gases and fluids to reach the surface. Along this flow path, endogenic fluids interact with Precambrian crystalline units and pick up high radiogenic isotopic signatures (Figure 10; top right image). These endogenic fluids then continue towards the surface either as a result of local fault related hydrothermal pressure (Uysal et al., 2009), seismicity, and/or pulses in mantle/magmatic activity. Along this trajectory, the endogenic fluids interact with sedimentary units and epigenic fluids, resulting in dilution of the once endogenic fluids (i.e. mixing of fluids with different isotopic compositions). At and near the surface, CO₂ in solution (i.e. HCO₃⁻) begins to degass causing the formation of travertines (see Eq. 1 and 2). The final result (Figure

10; top left image) is the formation of large travertine deposits that contain a record of the isotopic composition of the fluid at the time of formation.

To conclude, the high isotopic (i.e. $^{87}\text{Sr}/^{86}\text{Sr}$ and $(^{234}\text{U}/^{238}\text{U})_i$) signatures of this study reflect deep fluid sources migrating to shallow surfaces along the Santa Fe fault system through time. The difference in variation between $^{87}\text{Sr}/^{86}\text{Sr}$ and $(^{234}\text{U}/^{238}\text{U})_i$ values (i.e. Sr shows little variation while U decreases with time) is due to shallow fluids having higher Sr concentrations, which may dilute the Sr signature of deep fluids. Additionally, the decreasing $(^{234}\text{U}/^{238}\text{U})_i$ signature is a possible indication of the last impulse of highly radiogenic endogenic fluids to reach the surface due to a tectonic and/or magmatic event in the region. For example, on Figure 10, tilted Santa Fe Group units are overlain by an undeformed horizontal travertine deposit that records a minimum constraint on the timing of the last seismic event associated with the Santa Fe fault. It is also possible that Sr and U isotopic trends reflect varying fluid-rock interactions in space and time along the fluid pathways. However, data found in various hydrogeochemical studies in the area support the hypothesis that endogenic fluids mix with epigenic fluids along deeply penetrating faults (Crossey et al., 2011; Williams et al., 2013; Priewisch et al., 2014; Williams et al., 2018).

3.7 CONCLUSIONS

U-series ages of travertine deposits in the Lucero Uplift indicate that formation has been active since at least ~600 ka, though older travertine deposits are inferred based on stratigraphic position. In our study, travertine formation ages were categorized into 3 groups: Qtr1 0.94 ± 0.01 to 84.6 ± 1.3 ka, Qtr2 137.9 ± 2.7 to 355 ± 18 ka, and Qtr3 420 ± 28 to 592 ± 110 ka. The majority of the travertine deposits in our study formed during glacial and interglacial periods. The focus of this study was not of volumes of travertine deposits but of the timing of formation. We find minimal evidence to attribute paleoclimate cycles to travertine formation in the Lucero Uplift. This

is supported by varying travertine precipitation rates (0.08- 53 mm/ka), which show no correlation with climatic cycles. However, an argument can be made to suggest paleoclimate plays a minimal influence on travertine formation due to the need of fluids in the subsurface, which are controlled by paleo-hydrologic conditions.

C, Sr, and U isotope data demonstrate high ratios in travertine deposits of the Lucero Uplift. $\delta^{13}\text{C}$ values range 2 – 9‰, $^{87}\text{Sr}/^{86}\text{Sr}$ values range from 0.714 – 0.717, and $(^{234}\text{U}/^{238}\text{U})_i$ values range from 3.57 – 9.29, suggesting fluid-rock interaction during deep crustal circulation in more radiogenic basement rock. We interpret these data as evidence of major tectonic influence in travertine formation due to spatial associations with faults (i.e. seismicity) and low mantle velocity zones (i.e. Rio Grande rift and Jemez Lineament) responsible for Quaternary basaltic volcanism and regional mantle degassing (Dunbar, 2005; Newell et al., 2005; Embid, 2009; Priewisch et al., 2014; Williams et al., 2018). Furthermore, we constrain movement of the Santa Fe fault between 490 ± 52 to 592 ± 110 ka (2σ) based on undeformed travertine deposits overlying tilted Santa Fe Group units in two sections of our study area. Our data and interpretations suggest that travertine formation is driven by tectonic (Rio Grande rift) and regional mantle/magmatic (Jemez Upwelling) controls. The results presented here confirm that travertine deposits provide important insights into paleo-fluid sources along major fault zones.

3.8 REFERENCES

- Aldrich, M.J., 1986, Tectonics of the Jemez lineament in the Jemez Mountains and Rio Grande rift: *Journal of Geophysical Research*, v. 91, no. B2, p. 1753–1762, doi:10.1029/JB091iB02p01753.
- Allen, M.S., and Foord, E.E., 1991, Geological geochemical and isotopic characteristics of the Lincoln County porphyry belt, N.M.: Implications for regional tectonics and mineral

- deposits: New Mexico Geological Society Fall Field Conference Guidebook, v. 42, p. 97-115.
- Baldrige, W.S., Olsen, K.H., and Callender, J.F., 1984, Rio Grande rift: Problems and Perspectives: New Mexico Geological Society, Guidebook 35, p. 1-12.
- Ballentine, C.J., Schoell, M., Coleman, D., and Cain, B.A., 2001, 300-Myr-old magmatic CO₂ in natural gas reservoirs of the west Texas Permian basin: *Nature*, v. 409, p. 327–331, doi:10.1038/35053046.
- Barker, J.M., Austin, G.S., and Sivills, D.J., 1996, Travertine in New Mexico—Commercial deposits and otherwise: New Mexico Bureau of Mines and Mineral Resources Bulletin, v. 154, p. 73–92.
- Berardi, G., Vignaroli, G., Billi, A., Rossetti, F., Soligo, M., Kele, S., Baykara, M.O., Bernasconi, S.M., Castorina, F., Tecce, F. and Shen, C.C., 2016, Growth of a Pleistocene giant carbonate vein and nearby thermogene travertine deposits at Semproniano, southern Tuscany, Italy: Estimate of CO₂ leakage. *Tectonophysics*, 690, pp.219-239.
- Berglund, H.T., Sheehan, A.F., Murray, M.H., Roy, M., Lowry, A.R., Nerem, R.S., and Blume, F., 2012, Distributed deformation across the Rio Grande Rift, Great Plains, and Colorado Plateau: *Geology*, v. 40, p. 23–26, doi:10.1130/G32418.1.
- Blomgren, V.J., Crossey, L.J., Karlstrom, K.E., Fischer, T.P. and Darrah, T.H., 2019, Hot spring hydrochemistry of the Rio Grande rift in northern New Mexico reveals a distal geochemical connection between Valles Caldera and Ojo Caliente. *Journal of Volcanology and Geothermal Research*, 387, p.106663. doi: 10.1016/j.jvolgeores.2019.106663
- Bourdon, B., Turner, S., Henderson, G. Lundstrom, C., 2003, Introduction to U-series Geochemistry: doi:10.2113/0520001.

- Brogi, A., and Capezzuoli, E., 2009, Travertine deposition and faulting: The fault-related travertine fissure-ridge at Terme S. Giovanni, Rapolano Terme (Italy): *International Journal of Earth Sciences*, v. 98, p. 931–947, doi:10.1007/s00531-007-0290-z.
- Brogi, A., Capezzuoli, E., Aqué, R., Branca, M., and Voltaggio, M., 2010, Studying travertines for neotectonics investigations: Middle–late Pleistocene syn-tectonic travertine deposition at Serre di Rapolano (Northern Apennines, Italy): *International Journal of Earth Sciences*, v. 99, p. 1383–1398, doi:10.1007/s00531-009-0456-y.
- Brogi, A., Alçiçek, M.C., Yalçiner, C.Ç., Capezzuoli, E., Liotta, D., Meccheri, M., Rimondi, V., Ruggieri, G., Gandin, A., Boschi, C. and Büyüksaraç, A., 2016. Hydrothermal fluids circulation and travertine deposition in an active tectonic setting: insights from the Kamara geothermal area (western Anatolia, Turkey). *Tectonophysics*, 680, pp.211-232.
- Bullen, T.D., Krabbenhoft, D.P. & Kendall, C., 1996, Kinetic and mineralogic controls on the evolution of groundwater chemistry and $87\text{Sr}/86\text{Sr}$ in a sandy silicate aquifer, northern Wisconsin, USA: *Geochimica et Cosmochimica Acta*, v. 60, p. 1807-1821.
- Burke, W.H., Denison, R.E., Hetherington, E.A., Koepnick, R.B., Nelson, H.F. and Otto, J.B., 1982. Variation of seawater $87\text{Sr}/86\text{Sr}$ throughout Phanerozoic time. *Geology*, 10(10), pp.516-519.
- Chabaux F., A.S. Cohen, R.K. O’Nions, and J.R. Hein, 1995, 238U - 234U - 230Th chronometry of Fe- Mn crusts. *Geochimica et Cosmochimica Acta* 59, 633–638.
- Chabaux, F., Riotte, J., and Dequincey., O., 2003, U-Th-Ra fractionation during weathering and river transport: *Reviews in Mineralogy and Geochemistry*, v. 52, p. 533–576.
- Channer, M.A., Ricketts, J.W., Zimmerer, M., Heizler, M., and Karlstrom, K.E., 2015, Surface uplift above the Jemez mantle anomaly in the past 4 Ma based on $40\text{Ar}/39\text{Ar}$ dated

- paleoprofiles of the Rio San Jose, New Mexico, USA: *Geosphere*, v. 11, p. 1384–1400, <https://doi.org/10.1130/GES01145.1>.
- Chapin, C.E., 1979, Evolution of the Rio Grande rift—A summary. *Rio Grande rift: tectonics and magmatism*, 14, pp.1-6.
- Chapin, C.E., Cather, S.M. and Keller, G.R., 1994, Tectonic setting of the axial basins of the northern and central Rio Grande rift, in Keller, G. R., S. M. eds, *Rio Grande rift: Structure, stratigraphy, and tectonic setting*, Geological Society of America Special Paper 291, p.5-25
- Chapin, C.E., McIntosh, W.C., Chamberlin, R.M., Mack, G.H. and Giles, K.A., 2004, The late Eocene-Oligocene peak of Cenozoic volcanism in southwestern New Mexico. *The Geology of New Mexico: A Geologic History: New Mexico Geological Society Special Publication*, 11, pp.271-293.
- Cheng, H., Edwards, R.L., Hoff, J., Gallup, C.D., Richards, D.A., Asmerom, Y., 2000, The half-lives of uranium- 234 and thorium-230. *Chem. Geol.* 169, 17-33.
- Clark, K.I., Fritz P., 1997, *Environmental Isotopes in Hydrogeology*: Lewis Publishers, New York, pp. 328.
- Cron, B., 2011, *Geochemical characteristics and microbial diversity of CO₂-rich mound springs of the Tierra Amarilla anticline, New Mexico [M.S. thesis]*: Albuquerque, University of New Mexico, 110 p.
- Crossey, L.J., Fischer, T.P., Patchett, P.J., Karlstrom, K.E., Hilton, D.R., Huntoon, P., and Reynolds, A.C., 2006, Dissected hydrologic system at Grand Canyon: Interaction between upper world and lower world waters in modern springs and travertine: *Geology*, v. 34, p. 25-28.

- Crossey, L.J., Karlstrom, K.E., Springer, A., Newell, D., Hilton, D., and Fischer, T., 2009, Degassing of mantle-derived CO₂ and ³He from springs in the southern Colorado Plateau region— neotectonic connections and implications for groundwater systems: *Geological Society of America Bulletin*, v. 121, p. 1034-1053. DOI 10.1130/B26394.
- Crossey, L.J., Karlstrom, K.E., Newell, D.N., Kooser, A., and Tafoya, A., 2011, The La Madera travertines, Rio Ojo Caliente, northern New Mexico: Investigating the linked system of CO₂-rich springs and travertines as neotectonic and paleoclimate indicators, in Koning, D.J., et al., eds., *Geology of the Tusas Mountains and Ojo Caliente: New Mexico Geological Society Guide- book*, v. 62, p. 301–316.
- Crossey, L.J., Karlstrom, K.E., Dorsey, R., Pearce, J.L., Wan, E., Beard, L.S., Asmeron, Y., Polyak, V., Crow, R., Cohen, A., and Bright, J., 2015, The importance of groundwater in propagating downward integration of the 6–5 Ma Colorado River system—Geochemistry of springs, travertines and lacustrine carbonates of the Grand Canyon region over the past 12 million years: *Geosphere*, <https://doi.org/10.1130/GES01073.1>.
- De Filippis, L., Faccenna, C., Billi, A., Anzalone, E., Brillì, M., Soligo, M., and Tuccimei, P., 2013, Plateau versus fissure ridge travertines from Quaternary geothermal springs of Italy and Turkey: Interactions and feedbacks between fluid discharge, paleoclimate, and tectonics: *Earth-Science Reviews*, v. 123, p. 35–52, doi:10.1016/j.earscirev.2013.04.004.
- Dickin, A.P., 1995, *Radiogenic Isotope Geology*. Cambridge University Press, Cambridge. 490.
- Dunbar, N., 2005, Quaternary volcanism in New Mexico: *New Mexico Museum of Natural History and Science Bulletin*, v. 28, p. 95–106.

- Durand, S., Chabaux, F., Rihs, S., Düringer, P., Elsass, P., 2005, U isotope ratios as tracers of groundwater inputs into surface waters: example of the Upper Rhine hydrosystem. *Chemical Geology* 220(1), 1-19.
- Duschatco, R.W., 1953, Fracture studies in the Lucero uplift, New Mexico: United States Atomic Energy Commission, RME-3072, 49 p.
- Edwards, R.L., Chen, J., and Wasserburg, G., 1987, ^{238}U - ^{234}U - ^{230}Th - ^{232}Th systematics and the precise measurement of time over the past 500,000 years: *Earth and Planetary Science Letters*, v. 81, p. 175–192, doi:10.1016/0012-821X(87)90154-3.
- Embid, E.H., 2009, U-Series dating, geochemistry, and geomorphic studies of travertines and springs of the Springerville area, east-central Arizona, and tectonic implications [M.S. thesis]: Albuquerque, University of New Mexico, 103 p.
- Epstein, S., Buchsbaum, R., Lowenstam, H.A. and Urey, H.C., 1953, Revised carbonate–water isotopic temperature scale: *Geol Soc Am Bull*: v. 64, p. 1315-1326.
- Faccenna, C., Soligo, M., Billi, A., De Filippis, L., Funicello, R., Rossetti, C., and Tuccimei, P., 2008, Late Pleistocene depositional cycles of the Lapis Tiburtinus travertine (Tivoli, central Italy): Possible influence of climate and fault activity: *Global and Planetary Change*, v. 63, p. 299–308, doi:10.1016/j.gloplacha.2008.06.006.
- Fleischer, R. L., 1980, Isotopic Disequilibrium of Uranium: Alpha-Recoil Damage and Preferential Solution Effects. *Science*, 207, 979
- Frery, E., 2012, Episodic circulation of reactive fluids along faults: From travertine- to basinscale on the Colorado Plateau natural example (USA) [Ph.D. thesis]: University of Grenoble 1, University of Leuven, 247 p.

- Formento- Tigilio M.L., and Pazzaglia, F.J., 1998, Tectonic geomorphology of the Sierra Nacimiento: Traditional and new techniques in assessing long-term landscape evolution in the southern Rocky Mountains: *Journal of Geology*, v. 106, p. 433-454.
- Frank N, Braum M, Hambach U, et al. 2000. Warm period growth of travertine during the last interglaciation in Southern Germany. *Quaternary Research* 54: 38–48.
- Garcia, S., 2017, Tracing anthropogenic salinity inputs to the semi-arid Rio Grande river: A multi-isotope tracer approach [M.S. thesis]: El Paso, University of Texas at El Paso, 90 p.
- Goff, F., McCormick, T., Gardner, J.N., Trujillo, P.E., Counce, D., Vidale, R., and Charles, R., 1983, Water geochemistry of the Lucero uplift, New Mexico: A geothermal investigation of low-temperature mineralized fluids: Los Alamos National Laboratory LA9738-OBES, 26 p., doi:10.2172/6246390.
- Goff F, Shevenel L. 1987. Travertine deposits of Soda Dam, New Mexico, and their implications for the age and evolution of the Valles caldera hydrothermal system. *Geological Society of America Bulletin* 99: 292–302.
- Goff, F., Evans, W.C., Gardner, J.N., Adams, A. and Janik, C.J., 1994. Interpretation of in-situ fluid samples from geothermal wells: example from hole VC-2B, Valles caldera, New Mexico. *Geothermal science and technology*, 4(2), pp.97-128.
- Giustini, F., Brilli, M., Mancini, M., 2018, Geochemical study of travertines along middle-lower Tiber valley (central Italy): genesis, palaeo-environmental and tectonic implications. *Int J Earth Sci (Geol Rundsch)* 107, 1321–1342 (2018). <https://doi.org/10.1007/s00531-017-1535-0>

- Hancock, P.L., Chalmers, R.M., Altunel, E., and Cakir, Z., 1999, Travitonics: Using travertines in active fault studies: *Journal of Structural Geology*, v. 21, p. 903–916, doi:10.1016/S0191-8141(99)00061-9.
- Hogan, J.F., Phillips, F.M., Mills, S.K., Hendrickx, J.M.H., Ruiz, J., Chesley, J.T., and Asmerom, Y., 2007, Geologic origins of salinization in a semi-arid river: The role of sedimentary basin brines: *Geology*, v. 35, p. 1063–1066, doi:10.1130/G23976A.1.
- Ivanovich, M. and Harmon, R.S., 1992, Uranium-series disequilibrium: Applications to earth, marine, and environmental sciences. Clarendon Press, Oxford University Press.
- Ivanovich, M., 1994. Uranium series disequilibrium: concepts and applications. *Radiochimica Acta*, 64(2), pp.81-94.
- Jochum, K.P., Weis, U., Schwager, B., Stoll, B., Wilson, S.A., Haug, G.H., Andreae, M.O. and Enzweiler, J., 2016. Reference values following ISO guidelines for frequently requested rock reference materials. *Geostandards and Geoanalytical Research*, 40(3), pp.333-350.
- Jweda, J., Bolge, L., Class, C., and Goldstein, S. L., 2016, High precision Sr-Nd-Hf-Pb isotopic compositions of USGS reference material BCR-2: *Geostandards and Geoanalytical Research*, v. 40, n. 1, p. 101–115, <https://doi.org/10.1111/j.1751-908X.2015.00342.x>
- Kampman, N., Burnside, N.M., Shipton, Z.K., Chapman, H.J., Nicholl, J.A., Ellam, R.M., and Bickle, M.J., 2012, Pulses of carbon dioxide emissions from intra- crustal faults following climatic warming: *Nature Geo- science*, v. 5, p. 352–358, doi:10.1038/ngeo1451.
- Kirkland, D.W., Denison, R.E., and Evans, R., 1995, Middle Jurassic Todilto Formation of Northern New Mexico and Southwestern Colorado: Marine or Nonmarine?: New Mexico Bureau of Mines and Mineral Resources Bulletin 147, 37 p.

- Kolomaznik, M., Ricketts, J.W., Priewisch, A., Crossey, L.J., Karlstrom, K.E., Asmerom, Y., and Polyak, V., 2013, U-series dating and stable isotope analysis of Quaternary travertines with implications for incision rates in western Rio Grande rift, Carrizo Arroyo, New Mexico: N. M. Geological Society, Guidebook 64, p. 199-204.
- Konter, J. G., Storm, L. P., 2014. High Precision $^{87}\text{Sr}/^{86}\text{Sr}$ Measurements by MC-ICP-MS, Simultaneously Solving for Kr Interferences and Mass-Based Fractionation. *Chemical Geology*, 385(2014): 26–34
- Kronfeld, J., Gradsztajn, E., Muller, H. W., Radin, J., Yaniv, A., and Zach, R., 1975, Excess ^{234}U : An aging effect in confined waters: *Earth and Planetary Science Letters*, v. 27, p. 342–345.
- Kronfeld, J., Vogel, J.C. and Talma, A.S., 1994. A new explanation for extreme $^{234}\text{U}/^{238}\text{U}$ disequilibria in a dolomitic aquifer. *Earth and Planetary Science Letters*, 123(1-3), pp.81-93.
- Ludwig, K. R. (2012). *Isoplot 3.75: A geochronology toolkit for Microsoft Excel*. Berkeley
- Luo, S.D. and Ku, T.L., 1991, U-Series Isochron Dating - A Generalized-Method Employing Total-Sample Dissolution. *Geochimica Et Cosmochimica Acta*, 55(2): 555-564.
- May, S.J., Kelley, S.A., and Russell, L.R., 1994, Footwall unloading and rift shoulder uplifts in the Albuquerque Basin: Their relation to syn-rift fanglomerates and apatite fission-track ages, in Keller, G.R., and Cather, S.M., eds., *Basins of the Rio Grande Rift: Structure, Stratigraphy, and Tectonic Setting*: Geological Society of America, Special Paper 291, p. 125–134.
- McArthur, J.M., Howarth, R.J., and Bailey, T.R., 2001, Strontium isotope stratigraphy: LOWESS Version 3: Best fit to the marine Sr isotope curve for 0–509 Ma and accompanying look-

- up table for deriving numerical age: *Journal of Geology*, v. 109, p. 155–170, doi:10.1086/319243.
- McMillan, N. J., A. P. Dickin, and D. Haag, 2000, Evolution of magma source regions in the Rio Grande rift, southern New Mexico, *Geol. Soc. Am. Bull.*, 112, 1582 – 1593.
- Miocic, J.M., Gilfillan, S.M., Frank, N., Schroeder-Ritzrau, A., Burnside, N.M. and Haszeldine, R.S., 2019. 420,000 year assessment of fault leakage rates shows geological carbon storage is secure. *Scientific reports*, 9(1), pp.1-9.
- Morgan, P., Seager, W.R., and Golombek, M.P., 1986, Cenozoic thermal, mechanical, and tectonic evolution of the Rio Grande rift: *Journal of Geophysical Research*, v. 91, p. 6263-6276, <https://doi.org/10.1029/JB091iB06p06263>.
- Mukhopadhyay, B. and Brookins, D.G., 1976. Strontium isotopic composition of the Madera Formation (Pennsylvanian) near Albuquerque, New Mexico. *Geochimica et Cosmochimica Acta*, 40(6), pp.611-616.
- Newell, D.L., Crossey, L.J., Karlstrom, K., Fischer, T., and Hilton, D., 2005, Evidence for continental-scale links between the mantle and groundwater systems of the Western United States based on hydrogeochemistry of travertine-depositing springs and regional synthesis of helium isotopic data: *GSA Today*, v. 15, no. 12, p. 4-10.
- Nuriel, P., Rosenbaum, G., Zhao, J.X., Feng, Y., Golding, S.D., Villemont, B., and Weinberger, R., 2012, U-Th dating of striated fault planes: *Geology*, v. 40, p. 647-650.
- Nyachoti, S.K., 2016, Application of uranium and strontium isotopes as salinity and paleo-environmental conditions tracers: Insight from the Rio Grande River and pedogenic carbonates in drylands soils of Southwest, USA. The University of Texas at El Paso.

- Özkul, M., Kele, S., Gökgöz, A., Shen, C.-C., Jones, B., Baykara, M.O., Fórizs, I., Németh, T., Chang, Y.-W., and Alçiçek, M.C., 2013, Comparison of the Quaternary travertine sites in the Denizli extensional basin based on their depositional and geochemical data: *Sedimentary Geology*, v. 294, p. 179–204, doi:10.1016/j.sedgeo.2013.05.018.
- Paces, J. B. and Wurster, F. C. (2014). Natural uranium and strontium isotope tracers of water sources and surface water–groundwater interactions in arid wetlands–Pahranagat Valley, Nevada, USA. *Journal of Hydrology*, 517, 213-225.
- Pentecost, A., 1995. The quaternary travertine deposits of Europe and Asia Minor. *Quaternary Science Reviews*, 14(10), pp.1005-1028.
- Pentecost, A., 2005, *Travertine*: Berlin, Springer Verlag, 445 p.
- Pett-Ridge, J.C., Derry, L.A., and Kurtz, A.C., 2009, Sr isotopes as a tracer of weathering processes and dust inputs in a tropical granitoid watershed, Luquillo Mountains, Puerto Rico: *Geochimica et Cosmochimica Acta* 73.1 (2009): 25-43.
- Pigati, J.S., Miller, D.M., Bright, J.E., Mahan, S.A., Nekola, J.C., and Paces, J.B., 2011, Chronology, sedimentology, and microfauna of groundwater discharge deposits in the central Mojave Desert, Valley Wells, California: *Geological Society of America Bulletin*, v. 123, p. 2224–2239, doi:10.1130/B30357.1.
- Priestley SC, Karlstrom KE, Love AJ, et al. 2018. Uranium series dating of Great Artesian Basin travertine deposits: Implications for palaeohydrogeology and palaeoclimate. *Palaeogeography, Palaeoclimatology, Palaeoecology* 490: 163–177.
- Priewisch, A., Crossey, L. J., Karlstrom, K. E., Polyak, V. J., Asmerom, Y., Nereson, A., & Ricketts, J. W. 2014, U-series geochronology of large-volume Quaternary travertine

- deposits of the southeastern Colorado Plateau: Evaluating episodicity and tectonic and paleohydrologic controls. *Geosphere*, 10(2), 401-423.
- Reiter, M., Chamberlin, R.M., and Love, D.W., 2010, New data reflect on the thermal antiquity of the Socorro magma body locale, Rio Grande Rift, New Mexico: *Lithosphere*, v. 2, p. 447–453, doi:10.1130/L115.1.
- Ricketts, J.W., Karlstrom, K.E., Priewisch, A., Crossey, L.J., Polyak, V.J., and Asmerom, Y., 2014, Quaternary extension in the Rio Grande rift at elevated strain rates recorded in travertine deposits, central New Mexico: *Lithosphere*, v. 6, p. 3–16, doi: 10.1130/L278.1.
- Rosholt, J.N., 1976, $^{230}\text{Th}/^{234}\text{U}$ dating of travertine and caliche rinds, *GSA abstr. Prog.* 8, 1076.
- Ricketts, J.W. and Karlstrom, K.E., 2014, Geologic map of the South Garcia SE 7.5-minute Quadrangle, Valencia County, New Mexico. New Mexico Bureau of Geology and Mineral Resources Open-File Geologic Map 246, scale 1: 24,000.
- Ricketts, J.W., Ma, L., Wagler, A.E. and Garcia, V.H., 2019, Global travertine deposition modulated by oscillations in climate. *J. Quaternary Sci.*, 34: 558-568. doi:[10.1002/jqs.3144](https://doi.org/10.1002/jqs.3144)
- Russell, L.R., and Snelson, S., 1994, Structure and tectonics of the Albuquerque Basin segment of the Rio Grande rift: Insights from reflection seismic data, in Keller, G.R., and Cather, S.M., eds., *Basins of the Rio Grande rift: Structure, stratigraphy, and tectonic setting*: Geological Society of America Special Paper 291, p. 83–112, doi:10.1130/SPE291-p83.
- Sanford, A. R., Mott, R. P., Shuleski, P. J., Rinehart, E. J., Caravella, F. J., Ward, R. M., and Wallace, T. C., 1977, Geophysical evidence for a magma body in the vicinity of Socorro, New Mexico; in Heacock, J. G., ed, *The Earth's Crust: Its Nature and Physical Properties*:

- Geophysical Monograph Series, 20, American Geophysical Union, Washington, D.C., p. 385-404.
- Scharman, Mitchell R., 2006, Structural constraints on Laramide shortening and Rio Grande rift extension in the central Franklin Mountains, El Paso County, Texas, M.S. Thesis, University of Texas at El Paso, El Paso, TX 79968, 70p.
- Sharp, Z. (2007) Stable Isotope Geochemistry. Pearson Prentice Hall, Upper Saddle River, NJ, 344 pp.
- Schmandt, B., and Humphreys, E., 2010, Complex subduction and small-scale convection revealed by body-wave tomography of the western United States upper mantle: *Earth and Planetary Science Letters*, v. 297, p. 435– 445, doi:10.1016/j.epsl.2010.06.047.
- Shaw, C.A., and Karlstrom, K.E., 1999, The Yavapai-Mazatzal crustal boundary in the southern Rocky Mountains: *Rocky Mountain Geology*, v. 34, p. 37-52.
- Sims K.W.W., Gill, J.B., Dosseto, A., Hoffmann, D.L., Lundstrom, C.C., Williams, R.W., Ball, L., Tollstrup, D., Turner, S., Pyrtulak, J., Glessner, J.G., Standish, J.J., Elliott, T. (2008). An Inter-Laboratory Assessment of the Thorium Isotopic Composition of Synthetic and Rock Reference Materials. *Geostandards and Geoanalytical Research* 32(1), 65-91.
- Sosa, A., Thompson L., Velasco, A. A., Romero, R., Herrmann, R. B., 2014, 3-D structure of the Rio Grande rift from 1-D constrained joint inversion of receiver functions and surface wave dispersion, *Earth Planet. Sci. Lett.*, 402, 127–137.
- Szabo, B., 1990, Ages of travertine deposits in eastern Grand Canyon National Park, Arizona: *Quaternary Research*, v. 34, p. 24-32.
- Tafoya, A.J., 2012, Uranium-Series Geochronology and Stable Isotope Analysis of Travertine from Soda Dam, New Mexico: A Quaternary Record of Episodic Spring Discharge and

- River Incision in the Jemez Mountains Hydrothermal System [M.S. thesis]: Albuquerque, New Mexico, University of New Mexico, 104 p.
- Taggart, J.E., and Brookins, D.G., 1975, Rb-Sr whole rock age determinations for Sandia granite and Cibola gneiss, New Mexico: *Isochron/West*, no. 12, p. 5–8.
- Temiz, U., Gökten, E., and Eikenberg, J., 2009, U/Th dating of fissure ridge travertines from the Kirsehir region (Central Anatolia Turkey): Structural relations and implications for the Neotectonic development of the Anatolian block: *Geodinamica Acta*, 24, 95-100.
- Thompson, R.A., Johnson, C.M., Mehnert, H.H., 1991, Oligocene basaltic volcanism of the northern Rio Grande rift: San Luis Hills, Colorado: *Journal of Geophysical Research*, v. 96, p. 13,577–13,592, doi:10.1029/91JB00068.
- Uysal IT, Feng Y, Zhao J, et al. 2007. U-series dating and geochemical tracing of late Quaternary travertine in co-seismic fissures. *Earth and Planetary Science Letters* 257: 450–462.
- Uysal, I.T., Feng, Y.X., Zhao, J. Isik, V., Nuriel, P., and Golding, S.D., 2009, Hydrothermal CO₂ degassing in seismically active zones during the later Quaternary: *Chemical Geology*, v. 265, p. 442-454.
- Van der Hoven, S.J. and Quade, J., 2002. Tracing spatial and temporal variations in the sources of calcium in pedogenic carbonates in a semiarid environment. *Geoderma*, 108(3-4), pp.259-276.
- Vuataz, F.D., Goff, F., Fouillac, C. and Calvez, J.Y., 1988. A strontium isotope study of the VC-1 core hole and associated hydrothermal fluids and rocks from Valles Caldera, Jemez Mountains, New Mexico. *Journal of Geophysical Research: Solid Earth*, 93(B6), pp.6059-6067.

- Williams, A.J., Crossey, L.J., Karlstrom, K.E., Newell, D., Person, M., and Woolsey, E., 2013, Hydrogeochemistry of the Middle Rio Grande aquifer system—Fluid mixing and salinization of the Rio Grande due to fault inputs: *Chemical Geology*, v. 351, p. 281–298, doi:10.1016/j.chemgeo.2013.05.029.
- Williams, R.T., Goodwin, L.B., Mozley, P.S., Beard, B.L., and Johnson, C.M., 2015, Tectonic controls on fault zone flow pathways in the Rio Grande rift, New Mexico, USA: *Geology*, v. 43, p. 723–726, doi: 10.1130/G36799.1.
- Williams, R.T., Goodwin, L.B., Mozley, P.S., 2016. Diagenetic controls on the evolution of fault-zone architecture and permeability structure: implications for episodicity of fault-zone fluid transport in extensional basins. *Geol. Soc. Am. Bull.* B31443.1.
- Williams, R. T., Goodwin, L. B., Sharp, W. D., & Mozley, P. S. (2017). Reading a 400,000-year record of earthquake frequency for an intraplate fault. *Proceedings of the National Academy of Sciences of the United States of America*, 114(19), 4893–4898. <https://doi.org/10.1073/pnas.1617945114>
- Williams, R. T., Beard, B. L., Goodwin, L. B., Sharp, W. D., Johnson, C. M., & Mozley, P. S. (2018). Radiogenic isotopes record a “drop in a bucket”—A fingerprint of multikilometer-scale fluid pathways inferred to drive fault-valve behavior. *Journal of Structural Geology*, 125, 262–269. <https://doi.org/10.1016/j.jsg.2018.07.023>
- Young, B. W., & Chan, M. A. (2017). Gypsum veins in Triassic Moenkopi mudrocks of southern Utah: Analogs to calcium sulfate veins on Mars. *Journal of Geophysical Research: Planets*, 122, 150–171. <https://doi.org/10.1002/2016JE005118>

Zentmyer, R., Myrow, P.M., Newell, D.L., 2008, Travertine deposits from along the South Tibetan Fault System near Nyalam, Tibet: *Geological Magazine*, v. 145, p. 753-765, doi: 10.1017/S0016756808005323.

Zieliński, M., Dopieralska, J., Belka, Z., Walczak, A., Siepak, M., Jakubowicz, M., 2016, Sr isotope tracing of multiple water sources in a complex river system, Noteć River, central Poland. *Science of the Total Environment*, 548-549, 307–316. <https://doi.org/10.1016/j.scitotenv.2016.01.0363.9>

3.9 TABLES

Table 3.1 Sample Locations and Descriptions

Sample ¹	Coordinates		Description of Travertine	Stratigraphy ²	Elevation (m)
	Name	Latitude			
TPL04	34.877537°	-107.087271°	thick cm-scale layered travertine located at base of basin floor near tilted Dakota Sandstone	Qtr1	1628
TPL07	34.871853°	-107.088024°	mm-scale layered, milky white travertine on top of Dakota Sandstone	Qtr3	1686
TPL10	34.874845°	-107.089183°	cm-scale layered travertine collected on top of tilted Dakota Sandstone	Qtr3	1672
TPL14	34.870413°	-107.090548°	layered travertine collected at edge of large eroded travertine mound	Qtr1	1664
TPL16	34.869249°	-107.090037°	cm-scale layered travertine with Fe- and Mn-oxides from tilted block	Qtr2	1684
TPL17	34.867917°	-107.090430°	top portion is cm-scale botryoidal travertine while bottom is cm-layered travertine	Qtr2	1697
TPL19	34.865841°	-107.090585°	cm-scale layered travertine collected above active travertine precipitating spring	Qtr1	1668
TPL21	34.863192°	-107.090474°	cm-scale layered travertine with Fe-oxide found at base	Qtr1	1677
TPL23	34.857370°	-107.093531°	cm-scale layered and clear travertine from draped surface	Qtr1	1691
TPL25	34.859448°	-107.086967°	mm-scale layered travertine at base of incised travertine mound	Qtr1	1678
TPL26	34.858250°	-107.085329°	thick cm-scale layered travertine found on top while bottom is mm-scale layered travertine	Qtr1	1663
TPL30	34.827493°	-107.084553°	very dense mm-scale layered travertine collect at base of large travertine flow deposit	Qtr1	1632
TPL31	34.829979°	-107.081543°	mm-scale layered travertine collected on top of tilted Santa Fe Group	Qtr2	1645
TPL34	34.800498°	-107.086267°	cm-scale blocky and very clear travertine veins; collected near exposure of San Andres Limestone	Qtr1	1682
TPL35	34.803581°	-107.086300°	mm-scale layered travertine with voids collected on top of tilted Santa Fe Group	Qtr3	1663
TPL35V	34.803581°	-107.086300°	vein cutting through TPL35	Qtr2	1663
TPL36	34.804158°	-107.086829°	mm-scale layered travertine, with pool and dam structures, on active travertine slope	Qtr1	1666
TPL38	34.804414°	-107.087152°	blocky travertine layers interlayered with Fe- and Mn-oxide material in incised area	Qtr1	1673
TPL39	34.805216°	-107.088189°	cm-scale botryoidal clear travertine collected on top of tilted Santa Fe Group	Qtr2	1714
TPL2-1	34.804140°	-107.086202°	mm-scale layered travertine collected at base of large travertine flow deposit	Qtr1	1650
TPL2-3	34.804907°	-107.086851°	travertine material collected at base of large travertine mound located on top of tilted Santa Fe Group	Qtr2	1681
TPL2-4	34.804855°	-107.087661°	mm-scale layered travertine collected at middle of large travertine mound right on top of tilted Santa Fe Group	Qtr2	1703
TPL2-5	34.804855°	-107.087661°	cm-scale layered travertine collected top of large travertine mound located on top of tilted Santa Fe Group	Qtr3	1703
TPL2-7BASE	34.826841°	-107.083973°	travertine material collected right on top of tilted Santa Fe Group near active travertine mounds	Qtr2	1625
TPL2-7	34.826841°	-107.083973°	cm-scale layered travertine collect above tilted Santa Fe Group	Qtr2	1625

¹A total of 47 travertine samples were collected for this study but only 25 samples of significant importance were analyzed and reported here.

²Travertine stratigraphy was determined by Ricketts and Karlstrom (2014) mapping, which was based on elevation (e.g. Qtr1 = low elevations = youngest; Qtr3 = high elevations = oldest).

Table 3.2 Travertine Geochronology

Sample ID	Sample Name	²³⁸ U (ppm)	²³² Th (ppm)	Measured Activity Ratios						^(234U/238U) _i ¹	± 2se	Age ¹ (ka)	± 2se	
				^(234U/238U) _m	±	^(230Th/238U) _m	±	^(232Th/238U) _m	±					
VG1	TPL04-Middle	1.983	0.120	4.991	0.025	0.060	0.001	0.020	0.000	5.00	0.03	0.94	0.01	
VG2	TPL07-Bottom	2.683	0.119	2.079	0.010	2.493	0.025	0.015	0.000	5.35	0.37	494.00	33.00	
VG3	TPL07-Middle	1.685	0.105	2.073	0.010	2.523	0.025	0.020	0.000	6.43	0.82	574.00	56.00	
VG4	TPL07-Top	2.083	0.261	2.063	0.010	2.492	0.025	0.041	0.000	5.25	0.41	491.00	37.00	
VG5	TPL10-BB	1.085	0.243	2.602	0.013	3.273	0.033	0.073	0.001	7.61	0.50	502.00	30.00	
VG6	TPL10-Bottom	1.686	0.577	2.521	0.013	3.147	0.031	0.112	0.001	6.34	0.53	445.00	37.00	
VG7	TPL10-BT	1.688	0.079	2.679	0.013	3.300	0.033	0.015	0.000	7.27	0.30	467.00	20.00	
VG8	TPL10-Middle	1.732	0.146	2.676	0.013	3.652	0.037	0.028	0.000	nd	nd	nd	nd	
VG9	TPL10-Top	2.485	0.094	2.695	0.013	3.603	0.036	0.012	0.000	nd	nd	nd	nd	
VG10	TPL14B-Middle	4.029	0.077	5.127	0.026	0.286	0.003	0.006	0.000	5.20	0.03	6.09	0.80	
VG11	TPL14M-Middle	2.243	0.024	5.074	0.025	0.689	0.007	0.003	0.000	5.26	0.03	15.56	0.24	
VG12	TPL14T-Middle	2.466	0.009	5.158	0.026	0.308	0.003	0.001	0.000	5.24	0.03	6.63	0.24	
VG13	TPL16-Bottom	1.677	0.020	4.168	0.021	3.617	0.036	0.004	0.000	5.90	0.01	154.20	1.40	
VG14	TPL16-Middle	3.391	0.006	4.303	0.022	3.663	0.037	0.001	0.000	6.03	0.03	148.90	2.60	
VG15	TPL16-Top	3.560	0.010	4.263	0.021	3.468	0.035	0.001	0.000	5.82	0.04	137.90	2.70	
VG16	TPL17-B	2.520	0.009	3.449	0.017	4.292	0.043	0.001	0.000	9.29	0.68	432.00	30.00	
VG17	TPL17-M	2.372	0.023	3.450	0.017	4.275	0.043	0.003	0.000	9.02	0.60	420.00	28.00	
VG18	TPL17-T	2.542	0.001	3.462	0.017	0.443	0.004	0.000	0.000	3.57	0.02	14.71	0.17	
VG19	TPL19-B	2.420	0.014	4.673	0.023	2.247	0.022	0.002	0.000	5.41	0.00	65.09	0.03	
VG20	TPL19-M	2.306	0.007	4.644	0.023	2.302	0.023	0.001	0.000	5.41	0.03	67.68	0.97	
VG21	TPL19-T	2.242	0.054	4.613	0.023	2.223	0.022	0.008	0.000	4.17	0.00	24.23	0.01	
VG22	TPL21-B	2.297	0.013	5.300	0.027	0.249	0.002	0.002	0.000	5.36	0.00	5.17	0.00	
VG23	TPL21-T	2.161	0.026	5.264	0.026	0.226	0.002	0.004	0.000	5.32	0.00	4.68	0.00	
VG24	TPL23-B	18.921	0.008	1.135	0.006	1.222	0.012	0.000	0.000	nd	nd	nd	nd	
VG25	TPL23-M	17.589	0.209	1.152	0.006	1.251	0.013	0.004	0.000	nd	nd	nd	nd	
VG26	TPL23-T	18.022	0.057	1.133	0.006	1.293	0.013	0.001	0.000	nd	nd	nd	nd	
VG27	TPL25-M	1.895	0.019	5.056	0.025	0.106	0.001	0.003	0.000	5.08	0.00	2.24	0.00	
VG28	TPL26-T	2.253	0.026	1.235	0.006	1.389	0.014	0.004	0.000	nd	nd	nd	nd	
VG29	TPL30-B	2.276	0.007	3.959	0.020	0.436	0.004	0.001	0.000	4.06	0.00	11.48	0.00	
VG30	TPL30-M1	1.365	0.020	3.959	0.020	0.531	0.005	0.005	0.000	4.09	0.00	15.31	0.00	
VG31	TPL30-M2	1.342	0.008	3.963	0.020	0.564	0.006	0.002	0.000	4.10	0.00	16.38	0.01	
VG32	TPL30-T	1.478	0.244	3.962	0.020	0.856	0.009	0.054	0.001	4.17	0.00	24.23	0.01	
VG33	TPL31-B	0.592	0.121	3.000	0.015	3.783	0.038	0.067	0.001	8.44	0.80	466.00	39.00	
VG34	TPL31-M	0.537	0.118	2.945	0.015	3.463	0.035	0.072	0.001	5.86	0.01	324.37	0.65	
VG35	TPL31-T	0.689	0.104	2.613	0.013	3.090	0.031	0.050	0.001	5.39	0.21	355.00	18.00	
VG36	TPL34-B	2.103	0.010	3.994	0.020	2.339	0.023	0.002	0.000	4.80	0.02	84.60	1.30	
VG37	TPL34-M	2.247	0.005	4.060	0.020	2.337	0.023	0.001	0.000	4.86	0.02	82.70	1.30	
VG38	TPL34-T	2.359	0.010	4.087	0.020	2.311	0.023	0.001	0.000	4.88	0.02	80.70	1.20	
VG39	TPL35-T	1.659	0.024	3.546	0.018	4.094	0.041	0.005	0.000	7.04	0.01	305.91	0.61	
VG40	TPL35-V	9.026	0.009	3.584	0.018	3.656	0.037	0.000	0.000	5.77	0.00	217.06	0.26	
VG41	TPL36-B	2.371	0.009	4.124	0.021	0.077	0.001	0.001	0.000	4.14	0.00	2.02	0.00	
VG42	TPL36-M	0.442	0.007	4.113	0.021	0.450	0.005	0.005	0.000	4.22	0.00	12.34	0.00	
VG43	TPL36-T	3.236	0.017	4.089	0.020	0.071	0.001	0.002	0.000	4.11	0.00	1.86	0.00	
VG44	TPL38-M	3.387	0.006	4.164	0.021	0.158	0.002	0.001	0.000	4.20	0.00	4.20	0.00	
VG45	TPL39-M	3.384	0.007	2.187	0.011	2.579	0.026	0.001	0.000	4.93	0.01	424.40	1.40	
VG46	TPL2-1	1.663	0.088	3.785	0.019	1.837	0.018	0.017	0.000	4.35	0.02	65.59	0.94	
VG47	TPL2-3B	1.628	0.823	1.947	0.010	2.470	0.025	0.166	0.002	6.00	1.60	592.00	110.00	
VG48	TPL2-4	4.718	0.008	2.183	0.011	2.362	0.024	0.001	0.000	4.13	0.15	351.00	19.00	
VG49	TPL2-5B	4.398	0.051	2.175	0.011	2.353	0.024	0.004	0.000	5.29	0.05	456.00	41.00	
VG50	TPL2-5M	4.181	0.010	2.181	0.011	2.620	0.026	0.001	0.000	5.24	0.46	455.00	40.00	
VG51	TPL2-5T	30.853	0.026	2.160	0.011	2.560	0.026	0.000	0.000	5.71	0.67	490.00	52.00	
VG52	TPL2-7 BASE	1.641	0.956	2.683	0.013	2.904	0.029	0.191	0.002	5.02	0.13	309.00	13.00	
VG53	TPL2-7B	11.217	0.034	3.303	0.017	2.901	0.029	0.001	0.000	4.99	0.05	194.90	4.70	
VG54	TPL2-7M	11.440	0.011	3.309	0.017	3.424	0.034	0.000	0.000	5.01	0.05	195.80	4.80	
VG55	TPL2-7T	10.718	0.009	3.307	0.017	2.909	0.029	0.000	0.000	5.01	0.05	195.50	4.70	
¹ (^{234U/238U}) _i and ages determined using Isoplot 3.7														
not determined														

Table 3.3 Travertine Isotope Data

Sample ID	Sample Name	$\delta^{13}\text{C}$ (VPDB) ¹	±	$\delta^{18}\text{O}$ (VSMOW) ²	±	(⁸⁷ Sr/ ⁸⁶ Sr) ^{c3}	± 2se
T1	TPL04-Middle	4.54	0.02	21.77	0.01	0.71581	0.00002
T2	TPL07-Bottom	4.16	0.01	23.74	0.02	0.71527	0.00002
T3	TPL07-Middle	4.10	0.01	23.88	0.03	0.71525	0.00003
T4	TPL07-Top	4.16	0.01	23.65	0.01	0.71525	0.00002
T5	TPL10-BB	4.48	0.02	24.27	0.02	nd	nd
T6	TPL10-Bottom	4.22	0.00	24.82	0.03	nd	nd
T7	TPL10-BT	5.41	0.01	25.08	0.01	0.71475	0.00029
T8	TPL10-Middle	2.82	0.01	24.65	0.01	nd	nd
T9	TPL10-Top	5.10	0.02	24.58	0.02	nd	nd
T10	TPL14B-Middle	7.41	0.01	24.67	0.02	0.71625	0.00002
T11	TPL14M-Middle	6.40	0.02	23.53	0.01	0.71626	0.00001
T12	TPL14T-Middle	5.30	0.01	24.32	0.01	0.71628	0.00002
T13	TPL16-Bottom	3.82	0.01	23.12	0.01	0.71664	0.00005
T14	TPL16-Middle	3.99	0.01	23.57	0.02	0.71664	0.00005
T15	TPL16-Top	3.55	0.01	23.41	0.02	0.71681	0.00002
T16	TPL17-B	5.25	0.01	25.91	0.02	0.71527	0.00002
T17	TPL17-M	5.13	0.01	25.26	0.02	0.71525	0.00003
T18	TPL17-T	4.46	0.01	24.32	0.02	0.71525	0.00002
T19	TPL19-B	6.37	0.01	24.90	0.02	0.71704	0.00004
T20	TPL19-M	6.39	0.01	24.96	0.01	0.71710	0.00002
T21	TPL19-T	6.29	0.02	24.88	0.01	0.71710	0.00002
T22	TPL21-B	5.63	0.01	22.58	0.01	0.71658	0.00006
T23	TPL21-T	5.95	0.01	23.99	0.02	0.71651	0.00003
T24	TPL23-B	2.95	0.01	21.06	0.01	0.71416	0.00007
T25	TPL23-M	2.41	0.01	18.99	0.01	0.71435	0.00002
T26	TPL23-T	2.47	0.01	19.23	0.02	0.71430	0.00003
T27	TPL25-M	5.41	0.01	21.96	0.01	0.71662	0.00011
T28	TPL26-T	3.09	0.00	24.00	0.01	0.71413	0.00005
T29	TPL30-B	5.18	0.01	22.98	0.01	0.71676	0.00002
T30	TPL30-M1	4.47	0.01	23.13	0.02	0.71678	0.00002
T31	TPL30-M2	4.44	0.01	22.93	0.01	0.71681	0.00004
T32	TPL30-T	4.85	0.01	23.54	0.02	nd	nd
T33	TPL31-B	4.67	0.01	24.01	0.02	0.71521	0.00003
T34	TPL31-M	4.80	0.01	24.15	0.02	0.71529	0.00005
T35	TPL31-T	4.65	0.00	23.90	0.02	0.71520	0.00004

T36	TPL34-B	3.65	0.01	22.66	0.02	0.71446	0.00003
T37	TPL34-M	4.44	0.00	23.57	0.02	0.71420	0.00002
T38	TPL34-T	4.79	0.01	23.50	0.01	0.71413	0.00004
T39	TPL35-T	4.37	0.01	22.23	0.01	0.71567	0.00002
T40	TPL35-V	6.54	0.00	23.47	0.01	0.71569	0.00005
T41	TPL36-B	4.80	0.01	20.99	0.01	0.71561	0.00018
T42	TPL36-M	4.70	0.00	20.84	0.02	0.71591	0.00003
T43	TPL36-T	5.03	0.01	21.20	0.01	0.71593	0.00002
T44	TPL38-M	4.29	0.02	20.90	0.02	0.71588	0.00003
T45	TPL39-M	3.46	0.00	22.44	0.02	0.71596	0.00002
T46	TPL2-1	2.51	0.00	21.75	0.01	0.71494	0.00003
T47	TPL2-3B	3.98	0.01	23.92	0.01	0.71577	0.00003
T48	TPL2-4	7.63	0.01	25.32	0.02	0.71596	0.00003
T49	TPL2-5B	5.33	0.01	24.06	0.03	0.71606	0.00002
T50	TPL2-5M	4.69	0.01	23.88	0.03	0.71603	0.00002
T51	TPL2-5T	4.53	0.01	23.88	0.02	0.71598	0.00006
T52	TPL2-7 BASE	5.16	0.01	24.13	0.01	0.71602	0.00002
T53	TPL2-7B	7.90	0.00	25.72	0.02	0.71646	0.00002
T54	TPL2-7M	8.28	0.01	25.92	0.02	0.71647	0.00004
T55	TPL2-7T	8.24	0.01	25.64	0.02	0.71637	0.00002
¹ Analyzed at Paleoenvironmental & Environmental Stable Isotope Laboratory at Kansas University							
² Converted from VPDB to VSMOW							
³ Analyzed at Center for Earth and Environmental Sciences at the University of Texas at El Paso.							
nd = not determined							

Table 3.4 Travertine Growth Rates

Sample Name	Distance (from top in mm)	Age (kyr)	2se (kyr)	RATE (mm/kyr)
TPL07T	4	491.0	37.00	0.08
TPL07M	9	574.0	56.00	
TPL07B	17	494.0	33.00	
TPL10BB	20	502.0	30.00	0.29
TPL10BT	10	467.0	20.00	
TPL16T	4	137.9	2.70	0.68
TPL16M	9	148.9	2.60	
TPL16B	15	154.2	1.40	
TPL17T	10	14.7	0.17	0.06
TPL17M	25	420.0	28.00	
TPL17B	36	432.0	30.00	
TPL19T	9	24.2	0.01	0.72
TPL19M	20	67.7	0.97	
TPL19B	36	65.1	0.03	
TPL21T	2	4.7	0.00	34.48
TPL21B	19	5.2	0.00	
TPL30T	11	24.2	0.01	7.73
TPL30M1	35	15.3	0.00	
TPL30M2	66	16.4	0.01	
TPL30B	94	11.5	0.00	
TPL31T	5	355.0	18.00	0.12
TPL31M	10	324.4	0.65	
TPL31B	20	466.0	39.00	
TPL34T	5	80.7	1.20	16.08
TPL34M	42	82.7	1.30	
TPL34B	67	84.6	1.30	
TPL36T	7	1.9	0.00	2.64
TPL36M	38	12.3	0.00	
TPL36B	62	2.0	0.00	
TPL2-5T	8	490.0	52.00	0.96
TPL2-5M	27	455.0	40.00	
TPL2-5B	42	456.0	41.00	
TPL2-7T	15	195.5	4.70	53.19
TPL2-7M	31	195.8	4.80	
TPL2-7B	39	194.9	4.70	

3.10 FIGURES

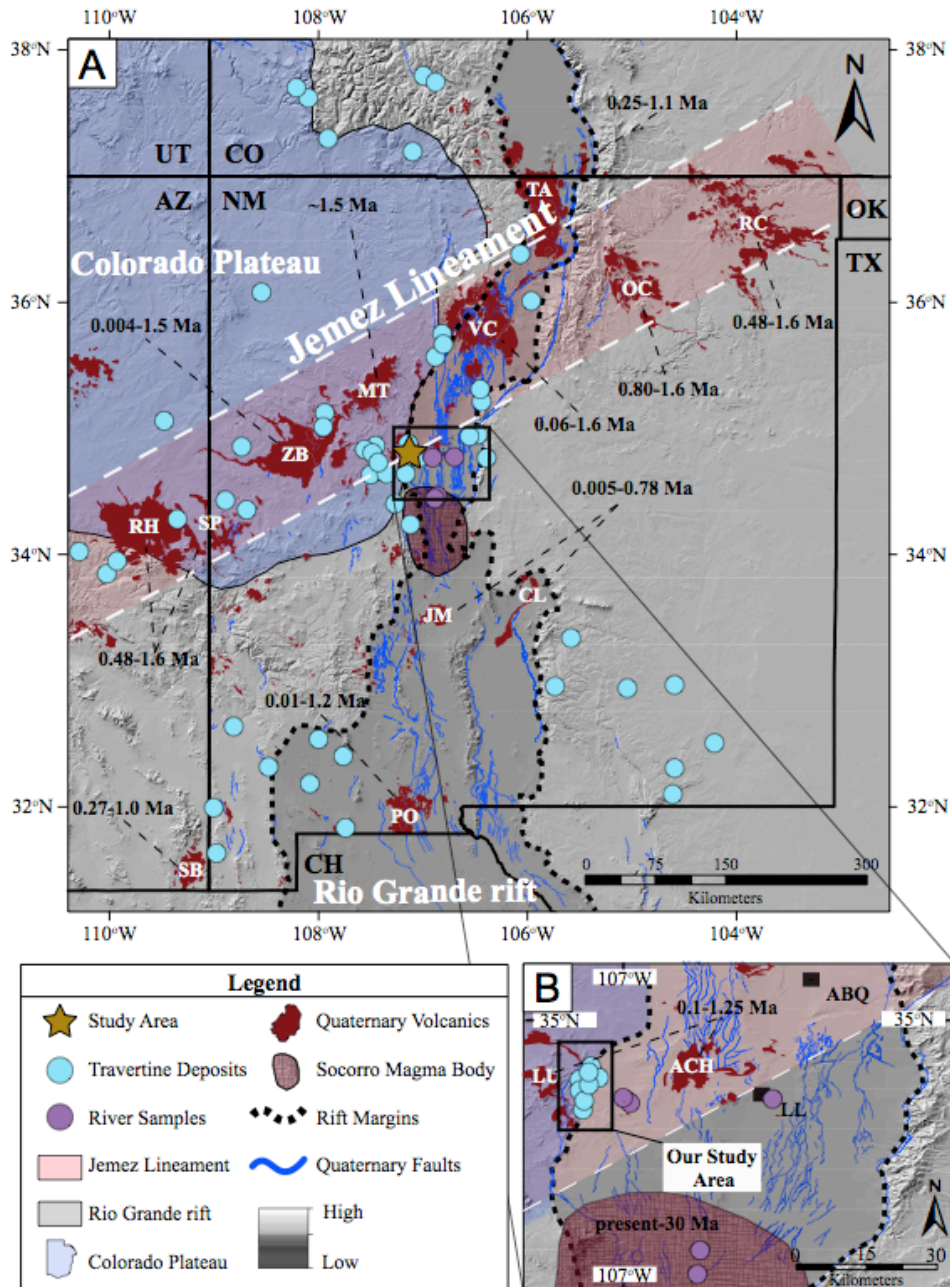


Figure 3.1 A) Regional digital elevation model showing location of travertine deposits in association with the Jemez Lineament, Rio Grande rift, Quaternary volcanism, and Quaternary faults (Barker et al., 1996). Travertine locations in the southern New Mexico (within the Rio Grande rift) were removed because the authors of this study visited those locations and determined they were not travertine deposits. Refer to Barker et al., 1996 for all location descriptions. B) Location of study area within the Jemez Lineament (red shaded region) on the western margin of the Rio Grande rift. Also shown is the Socorro magma body, which has been active since ~ 30 Ma.

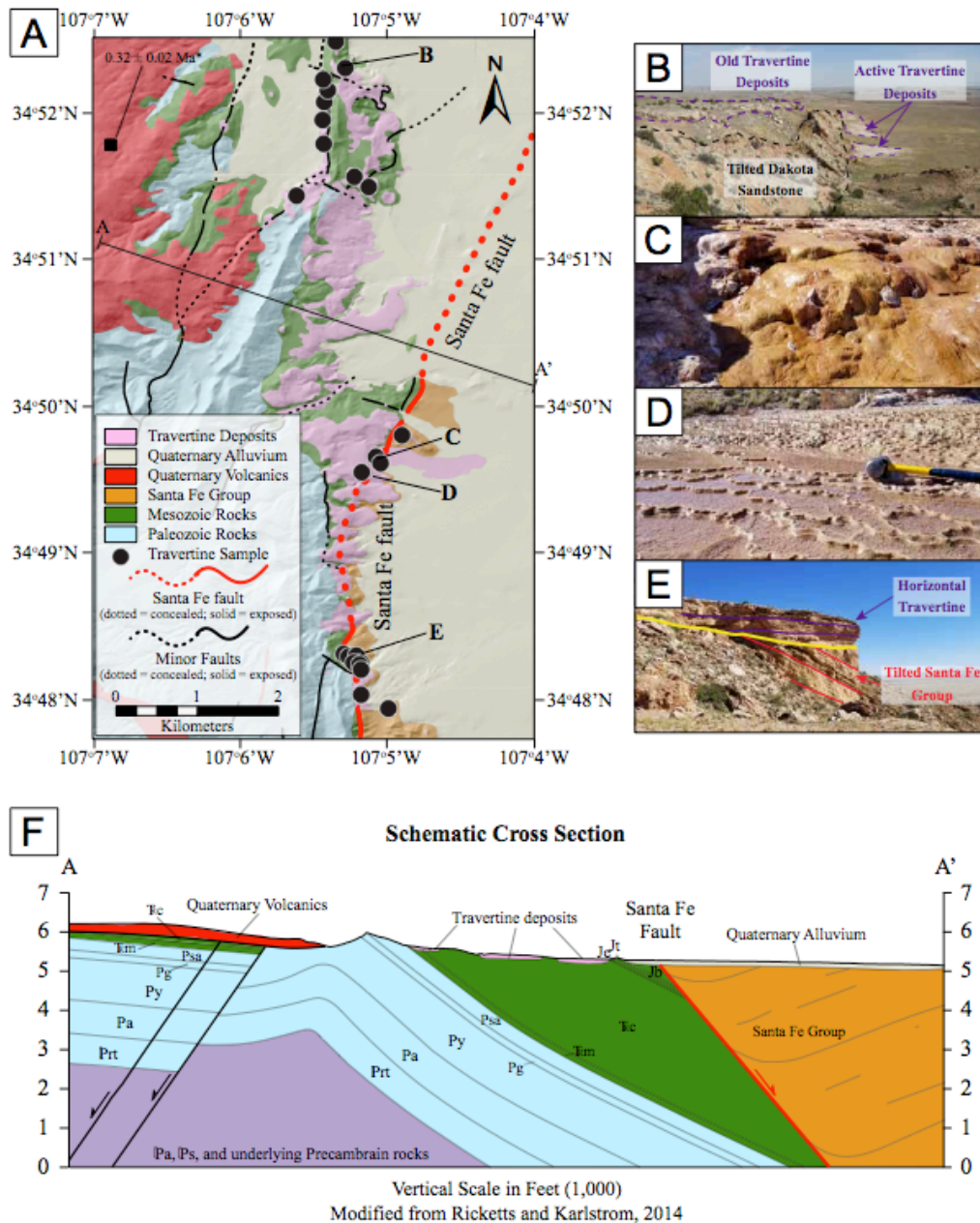


Figure 3.2 A) Geologic map of study area showing location of travertine deposits and location of collected samples. B) Image of tilted Mesozoic units and younger horizontal travertine deposits forming at high elevations (older travertine deposits) and lower elevations (younger travertine deposits). C) Image of active travertine precipitation forming drapes and curtains. Red-orange color due to Fe-oxide material co-precipitating with travertine. D) Image of small travertine pool and dam structures that are active. E) Tilted Santa Fe group overlaid by undeformed travertine deposits. F) Cross section through study area showing Precambrian, Paleozoic, Mesozoic, and Quaternary units.

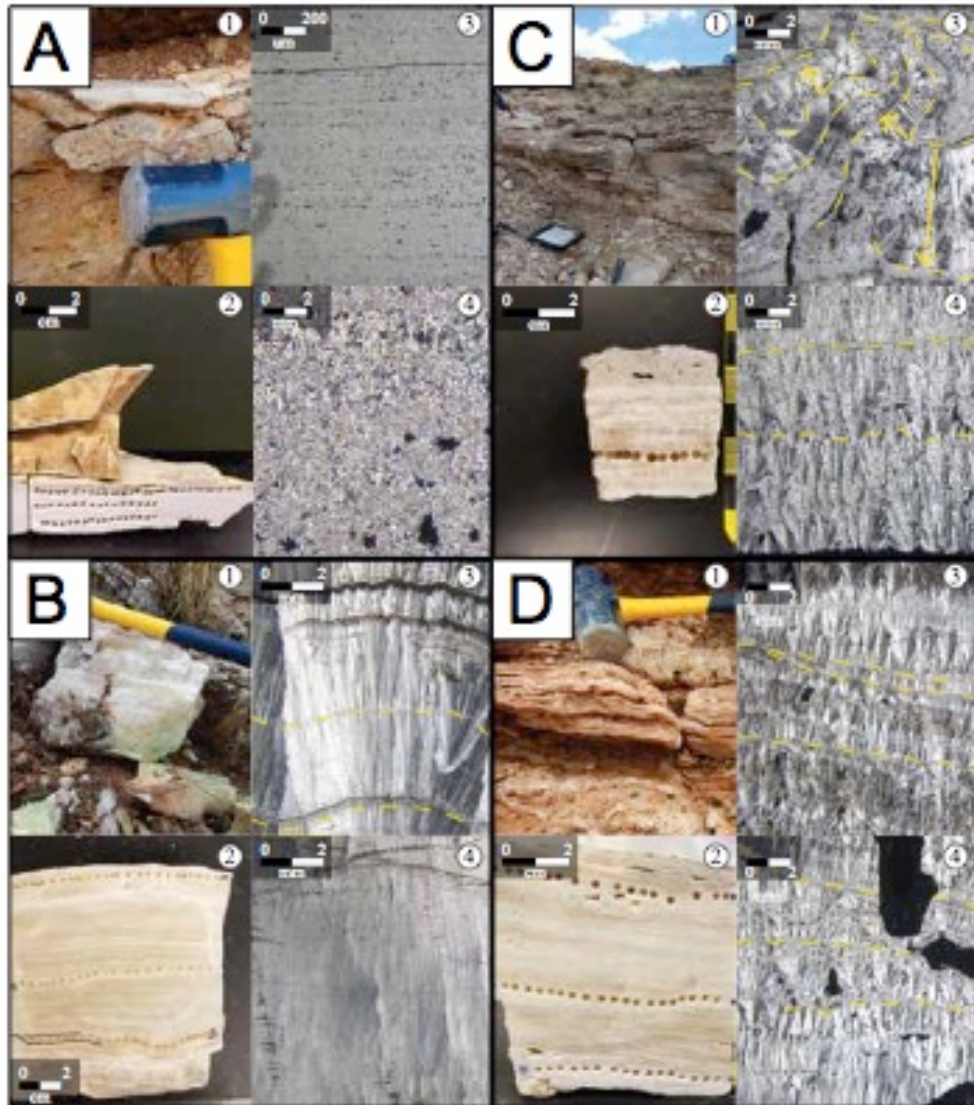


Figure 3.3 Images of collected travertine samples. Number on image refers to: 1 = travertine sample, 2 = drilling of hand sample, 3 and 4 = thin sections of travertine samples. A) Thin micritic layers in which textures are difficult to discern and many voids are present in the sample. B) Multiple thick botryoidal travertine layers (separated by yellow dashed line) with travertine growth indicated by radiating upward geometry of elongate calcite fibers. C) Chaotic travertine growth from multiple layers radiating in many different directions. D) Thick botryoidal travertine layers with many voids showing easy dissolution of material.

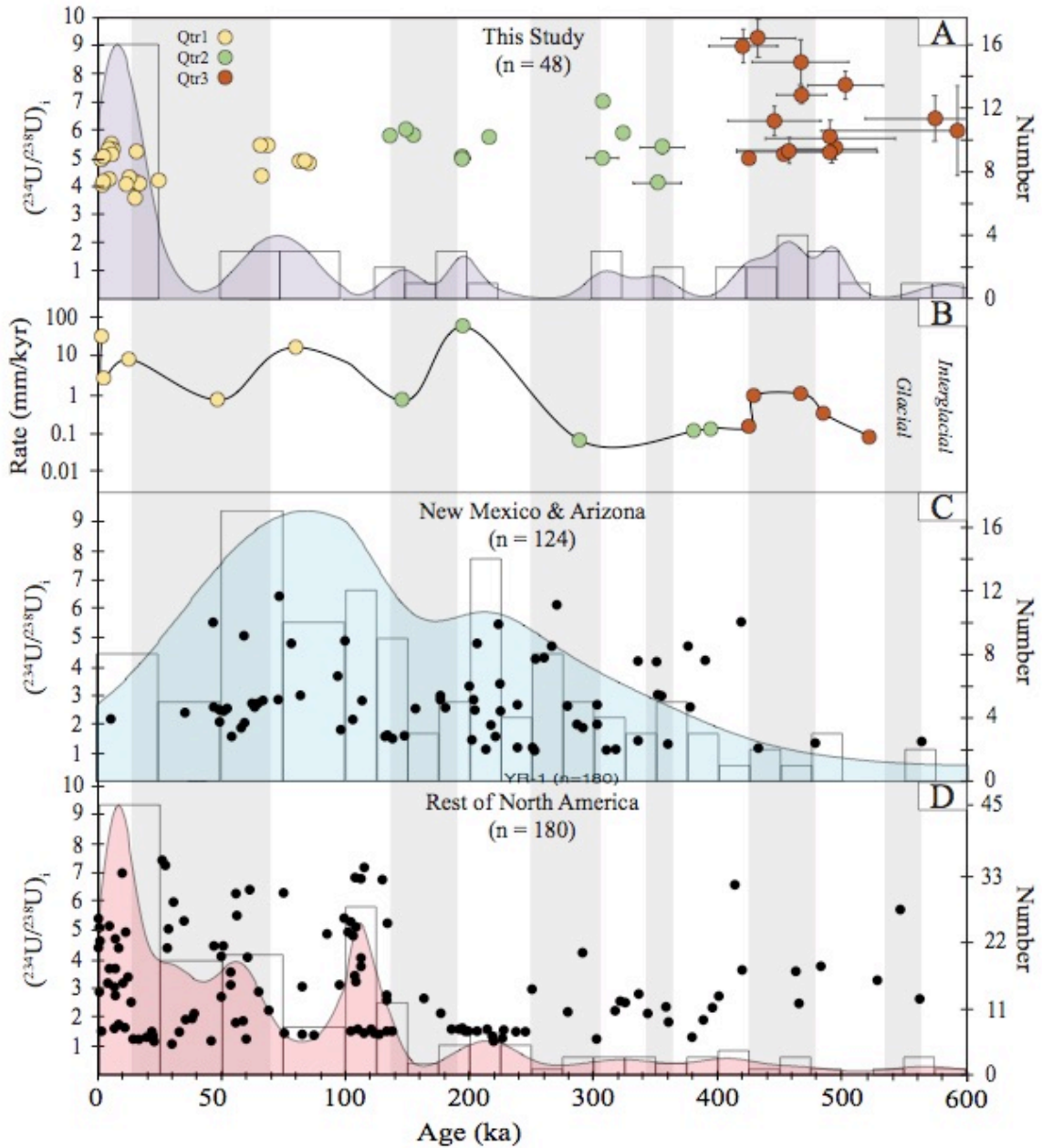


Figure 3.4 A) U-series travertine ages from this study plotted against $(^{234}\text{U}/^{238}\text{U})_i$. Kernel density estimate (KDE) and histograms of data shown. U-series ages determined using Berkeley Geochronology Center's Isoplot software v.3.75. B) Travertine precipitation rates. C) U-series travertine ages, from other travertine studies in the Rio Grande rift and along the Jemez Lineament, plotted against $(^{234}\text{U}/^{238}\text{U})_i$. Kernel density estimate (KDE) and histograms of data shown. D) U-series travertine ages, from all other travertine/calcite vein studies in North America, plotted against $(^{234}\text{U}/^{238}\text{U})_i$. Kernel density estimate (KDE) and histograms of data shown. Vertical grey rectangles refer to glacial periods while white rectangles represent interglacial periods.

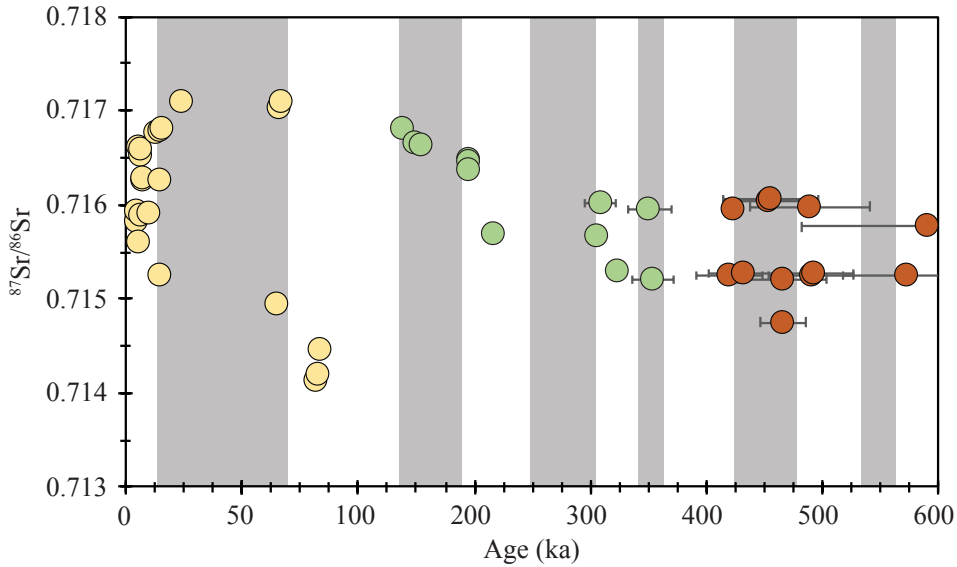


Figure 3.5 Strontium isotope signatures of travertine vs. U-series determined ages (ka). Red = Qtr3 group (>400 ka), Green = Qtr2 group (100 ka – 400 ka), Yellow = Qtr1 group (< 100 ka). Error bars not shown where uncertainty (2sigma) is less than symbol size; uncertainty decreases with younger ages. Vertical grey rectangles refer to glacial periods while white rectangles represent interglacial periods.

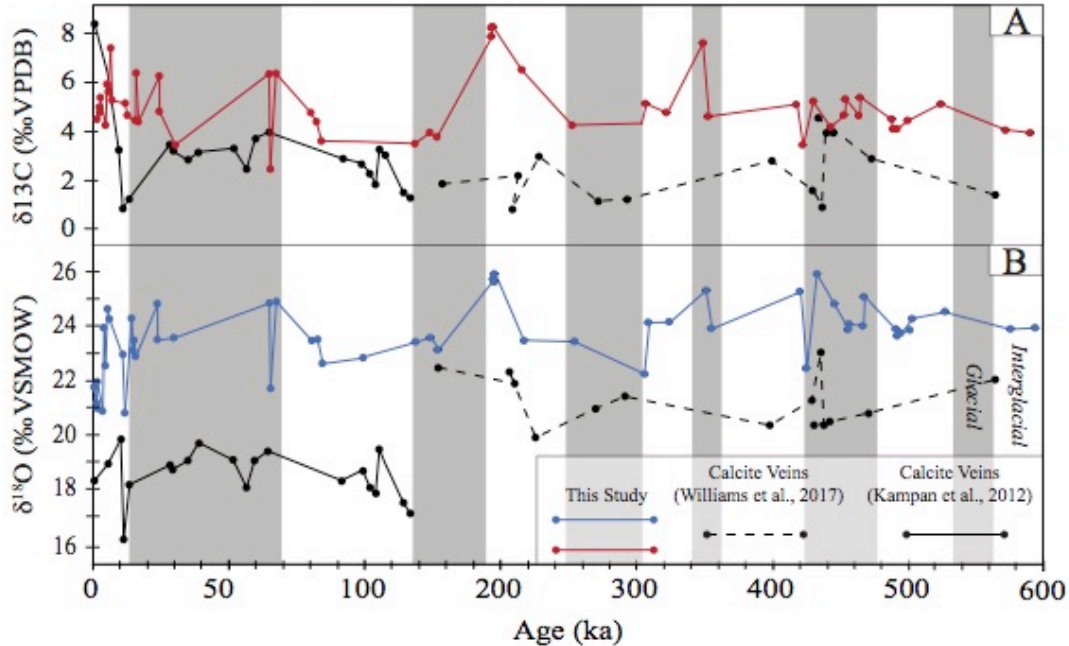


Figure 3.6 Summary of $\delta^{13}\text{C}$ (A) and $\delta^{18}\text{O}$ (B) vs. U-series determined ages (ka). Our data is compared to regional ^{13}C and ^{18}O record analyses of Kampman et al. (2012) and Williams et al. (2017), whom argue in favor of climatic influences for travertine formation (Kampman study) and against climatic influences (Williams study; attribute local tectonics). Vertical grey rectangles refer to glacial periods while white rectangles represent interglacial periods.

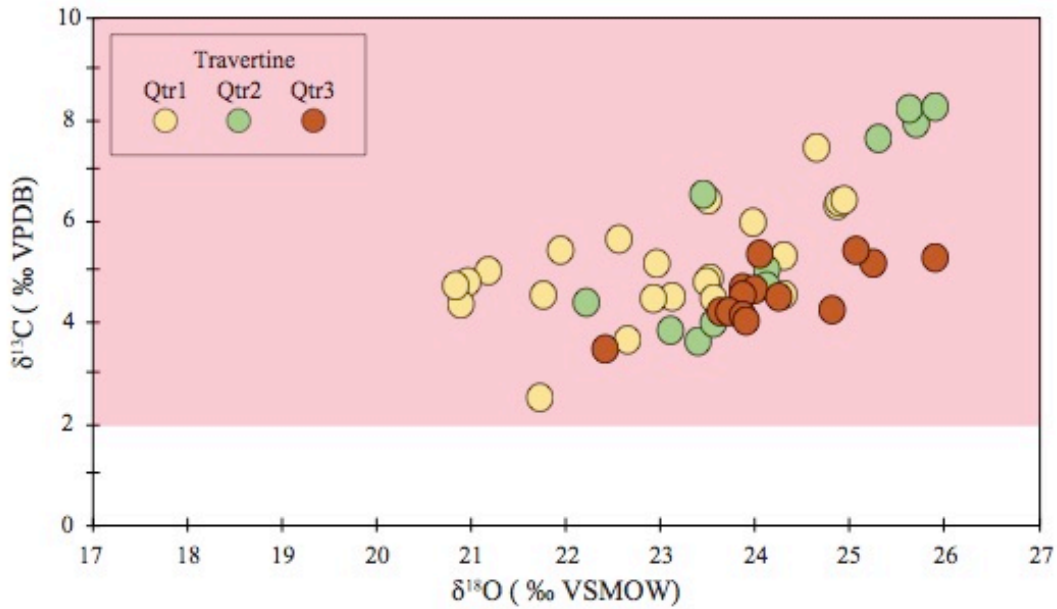


Figure 3.7 Stable carbon and oxygen isotope compositions of the three travertine groups of this study in the Lucero Uplift. Error bars not visible due to uncertainty (2sigma) being less than symbol size. Light red shaded area is range of worldwide travertine isotopic compositions associated with thermal/endogenic fluid sources.

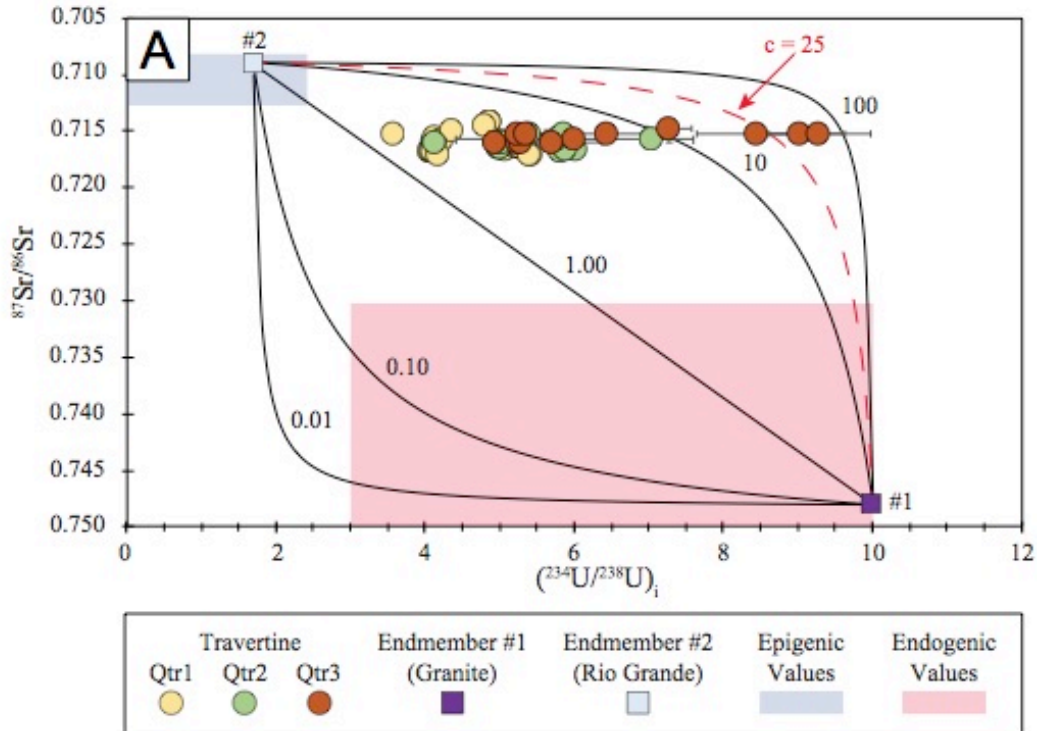
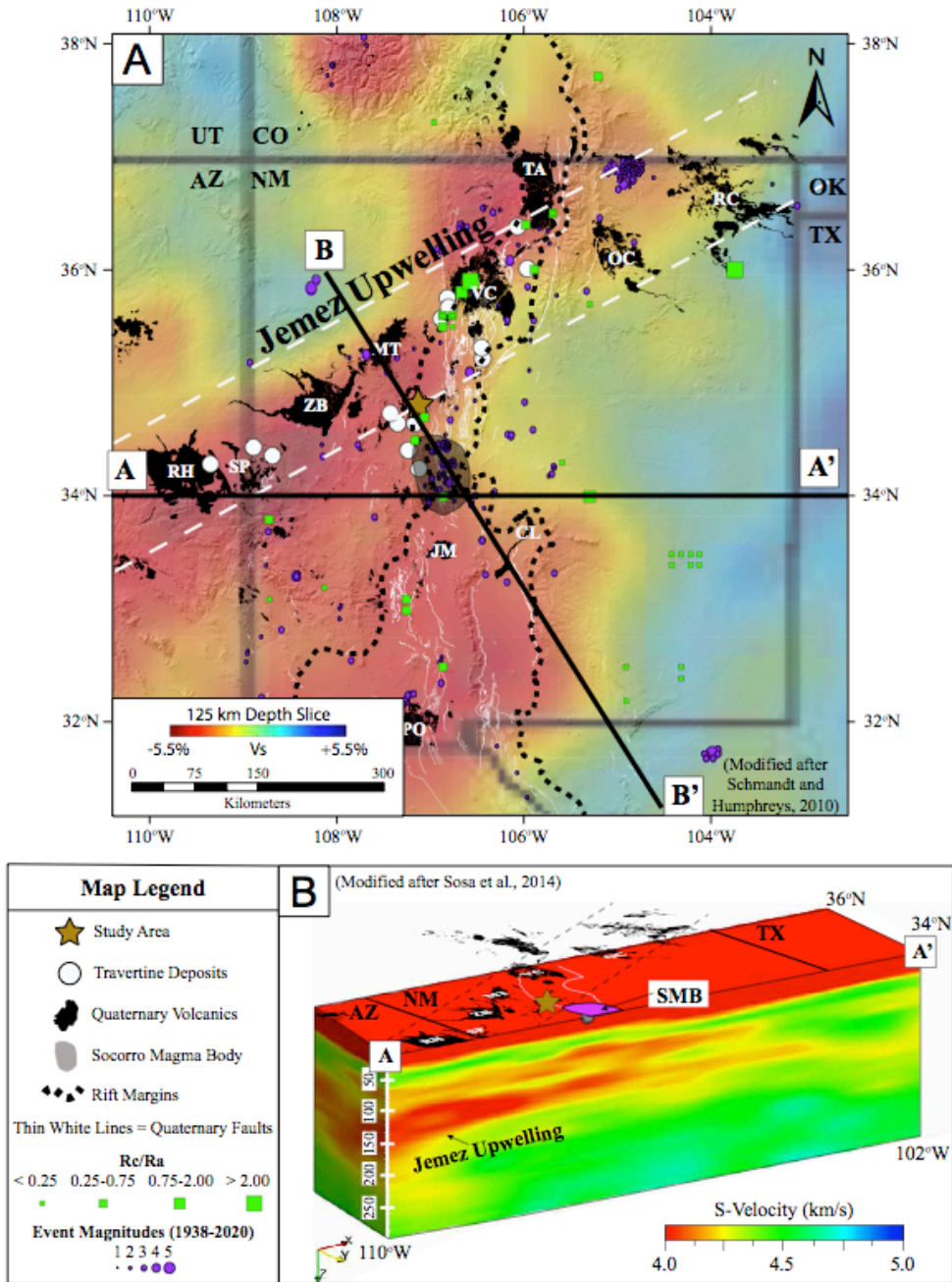


Figure 3.8 $^{87}\text{Sr}/^{86}\text{Sr}$ vs. $(^{234}\text{U}/^{238}\text{U})_i$; isotopic compositions mixing model of samples from the three travertine groups of this study showing little variation in Sr isotopic signature. Purple and light blue squares indicate endmember isotopic compositions of the Sandia Granite (purple; Brookins and Majundir (1988), Brookins and Majundir (1982), Crossey et al., 2006) and Rio Grande water sample (light blue; this study). Light red shaded rectangle is the region in which endogenic derived fluids would lie on this model. Light blue shaded rectangle is the region in which epigenic (i.e. meteoric) fluids would lie. Various mixing lines of the two endmembers (i.e. Sandia Granite and Rio Grande) are shown as solid black lines; curve is dependent on the relative elemental concentrations of each endmember. Direct mixing of the two chosen endmembers should result in a fluid mixing trajectory with a concentration ratio of 25 (red dashed line). Sandia Granite (Endmember #1): $^{87}\text{Sr}/^{86}\text{Sr} = 0.748$, $[\text{Sr}] = 220$ ppm, $(^{234}\text{U}/^{238}\text{U})_i = 10$, $[\text{U}] = 4.7$ ppm; Rio Grande (Endmember #2): $^{87}\text{Sr}/^{86}\text{Sr} = 0.709$, $[\text{Sr}] = 0.490$ ppm, $(^{234}\text{U}/^{238}\text{U})_i = 1.69$, $[\text{U}] = 0.002$ ppm.



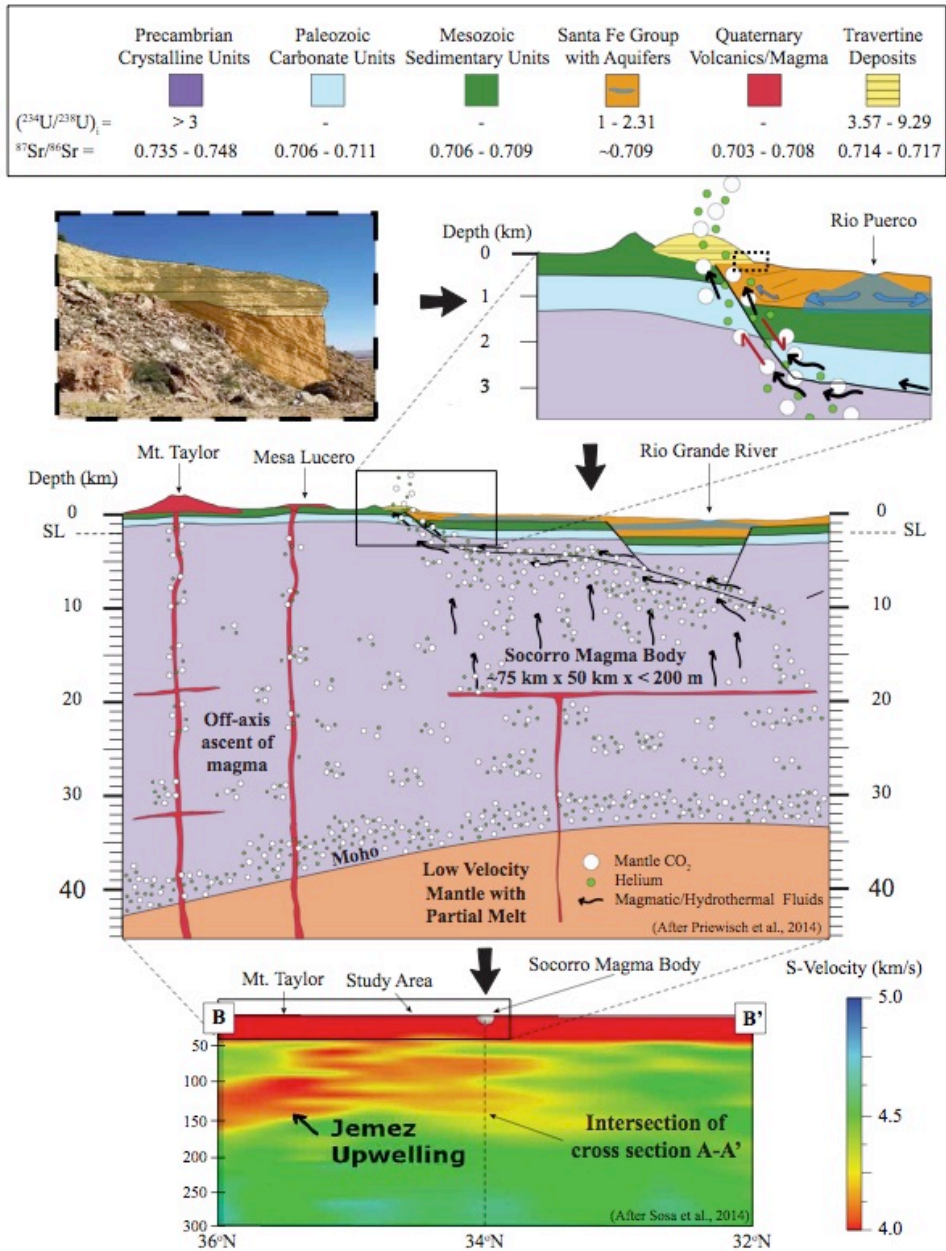


Figure 3.10 Top left: Tilted Santa Fe Group units overlaid by undeformed travertine deposits near the west bounding fault (Santa Fe fault) of the Rio Grande rift. Top right: Schematic cross section of travertine forming over the Santa Fe fault in our study area. Mantle derived gases and fluids are migrating up faults and coming in contact with different units. Middle: Conceptual model of the tectonic setting of the Rio Grande rift and Jemez Lineament after Williams et al. (2013) and Prewisch et al. (2014). The model show gases originating in the upper mantle and diffusing through the crust as well as magmatic systems. Magmatic fluids and mantle gases ascend along deep penetrating faults, like the Santa Fe fault, to the surface leading to travertine formation. Bottom: Cross section B-B' from Sosa et al. (2014) that crosses our study area. A high velocity zone underlies the Rio Grande rift, in particular in the area of the Jemez Lineament, which is termed the Jemez Upwelling.

Chapter 4: Hydrogeochemistry of travertine-precipitating springs of the Santa Fe fault zone

Victor H. Garcia¹, Lin Ma¹, and Jason W. Ricketts¹

¹*Department of Geological Sciences, The University of Texas at El Paso, 500 West University Ave. El Paso, TX. 79968*

4.1 ABSTRACT

Travertine-precipitating spring waters commonly represent the mixing of endogenic and epigenic fluids that are often associated with active fault zones of the Rio Grande rift. In this study, we present new hydrogeochemical data ($^{234}\text{U}/^{238}\text{U}$, $^{87}\text{Sr}/^{86}\text{Sr}$, and major ion chemistry) to provide perspectives on modern fluid sources contributing to surface rivers, springs and groundwaters adjacent to the Lucero Uplift (located in the Pueblo of Laguna Reservation 30 km west of Los Lunas, NM).

$^{234}\text{U}/^{238}\text{U}$ signatures of spring samples range from 2.9 ± 0.002 to 5.5 ± 0.004 . River sample $^{234}\text{U}/^{238}\text{U}$ ratios range from 1.6 ± 0.003 to 1.9 ± 0.003 . $^{87}\text{Sr}/^{86}\text{Sr}$ signatures in travertine-precipitating springs range from 0.714 ± 0.0001 to 0.717 ± 0.0001 while river samples range from 0.709 ± 0.0001 to 0.710 ± 0.0001 . The high $^{234}\text{U}/^{238}\text{U}$ and $^{87}\text{Sr}/^{86}\text{Sr}$ signatures in travertine-precipitating springs is indicative of mixing with small volumes of more radiogenic fluids derived from Precambrian basement. Mixing models show that 20% to 40% mixing between endogenic fluids with epigenic fluids is required to attain the current isotopic compositions.

Endogenic fluids have variable compositions and three geographically distinct hydrochemical facies compositions were identified with varying endogenic fluid contributions. Hydrogeochemical facies 1 (HF1) samples have a Na-Cl dominant composition, correlate with high TDS, conductivity, $^{234}\text{U}/^{238}\text{U}$, $^{87}\text{Sr}/^{86}\text{Sr}$, and are located on the Santa Fe fault zone. This group

is interpreted to reflect endogenic fluid sources that mix with epigenic fluids along their trajectory. HF3 samples have a mixed cation-anion composition, correlate with low TDS, conductivity, $^{234}\text{U}/^{238}\text{U}$, $^{87}\text{Sr}/^{86}\text{Sr}$, and are located away from major fault systems in the basin. This group is interpreted to reflect epigenic meteoric fluids that interact with alluvial aquifers in the Santa Fe group sediments. Using regional major ion data, we infer that western margin faults of the Rio Grande rift act as conduits for endogenic fluids to reach the surface.

4.2 INTRODUCTION

Fault zones in the shallow crust play an important role in a wide range of fluid-related geological processes such as seismic activity, mineral deposition, hydrocarbon migration, and govern paleo and modern fluid storage and fluid flow patterns (Deming, 1992; Fossen et al., 2010; Barton et al., 1995). Deformation associated with fault zones is recognized to be a critical element in the augmentation of permeability in the Earth's crust (Claesson et al., 2007). With increased permeability, faults are capable of acting as conduits for fluid and gas migration along fault zones (Johnson et al., 2013).

In the Rio Grande rift, where extension and crustal thinning are currently ongoing, it is hypothesized that deep basement penetrating faults facilitate the mixing of endogenic (deeply derived) fluids with epigenic (shallow meteoric) fluids (Newell et al., 2005; Crossey et al., 2009, Williams et al., 2013; Williams et al., 2018). In particular, studies have focused mainly on travertine-precipitating springs located along the western margin of the Rio Grande rift near the Socorro magma body (SMB) and Valles Caldera using mantle He and CO_2 , major ion chemistry, and $^{87}\text{Sr}/^{86}\text{Sr}$ methods (Crossey et al., 2009; Williams et al., 2013; McGibbon et al., 2018; Blomgren et al., 2019). Travertine-precipitating spring waters commonly represent the mixing of endogenic and epigenic fluids that are often associated with active fault zones, high geothermal

gradients, young magmatic systems, and in some cases are underlain by low mantle velocity zones (Crossey et al., 2009; Crossey et al., 2015).

In this study, we focus on travertine-precipitating springs associated with the Sant Fe fault system along the boundary of the Colorado Plateau and Rio Grande rift at the Lucero Uplift (Fig. 1) (~30 km west of Los Lunas, New Mexico). This location is of particular interest because it is located ~40 km north of the SMB boundary, ~100 km south of Valles Caldera, and there is evidence of recent volcanic activity (i.e. Suwanee basalt flow 0.32 ± 0.2 Ma; Bachman and Mehnert, 1978). The goal of this study is to assess the modern source of travertine-precipitating springs along the Santa Fe fault zone (i.e. endogenic, epigenic, or mixing of both) utilizing $^{238}\text{U}/^{234}\text{U}$, $^{87}\text{Sr}/^{86}\text{Sr}$, and major ion analyses. Additionally, we compare our data with regional spring and groundwater data to examine the influence fault zones, the SMB, and Valles Caldera have on fluid sources and fluid transport in the region. We find that travertine-precipitating springs in our study area contain endogenic signatures, which are influenced by the Jemez Lineament.

4.3 BACKGROUND

4.3.1 Geologic Setting

The Rio Grande rift is a zone of active continental extension which began rifting 30-32 Ma, and is defined by a thin crust underlain by low mantle velocities (Baldrige et al., 1984; Morgan et al., 1986; Schmandt and Humphreys, 2010). Regionally, the rift is composed of a series of north-south trending half graben bounded by major faults that extend from Colorado and continue into Mexico (Chapin, 1979). This extension has resulted in a complex network of fault zones that greatly influence modern fluid flow and storage (Figure 1). These fault systems offer an excellent opportunity to investigate modern fluid sources and hydrogeochemistry in northern and central New Mexico.

Travertine-precipitating springs in New Mexico generally occur within rift basins and along the western margin of the Rio Grande rift. Additionally, this region of the Rio Grande rift contains abundant evidence for persistent magmatic influences. In northern New Mexico, the Rio Grande rift is intersected by the Jemez Lineament (Figure 1), a northeast-southwest trending series of volcanic fields that consist of basaltic to rhyolitic rocks ranging in age from ~16 to 0.13 Ma (Dunbar, 2005; Zimmerer et al., 2016). Valles Caldera is located at the intersection of the Jemez Lineament and western margin of the Rio Grande rift (Goff and Shevenell, 1987). In central New Mexico, the Rio Grande rift is underlain by the SMB, a thin~20 km deep mid-crustal magma sheet (Reiter et al., 2010).

The associations between magmatic and tectonic activity in the Rio Grande rift are believed to provide 1) a source for mantle-derived CO₂ and ³He observed in springs along these intersects and 2) the deep penetrating faults that act as the conduits necessary for endogenic fluids to reach the surface (Figure 2; Newell et al., 2005; Williams et al., 2013; Priewisch et al., 2014).

4.3.2 Study Area Geology

The Lucero Uplift is a wide region of gently west dipping undeformed Paleozoic to Mesozoic rocks of the Colorado Plateau (Duschatko, 1953). To the east, the Lucero Uplift transitions into the boundary between the Colorado Plateau and the Rio Grande rift in central New Mexico. This boundary is a narrow (~500-m-wide) north-south trending fault zone consisting of steeply dipping Paleozoic to Cenozoic units (Callender and Zilinski, 1976). This fault zone consists of two major fault systems that separate relatively undeformed Paleozoic and Mesozoic units of the Colorado Plateau to the west from Cenozoic Santa Fe rift fill units to the east (May and Russel, 1994; Ricketts and Karlstrom, 2014). These main faults include the west-dipping reverse-sense

Comanche fault, that is likely Laramide in origin, and the east-dipping normal-sense Santa Fe fault that formed during development of the Rio Grande rift.

Active travertine-precipitating springs are present along a 30 km trace of the Lucero Uplift in our study area (Figure 3). Travertine-precipitating springs likely emanate from the Santa Fe fault system (Ricketts and Karlstrom, 2014). The presence of large 10-m thick travertine deposits and available U-series dates suggest that travertine-precipitating springs have been active in the area since at least ~500 ka (Ricketts et al. 2014; Chapter 3, this dissertation). Many large-volume travertine deposits are currently inactive, although active springs include a spring surrounded by a large travertine mound (Fig. 3B), many smaller active springs found in arroyos of the study area and at lower elevations along the basin floor. Some large travertine deposits (Fig. 3C and 3D) in the area are cut by younger travertine deposits with dam and pool structures filled with spring waters. Recent work on travertine-precipitating springs and travertine deposits near our study area indicate that source fluids are a mixture of endogenic and epigenic fluids (Crossey et al., 2011; Priewisch et al., 2014; Williams et al., 2013; Williams et al., 2015).

4.3.3 Uranium-series Isotopes

Uranium-series disequilibrium (U-series) has proven to be a successful tracer in hydrogeochemical investigations (Kronfeld et al., 1975; Ivanovich and Harmon, 1992; Chabaux et al., 2003). Most fluids usually have high ($^{234}\text{U}/^{238}\text{U}$) ratios greater than 1 due to the high solubility of U in oxidizing environments and preferential leaching of ^{234}U over ^{238}U into weathering fluids (Kronfeld et al., 1975; Fleisher, 1980; Anderson et al., 2009). This makes ($^{234}\text{U}/^{238}\text{U}$) ratios an ideal tracer to distinguish between shallow fluid sources, which typically have ($^{234}\text{U}/^{238}\text{U}$) less than 3, and deep fluid sources, which have much higher ($^{234}\text{U}/^{238}\text{U}$) values (Chabaux et al., 2003; Durand et al., 2005).

4.3.4 Strontium Isotopes

$^{87}\text{Sr}/^{86}\text{Sr}$ ratios can be used to differentiate between different lithologies because of the long-term evolution of Sr ratios over time due to Rb/Sr fractionation (Bullen et al., 1996). For example, granitic intrusive units tend to have higher $^{87}\text{Sr}/^{86}\text{Sr}$ ratios due to high Rb/Sr ratios and Sr being released into fluid systems naturally through the weathering of geologic materials and lack of fractionation by weathering (Pett-Ridge et al., 2009, Paces and Wurster, 2014; Crossey et al., 2015; Zielinski et al., 2016). This makes $^{87}\text{Sr}/^{86}\text{Sr}$ ratios useful in hydrogeochemical studies. This method is particularly useful in distinguishing between sedimentary units where isotopic compositions tend to be buffered by seawater ratios ($^{87}\text{Sr}/^{86}\text{Sr}$ ratios ~ 0.710) vs Precambrian granitic bedrock where long-term Rb decay leads to high Sr ratios ($^{87}\text{Sr}/^{86}\text{Sr}$ ratios ~ 0.735). This distinction is important in this study because shallow environments are dominated by sedimentary rocks vs deeper, Precambrian basement sources (Clark and Fritz, 1997; Pett-Ridge et al., 2009), which makes Sr isotopes ideal tracers to distinguish between epigenic and endogenic fluid sources.

4.4 METHODS

4.4.1 Sample Selection

A total of thirteen travertine-precipitating spring samples were collected along a 10 km trace of the Lucero Uplift (Table 1). In the northern section of our study area, we collected five spring samples from low and high elevation areas along minor faults of the Santa Fe fault zone (Figure 3). One spring sample was collected from travertine pool and dam structures in the central portion of our study area where the main Santa Fe fault is mostly overlain by a thick travertine deposit (Fig. 3C). The other seven spring samples were collected from the southern section of our study area in arroyos and active travertine deposits that overlie the main exposure of the Santa Fe fault. In addition, two river samples were collected at the intersection the Rio Puerco with NM

Highway 6 (Fig. 3E), one sample from the Rio Grande in Los Lunas, NM, one river sample near the Rio Puerco and NM Highway 60, and one river sample near La Joya, NM close to the confluence of the Rio Puerco and Rio Grande (Fig. 1).

Spring and river samples were analyzed at the Center for Earth and Environmental Isotope Research at the University of Texas at El Paso for $^{87}\text{Sr}/^{86}\text{Sr}$ ratios, $^{234}\text{U}/^{238}\text{U}$ ratios, and major ions. In the lab, 400 mL of sample were filtered using a $0.45\mu\text{m}$ cellulose acetate filter to remove sediment and particulates and placed in two 250 mL acid washed high density polyethylene Nalgene bottles. One bottle was acidified with 3 drops of concentrated nitric acid for future cation and isotope analysis and the other bottle was archived without acidification for immediate anion analysis.

4.4.2 U-series Analysis

For each sample, ~60 mL of water were evaporated overnight at 90°C and re-dissolved in 1 mL 7.5 N HNO_3 . Samples were separated and purified for U using ion chromatography procedures similar to Chabaux et al., (1995). Samples, which were previously dissolved in 1 mL of 7.5N HNO_3 , were loaded into columns containing AG 1-X8 anion exchange resin (200-400 mesh), which had previously been washed with 6 N HCl and 0.25 HNO_3 , rinsed with $18\text{M}\Omega$ water, and conditioned with 7.5 N HNO_3 . After sample introduction, samples were eluted with 7.5 N HNO_3 . U was collected in 15 mL Teflon beakers in a series of steps using $18\text{M}\Omega$ water, 0.5 N HCl and 6 N HCl . Samples were evaporated overnight and redissolved in 0.2 mL of 6 N HCl . U was then purified using columns containing 0.6 mL AG1-X8 200-400 mesh resin which were washed in the same method as the previous columns and conditioned with 6 N HCl . After sample introduction, we used a series of elutions using 6 N HCl and acetone + 6 N HCl . U was collected with 0.5 N HCl and evaporated overnight. Samples were then analyzed on MC-ICP-MS to obtain

$^{234}\text{U}/^{238}\text{U}$ ratios using the uranium standard (NBL145B) for standard bracketing method to correct for mass fractionation and ion counter gains for U measurements. We calculated $^{234}\text{U}/^{238}\text{U}$ activity ratios using decay half-lives of ^{234}U and ^{238}U . Uranium concentrations were calculated from weight and concentrations of the spike as well as ion counter gain and mass fractionation corrected $^{233}\text{U}/^{238}\text{U}$ isotope ratios.

For accuracy purposes, about 200 mg of the USGS rock standard BCR-2 rock standard was spiked with ^{233}U reference material and digested in HNO_3 -HF then followed by HCl - H_3BO_3 to dissolve all silicates and fluorides in the samples (Pelt et al., 2008; Granet et al., 2007; Dequincey et al., 2002). The BCR2 standard showed a value of $^{234}\text{U}/^{238}\text{U} = 1.004 \pm 0.0045$ (2σ ; $n=2$) consistent with those reported by Sims et al., (2008).

4.4.3 Strontium Isotopes

Samples were processed in batches of 16, which included one Columbia River Basalt (BCR-2) standard reference material and one blank. To separate Sr from the sample matrix for isotope ratio analysis, Sr column chemistry was carried out for a select number of samples following the technique of Konter and Storm (2014) with Eichrom® Sr-resin. The samples were first dried by pouring ~7.5 mL of acidified water sample into 15-mL Teflon beakers and left in a hot plate overnight at 90°C . Columns were cleaned with 6 N HNO_3 and rinsed with DI Water. They were then filled with Eichrom® Sr-resin and cleaned with ultrapure water then conditioned with 3.5 N HNO_3 . The samples were re-dissolved in 0.5 mL 3.5 N HNO_3 and loaded onto the column. The matrix was eluted in a series of steps by adding different amounts of 3.5 N HNO_3 . Sr was collected in clean 15-mL Teflon beakers by adding 0.05 N HNO_3 to the columns. Isotopic ratios of $^{87}\text{Sr}/^{86}\text{Sr}$ were measured using a Nu Plasma MC-ICP-MS using the standard sample bracketing method with the strontium standard NIST SRM 987. The USGS rock standard BCR-2

was measured to assess accuracy of our measurements. The measured $^{87}\text{Sr}/^{86}\text{Sr}$ isotope ratios for BCR2 were $^{87}\text{Sr}/^{86}\text{Sr} = 0.70503 \pm 0.0001$ (2σ ; $n=2$). Our results are consistent with the accepted reference values of $^{87}\text{Sr}/^{86}\text{Sr}$ ratio of BCR-2 is 0.70502 ± 0.00001 (2σ) (Jweda et al., 2015).

4.4.4 Major Ions

For major cation concentrations, ~15-mL of acidified sample was analyzed on a Perkin Elmer 5300DV Optical Emission Spectrometer (OES). The standards USGS M-210 and NIST 1640a were analyzed between 3-5 times during each run to assess measurement precision. Percent error of the standards was no greater than 10% on all major elemental concentrations. For major anion concentrations, the non-acidified filtered sample was diluted with DI water by approximately ten times (i.e. 10 mL of DI water for every 1 mL of sample). The accurate dilution factor for each sample was calculated with sample weights. These samples were analyzed using a Dionex ICS-2100. An in-house water standard was measured at least twice during each run to ensure accuracy. Standard errors in general were no greater than 12%.

4.5 RESULTS

4.5.1 U-series Ratios

U-series data is summarized in Table 2 and Figure 4. Analyzed travertine-precipitating springs samples have U concentrations ranging from 11–23 ppb and $^{234}\text{U}/^{238}\text{U}$ ratios of 2.9 ± 0.002 to 5.5 ± 0.004 . River sample U concentrations range from 2–8 ppb and $^{234}\text{U}/^{238}\text{U}$ ratios range from 1.6 ± 0.003 to 1.9 ± 0.003 . Spatially, there is no relationship between $^{234}\text{U}/^{238}\text{U}$ ratios and their locations.

4.5.2 Strontium Isotopes

Strontium isotope data are summarized in Table 2 and Figure 5. Analyzed travertine-precipitating spring samples have Sr concentrations ranging from 4.5–12.5 ppm and $^{87}\text{Sr}/^{86}\text{Sr}$ ratios

ranging from 0.714 ± 0.0001 to 0.717 ± 0.0001 . River sample Sr concentrations range from 0.5–3.2 ppm and have $^{87}\text{Sr}/^{86}\text{Sr}$ ratios ranging from 0.709 ± 0.0001 to 0.710 ± 0.0001 . Similar to U-series data, $^{87}\text{Sr}/^{86}\text{Sr}$ ratios have no spatial relationships with location.

4.5.3 Major Ions

Major ion elemental chemistry is reported in Table 3 and in Figure 6. Total dissolved solids (TDS) in spring samples ranged from 25,346–34,629 ppm. The three samples collected from the Rio Puerco had very similar TDS with an average of 1,267 ppm. The two Rio Grande samples had the lowest TDS of 445 ppm and 763 ppm. The major dissolved ion concentrations (all in ppm) for spring samples are as follows: Ca (157-667), Mg (104-207), Na (6809-10626), K (164-294), HCO_3^- (5176-12140), SO_4 (3935-7969), and Cl (4405-11881). The major dissolved ion concentrations (all in ppm) for Rio Puerco samples are as follows: Ca (104-105), Mg (24-26), Na (162-167), K (4-5), HCO_3^- (435-562), SO_4 (408-496), and Cl (37-50). The major dissolved ion concentrations (all in ppm) for Rio Grande samples are as follows: Ca (34-68), Mg (7-7), Na (42-91), K (3-4), HCO_3^- (285-352), SO_4 (58-204), and Cl (22-45).

Hydrogeochemical facies were determined using field parameters, local geology, and major ion chemistry. Two distinct hydrogeochemical facies (HF) are observed on a Piper diagram of our data (Figure 6) that correspond with their geographic locations. HF1 consists of fault zone collected spring samples, which are a dominant Na-Cl group (Figure 6 red circles). HF3 consists of five river samples collected within the Albuquerque basin, away from major faults, and contain noticeably less Na-Cl but higher amounts of Ca and SO_4 compared to HF1 (Figure 6 blue circles).

4.6 DISCUSSION

4.6.1 U Isotope Sources and Implications

Initial fluid $^{234}\text{U}/^{238}\text{U}$ activity ratios reflect the amount of ^{234}U present in fluids relative to the $^{234}\text{U}/^{238}\text{U}$ activity ratio at secular equilibrium. Excess initial ^{234}U (i.e. $^{234}\text{U}/^{238}\text{U} > 1$) indicate prolonged contact between fluids and U-rich lithologies, which enhances the transfer of alpha recoiled ^{234}U into U depleted fluids (Kronfeld et al., 1975; 1994). Because of this, endogenic fluids typically exhibit higher concentrations of U and higher $^{234}\text{U}/^{238}\text{U}$ ratios than epigenic fluids (Chabaux et al., 2003).

Meteoric fluids (i.e. epigenic fluids) of the Rio Grande typically have $^{234}\text{U}/^{238}\text{U}$ ratios equal to ~ 2 (Nyachoti, 2016; Garcia, 2017). This is confirmed by river samples collected in this study, which have $^{234}\text{U}/^{238}\text{U}$ ratios < 2 from two different rivers at four separate locations. However, there is a slight difference in $^{234}\text{U}/^{238}\text{U}$ ratios between the Rio Puerco and Rio Grande. The Rio Puerco has slightly higher $^{234}\text{U}/^{238}\text{U}$ ratios (average = 1.89; n = 3) than the Rio Grande (average = 1.70; n = 2). This difference is likely due to the larger volume of water present in the Rio Grande, which dilutes higher $^{234}\text{U}/^{238}\text{U}$ signatures, compared to the water-limited Rio Puerco.

In contrast, $^{234}\text{U}/^{238}\text{U}$ signatures of travertine-precipitating springs range from 2.97 to 5.41 with an average $^{234}\text{U}/^{238}\text{U}$ value of 3.80; indicative of endogenic sources. It is likely that these signatures are assimilated from Paleozoic, Mesozoic, or Cenozoic units found in the foot wall and hanging wall of the Santa Fe fault system or are derived from a deeper endogenic source (i.e. magmatic or crystalline basement). Limestone units, which are common in Paleozoic and Mesozoic units in our study area, typically have moderate U concentrations (~ 5 ppm) and low $^{234}\text{U}/^{238}\text{U}$ ratios of $\sim 1 - 2$ (Deschamps et al., 2004). Alternatively, Cenozoic units such as magmatic materials (e.g. basalts) are depleted in U and have low $^{234}\text{U}/^{238}\text{U}$ values (Williams et al., 2018)

while rift related sediments have $^{234}\text{U}/^{238}\text{U}$ signatures similar to groundwater and river values between 1.35 – 2.65. Latter value from Truth or Consequences, NM where geothermal waters are prominent (Szynkiewicz et al., 2015). All of the previously mentioned $^{234}\text{U}/^{238}\text{U}$ values are much lower than the relatively high $^{234}\text{U}/^{238}\text{U}$ observed in our spring samples.

We infer the higher $^{234}\text{U}/^{238}\text{U}$ values in our spring samples to represent endogenic fluids, which were in contact with U-bearing Precambrian crystalline basement. This is supported by anomalously high $^{234}\text{U}/^{238}\text{U}$ signatures observed in travertine deposits of our study area, which range from 3.6 to 9.3 and get lower $^{234}\text{U}/^{238}\text{U}$ values with younger travertine ages (Chapter 3, this dissertation).

4.6.2 $^{87}\text{Sr}/^{86}\text{Sr}$ Sources and Implications

In our study, travertine-precipitating springs show Sr isotopes ranging from 0.714 to 0.717 and correlate with fluids that have undergone deep circulation through Precambrian basement (Figure 6). This range of $^{87}\text{Sr}/^{86}\text{Sr}$ signatures in our spring samples is within range other travertine-precipitating springs and travertine deposits near our study area of 0.711 to 0.734 (Goff et al., 1983; Crossey, 2006; Williams et al., 2013; Priewisch et al., 2014; Williams et al., 2015). The highest $^{87}\text{Sr}/^{86}\text{Sr}$ values are commonly associated with Proterozoic granitic basement, which range from 0.735-0.748 (Taggart and Brookins, 1975; Goff and Gardner, 1994; Crossey et al., 2006; Williams et al., 2015).

In our study area, it is expected that fluids migrating to the surface along the Santa Fe fault zone interact with various Paleozoic limestone ($^{87}\text{Sr}/^{86}\text{Sr} = 0.706 - 0.711$) and Mesozoic limestone units ($^{87}\text{Sr}/^{86}\text{Sr} = 0.706-0.709$) (Mukhopadhyay and Brookins, 1976; Burke et al., 1982; Kirkland et al., 1995; McArther et al., 2001; Young and Chan, 2017) . If modern spring fluids do indeed originate from highly radiogenic basement rock, then the water-rock interaction between those

fluids and limestone units may account for the reduced $^{87}\text{Sr}/^{86}\text{Sr}$ signatures observed in our travertine-precipitating springs. Additionally, mixing with waters passing through other lithologic types and/or meteoric fluids along fault flow paths could also account for the low $^{87}\text{Sr}/^{86}\text{Sr}$ signatures observed. For example, basalts in our region typically have $^{87}\text{Sr}/^{86}\text{Sr}$ signatures of 0.703-0.708 (Allen and Foord, 1991; Johnson and Thompson, 1991; McMillan et al., 2000) while rivers in the Rio Grande rift have $^{87}\text{Sr}/^{86}\text{Sr}$ values of \sim 0.709 (Hogan et al., 2007; Garcia, 2017).

We interpret the moderately high $^{87}\text{Sr}/^{86}\text{Sr}$ signatures of our travertine-precipitating springs as being indicative of water-rock interaction with highly radiogenic Precambrian crystalline basement (e.g. Sandia Granite), which have $^{87}\text{Sr}/^{86}\text{Sr}$ signatures of 0.748 (Williams et al., 2018). This hypothesis is supported by similarly high ($^{234}\text{U}/^{238}\text{U}$)_i values in our spring samples. Fluid mixing calculations (Crossey et al., 2006; McGibbon et al., 2018; Williams et al., 2018) suggest that fluids with moderate $^{87}\text{Sr}/^{86}\text{Sr}$ signatures (i.e. \sim 0.714-0.720) are attainable with mixing of approximately 1-20% of highly radiogenic endogenic fluids with low non-radiogenic epigenic fluids.

We infer that deeply sourced fluids initially acquire the signature of the highly radiogenic basement materials, ascend along deep basement penetrating faults and into Paleozoic/Mesozoic carbonates (0.706-0.711), and further mix with shallow meteoric fluids (\sim 0.709) near the surface to reach their current $^{87}\text{Sr}/^{86}\text{Sr}$ isotopic values (Figure 7).

4.6.3 $^{234}\text{U}/^{238}\text{U}$ vs $^{87}\text{Sr}/^{86}\text{Sr}$ Mixing Model

A mixing model of endogenic/radiogenic $^{234}\text{U}/^{238}\text{U}$ and $^{87}\text{Sr}/^{86}\text{Sr}$ versus epigenic/non-radiogenic $^{234}\text{U}/^{238}\text{U}$ and $^{87}\text{Sr}/^{86}\text{Sr}$ endmembers can clarify the sources and likely flow paths of fluids in the Santa Fe fault zone. Using the equation derived by Vollmer (1976), we selected three endmembers that are likely to be encountered by fluids in our study area: 1) Precambrian

crystalline basement with high isotopic signatures, 2) shallow fluids with similar isotopic signatures to the Rio Grande, and 3) Precambrian crystalline basement with lower isotopic signatures (Figure 8).

In Figure 8, $^{87}\text{Sr}/^{86}\text{Sr}$ vs. $(^{234}\text{U}/^{238}\text{U})_i$ data are plotted for our river samples (varying shades of blue circles), spring samples (red circles), and our three selected endmembers (squares). Additionally, $^{87}\text{Sr}/^{86}\text{Sr}$ and $(^{234}\text{U}/^{238}\text{U})_i$ compositions for travertine deposits in the study area are also plotted (Garcia et al., in prep). Figure 8A, shows multiple mixing lines between endmember #1 (highly radiogenic Precambrian crystalline basement; purple square) and endmember #2 (low radiogenic Rio Grande signatures; light blue square). Mixing between these two endmembers, would result in a concentration ratio of 25 ($c = (\text{Sr}_1 \times \text{U}_2) / (\text{Sr}_2 \times \text{U}_1)$) and would have a mixing curve (dashed grey line) as shown on Figure 8A. None of the river or spring samples plot near this line, indicating a possible different fluid path. However, two travertine samples lie within range of the direct mixing curve of these two endmembers.

Figure 8A also shows two mixing lines between endmember #2 (low radiogenic Rio Grande signatures; light blue square) and endmember #3 (Precambrian crystalline basement with lower isotopic signatures; lilac square). In this scenario, the only difference is a lower $^{87}\text{Sr}/^{86}\text{Sr}$ signature in the Precambrian crystalline basement, which are possible. Direct mixing between these endmembers would result in a similar concentration ratio of 25 (Figure 8A) to that of mixing between endmember #1 and #2.

Figure 8B, represents only mixing lines between endmember #2 and #3. In this scenario, the best fit mixing line has a concentration ratio of 0.60 (dashed lilac line) with the spring data fitting between concentration ratios of 0.45 and 2 (dashed black lines). In these cases, it is apparent that mixing of a small volume of endogenic fluids (derived from Precambrian crystalline basement;

$^{87}\text{Sr}/^{86}\text{Sr} = 0.748$; $^{234}\text{U}/^{238}\text{U} = 5$) and a larger volume of epigenic fluids (derived from shallow aquifers; $^{87}\text{Sr}/^{86}\text{Sr} = 0.709$; $^{234}\text{U}/^{238}\text{U} = 1.70$). This mixing model demonstrates that the travertine-precipitating spring signatures can be explained by a mixing of varying volumes of endogenically derived fluids with epigenic fluids. Additionally, the mixing models confirm that there must be some endogenic input.

4.6.4 Major Ion Chemistry

A Piper diagram (Fig. 6) was used to highlight major ion variations and similarities between the different samples groups. It is possible to establish potential fluid sources and paths by identifying hydrogeochemical characteristics of each sample group. In this section, we highlight the differences in our data and compare it to regional major ion studies.

The two hydrogeochemical facies (HF) can be defined by their endmember compositions (Figure 6). HF1, consisting of the travertine-precipitating spring samples, comprises a Na-Cl dominant composition. HF1 samples correlate with high TDS, conductivity, $^{234}\text{U}/^{238}\text{U}$, $^{87}\text{Sr}/^{86}\text{Sr}$, and are located along the Santa Fe fault zone. This group is interpreted to reflect endogenic fluid sources that mix with epigenic fluids along their trajectory. Samples PLTS02 and PLTS05 contain less Cl and plot slightly different than the other spring samples. They are located near other spring samples, which have slightly higher Cl concentrations. We attribute less evaporation or more dilution with meteoric fluids in samples PLTS02 and PLTS05 to explain the minor difference observed in Cl.

HF3, consisting of various river samples from the Rio Puerco and Rio Grande, comprises a mixed cation/anion composition corresponding with local meteoric chemistry consistent with other river compositions. HF3 samples correlate with low TDS, conductivity, $^{234}\text{U}/^{238}\text{U}$, $^{87}\text{Sr}/^{86}\text{Sr}$, and are located away from major fault systems in the basin. This group is interpreted to reflect

epigenic meteoric fluids that interact with alluvial aquifers in the Santa Fe group sediments. River sample RG01 plots slightly lower than the other rivers samples due to lower Cl, SO₄⁻, and higher HCO₃ relative to the other samples. This sample from the Rio Grande is located near Los Lunas, NM and represents river samples with less SO₄⁻ input compared to the Rio Puerco samples and to the Rio Grande sample after the confluence of both river systems.

4.6.5 Regional Implications

Studies of travertine-precipitating springs in New Mexico have not, to date, ²³⁴U/²³⁸U signatures. However, most travertine studies do include ²³⁴U/²³⁸U initial ratios (3.5 to 9.3), which imply that travertine deposits, and thus, travertine-precipitating springs, must have an endogenic component. Similarly, ⁸⁷Sr/⁸⁶Sr from other studies in the region and from our travertine data (0.711 to 0.734) reported here indicate an endogenic source.

Regional major ion water data were compiled to show the spatial distribution of four hydrogeochemical facies within basins of the Rio Grande in Figure 9 and 10. The data reported here are from Goff and Shevenell, (1987), Bexfield and Plummer (2003), Crossey et al., (2011), Williams et al., (2013), Johnson et al., (2013), McGibbon et al., (2018), and Blomgren et al., (2019). In Figure 9, data points are color coded according to which hydrogeochemical facies (HF) they plot on Figure 10 (e.g. small red circles indicate HF1-endogenic source, small black circles are HF2-volcanic source, small blue circles are HF3-meteoric, and small green circles are HF4-sedimentary source). In Figure 10, data points are also color coded based on the facies they plot in. The different shapes refer to which basin they are located in (e.g. open diamonds = San Luis Basin, open circle = Española Basin, open square = Socorro Basin, open triangle = Albuquerque Basin) and other water samples located through the different basins (e.g. half red circle = Rio Salado, turquoise circles = Rio Grande, open stars = Lucero Uplift springs). River and Spring

samples from this study are also plotted on each Piper Diagram as larger faded blue and red circles. Additionally, data from travertine-precipitating springs are also used for comparison to our data.

Samples that fall under HF1 (i.e. endogenic source) tend to be located on the western margin of the Rio Grande rift near the Socorro Magma Body and the Lucero Uplift (location of this study; Figure 9). In the Albuquerque Basin, HF1 samples cluster near intra-rift faults near the western margin of the Rio Grande rift. In contrast, HF2 (i.e. volcanic source mixed Na-K-HCO₃-CO₃) are dominantly located on the western margin of the Española Basin (Figure 9). In particular, the Española basin samples are located in the transition from Valles Caldera to the Española Basin. HF3-meteoric source samples are mostly river and shallow groundwater well samples located within the rift basins (i.e. Española, Albuquerque, and Socorro basins). In the Albuquerque Basin, however, many meteoric samples are located near intra-rift faults closer to the eastern margin of the Rio Grande rift. HF4 (i.e. sedimentary source; Ca-SO₄) are mainly found within the Albuquerque Basin and eastern margin of the Socorro Basin, implying local carbonate and gypsum sources.

Data from Valles Caldera also fit into 4 distinct hydrogeochemical facies (Figure 10). HF1 (i.e. endogenic samples) are generally geothermal well data from within the caldera though some samples are from the endogenically influenced Jemez River springs near Soda Dam (location of fault). HF2 (i.e. volcanic source mixed Na-K-HCO₃-CO₃) samples clearly demonstrate the influence of surficial and underlying volcanic units associated with Valles Caldera (Figure 9). HF3-meteoric samples are from small “springs” with high meteoric input within the caldera. These springs drain into the main Jemez River, which has a mix of HF2 and HF3 samples at its head waters.

Travertine-precipitating springs in the Rio Grande rift are very similar to our spring samples (Figure 9 and 10) with the exception of springs located near La Madera and Ojo Caliente, NM (purple circles). These springs likely have a meteoric influence, which would explain why they plot so differently from the rest of the travertine-precipitating spring samples in the Rio Grande rift. The main difference between our spring samples and other spring samples is less influence from gypsum bearing units, which produce elevated Ca and SO₄ as is the case in Tierra Amarilla (yellow X) and Peñasco Springs (green triangles). In contrast, Soda Dam travertine fluids contain the least amount of SO₄ but slightly more Ca. This is likely due to the lack of SO₄ bearing units in the area. The Ca is likely derived from travertine deposits that are actively being dissolved or originates from underlying carbonate units.

We conclude that endogenic flow paths are persistent along the western margin of the Rio Grande rift. This is supported by anomalously high ³He/⁴He ratios in travertine spring studies, which indicate mantle origins, along the western margin of the Rio Grande rift (Figure 9). Travertine-precipitating springs from our study area are likely a mixture of endogenic fluids and epigenic shallow basin fluids that interact along the western rift margin (see Figure 2). U, Sr, and major ion chemistry demonstrate that fluids migrate along fault conduits that extend into the Precambrian basement.

4.7 SUMMARY AND CONCLUSIONS

In this study, we applied ²³⁴U/²³⁸U, ⁸⁷Sr/⁸⁶Sr, and major ion geochemical tracers to travertine-precipitating springs from the Santa Fe fault zone at the Lucero Uplift and various river samples from the Rio Puerco and Rio Grande. We then compared our data to regional Rio Grande rift hydrogeochemical data. The range of travertine-spring fluid compositions we observe is representative of endogenic influenced fluids while river sample compositions are representative

of epigenic influenced fluids of the Albuquerque hydrologic basin. The following is a summary of our results:

- 1) $^{234}\text{U}/^{238}\text{U}$ signatures of spring samples range from 2.9 ± 0.002 to 5.5 ± 0.004 . River sample $^{234}\text{U}/^{238}\text{U}$ ratios range from 1.6 ± 0.003 to 1.9 ± 0.003 . The higher $^{234}\text{U}/^{238}\text{U}$ signature in travertine-precipitating springs is indicative of mixing with a more radiogenic fluids similar to those which would be found in water-rock interactions with Precambrian basement granite. This is supported by similarly high $^{87}\text{Sr}/^{86}\text{Sr}$ signatures.
- 2) $^{87}\text{Sr}/^{86}\text{Sr}$ signatures in travertine-precipitating springs range from 0.714 ± 0.0001 to 0.717 ± 0.0001 . River sample $^{87}\text{Sr}/^{86}\text{Sr}$ ratios range from 0.709 ± 0.0001 to 0.710 ± 0.0001 . The higher $^{234}\text{U}/^{238}\text{U}$ signature in travertine-precipitating springs is indicative of mixing with small volumes of more radiogenic fluids similar to those which would be found in water-rock interactions with Precambrian basement granite.
- 3) Discernable major ion variations in samples of this study can also be explained by mixing of small volumes endogenic fluids with larger volumes of epigenic fluids near the surface. Endogenic fluids have variable compositions and three geographically distinct hydrochemical facies compositions were identified with varying endogenic fluid contributions. Hydrogeochemical facies 1 samples have a Na-Cl dominant composition, correlate with high TDS, conductivity, $^{234}\text{U}/^{238}\text{U}$, $^{87}\text{Sr}/^{86}\text{Sr}$, and are located on the Santa Fe fault zone. This group is interpreted to reflect endogenic fluid sources that mix with epigenic fluids along their trajectory. Hydrogeochemical facies 3 samples have a mixed cation-anion composition, correlate with low TDS, conductivity, $^{234}\text{U}/^{238}\text{U}$, $^{87}\text{Sr}/^{86}\text{Sr}$, and are located away from major fault systems in the basin. This group is interpreted to reflect epigenic meteoric fluids that interact with alluvial aquifers in the Santa Fe group sediments.

- 4) Previous studies, confirmed endogenic sources for spring samples collected on the western margin of the Rio Grande rift near the Socorro Magma Body (Williams et al., 2013, Prewisch et al., 2014) and around the Valles Caldera area (Crossey et al., 2011; Blomgren et al., 2019; McGibbon et al., 2018). This study serves as a link between the two aforementioned regions to confirm that the western margin faults of the Rio Grande rift, from the northern portion of the Socorro Basin to the southern portion of the San Luis Basin, act as conduits that allow endogenic fluids to reach the surface where they mix with epigenic fluids.

4.8 REFERENCES

- Allen, M.S., and Foord, E.E., 1991, Geological geochemical and isotopic characteristics of the Lincoln County porphyry belt, N.M.: Implications for regional tectonics and mineral deposits: New Mexico Geological Society Fall Field Conference Guidebook, v. 42, p. 97-115.
- Andersen, M.B., Erel, Y., Bourdon, B., 2009, Experimental evidence for ^{234}U – ^{238}U fractionation during granite weathering with implications for $^{234}\text{U}/^{238}\text{U}$ in natural waters: *Geochim. Cosmochim. Acta*, v. 73, p. 4124–4141.
- Bachman, G.O. and Mehnert, H.H., 1978, New K-Ar dates and the late Pliocene to Holocene geomorphic history of the central Rio Grande region, New Mexico. *Geological Society of America Bulletin*, 89(2), pp.283-292.
- Baldrige, W.S., Olsen, K.H., and Callender, J.F., 1984, Rio Grande rift: Problems and Perspectives: New Mexico Geological Society, Guidebook 35, p. 1-12.
- Barton C.A., Zoback M.D., Moos D (1995) Fluid flow along potentially active faults in crystalline rock. *Geology*, 23, 683–868.

- Bexfield, L.M., Plummer, L.N., 2003, Occurrence of arsenic in ground water of the middle Rio Grande Basin, central New Mexico. In: Welch, A.H., Stollenwerk, K.G. (Eds.), *Arsenic in Ground Water: Geochemistry and Occurrence*. Kluwer Academic Publishers, pp. 295–327.
- Blomgren, V.J., Crossey, L.J., Karlstrom, K.E., Fischer, T.P. and Darrah, T.H., 2019, Hot spring hydrochemistry of the Rio Grande rift in northern New Mexico reveals a distal geochemical connection between Valles Caldera and Ojo Caliente. *Journal of Volcanology and Geothermal Research*, 387, p.106663. doi: 10.1016/j.jvolgeores.2019.106663
- Bullen, T.D., Krabbenhoft, D.P. & Kendall, C., 1996, Kinetic and mineralogic controls on the evolution of groundwater chemistry and $^{87}\text{Sr}/^{86}\text{Sr}$ in a sandy silicate aquifer, northern Wisconsin, USA: *Geochimica et Cosmochimica Acta*, v. 60, p. 1807-1821.
- Burke, W.H., Denison, R.E., Hetherington, E.A., Koepnick, R.B., Nelson, H.F. and Otto, J.B., 1982, Variation of seawater $^{87}\text{Sr}/^{86}\text{Sr}$ throughout Phanerozoic time. *Geology*, 10(10), pp.516-519.
- Callender, J. F., and Zilinski, R. E. Jr., 1976, Kinematics of Tertiary and Quaternary deformation along the eastern edge of the Lucero Uplift, central New Mexico: *New Mexico Geological Society Special Publication 6*, p. 53- 61.
- Chabaux F., A.S. Cohen, R.K. O’Nions, and J.R. Hein, 1995, ^{238}U - ^{234}U - ^{230}Th chronometry of Fe- Mn crusts. *Geochimica et Cosmochimica Acta* 59, 633–638.
- Chabaux, F., Riotte, J., and Dequincey., O., 2003, U-Th-Ra fractionation during weathering and river transport: *Reviews in Mineralogy and Geochemistry*, v. 52, p. 533–576.
- Chapin, C.E., 1979, Evolution of the Rio Grande rift—A summary. *Rio Grande rift: tectonics and magmatism*, 14, pp.1-6.

- Claesson, L., Skelton, A., Graham, C. and Morth, C.M., 2007, The timescale and mechanisms of fault sealing and water- rock interaction after an earthquake. *Geofluids*, 7(4), pp.427-440.
- Clark, K.I., Fritz P., 1997, *Environmental Isotopes in Hydrogeology*: Lewis Publishers, New York, pp. 328.
- Crossey, L.J., Fischer, T.P., Patchett, P.J., Karlstrom, K.E., Hilton, D.R., Huntoon, P., and Reynolds, A.C., 2006, Dissected hydrologic system at Grand Canyon: Interaction between upper world and lower world waters in modern springs and travertine: *Geology*, v. 34, p. 25-28.
- Crossey, L.J., Karlstrom, K.E., Springer, A., Newell, D., Hilton, D., and Fischer, T., 2009, Degassing of mantle-derived CO₂ and ³He from springs in the southern Colorado Plateau region— neotectonic connections and implications for groundwater systems: *Geological Society of America Bulletin*, v. 121, p. 1034-1053. DOI 10.1130/B26394.
- Crossey, L.J., Karlstrom, K.E., Newell, D.N., Kooser, A., and Tafoya, A., 2011, The La Madera travertines, Rio Ojo Caliente, northern New Mexico: Investigating the linked system of CO₂-rich springs and travertines as neotectonic and paleoclimate indicators, in Koning, D.J., et al., eds., *Geology of the Tusas Mountains and Ojo Caliente: New Mexico Geological Society Guide- book*, v. 62, p. 301–316.
- Crossey, L.J., Karlstrom, K.E., Dorsey, R., Pearce, J.L., Wan, E., Beard, L.S., Asmeron, Y., Polyak, V., Crow, R., Cohen, A., and Bright, J., 2015, The importance of groundwater in propagating downward integration of the 6–5 Ma Colorado River system—Geochemistry of springs, travertines and lacustrine carbonates of the Grand Canyon region over the past 12 million years: *Geosphere*, <https://doi.org/10.1130/GES01073.1>.

- Deming, D., 1992, Catastrophic release of heat and fluid flow in the continental crust. *Geology*, 20(1), 83-86.
- Dequincey, O., Chabaux, F., Clauer, N., Sigmarsson, O., Liewig, N., Leprun, J.C., 2002, Chemical mobilizations in laterites : evidence from trace elements and ^{238}U – ^{234}U – ^{230}Th disequilibria. *Geochimica et Cosmochimica Acta*66, 1197–1210.
- Deschamps, P., Hillaire-Marcel, C., Michelot, J.L., Doucelance, R., Ghaleb, B. and Buschaert, S., 2004, $^{234}\text{U}/^{238}\text{U}$ Disequilibrium along stylolitic discontinuities in deep Mesozoic limestone formations of the Eastern Paris basin: evidence for discrete uranium mobility over the last 1–2 million years.
- Dunbar, N., 2005, Quaternary volcanism in New Mexico: New Mexico Museum of Natural History and Science Bulletin, v. 28, p. 95–106.
- Durand, S., Chabaux, F., Rihs, S., Düringer, P., Elsass, P., 2005, U isotope ratios as tracers of groundwater inputs into surface waters: example of the Upper Rhine hydrosystem. *Chemical Geology*220(1), 1-19.
- Duschatco, R.W., 1953, Fracture studies in the Lucero uplift, New Mexico: United States Atomic Energy Commission, RME-3072, 49 p.
- Fleischer, R. L., 1980, Isotopic Disequilibrium of Uranium: Alpha-Recoil Damage and Preferential Solution Effects. *Science*,207,979
- Fossen, H., Schultz, R.A., Rundhovde, E., Rotevatn, A. and Buckley, S.J., 2010, Fault linkage and graben stepovers in the Canyonlands (Utah) and the North Sea Viking Graben, with implications for hydrocarbon migration and accumulation. *AAPG bulletin*, 94(5), pp.597-613.

- Garcia, S., 2017, Tracing anthropogenic salinity inputs to the semi-arid Rio Grande river: A multi-isotope tracer approach [M.S. thesis]: El Paso, University of Texas at El Paso, 90 p.
- Goff, F., McCormick, T., Gardner, J.N., Trujillo, P.E., Counce, D., Vidale, R., and Charles, R., 1983, Water geochemistry of the Lucero uplift, New Mexico: A geothermal investigation of low-temperature mineralized fluids: Los Alamos National Laboratory LA9738-OBES, 26 p., doi:10.2172/6246390.
- Goff F, Shevenel L., 1987, Travertine deposits of Soda Dam, New Mexico, and their implications for the age and evolution of the Valles caldera hydrothermal system. *Geological Society of America Bulletin* 99: 292–302.
- Goff, F., Evans, W.C., Gardner, J.N., Adams, A. and Janik, C.J., 1994, Interpretation of in-situ fluid samples from geothermal wells: example from hole VC-2B, Valles caldera, New Mexico. *Geothermal science and technology*, 4(2), pp.97-128.
- Granet, M., Chabaux, F., Stille, P., France-Lanord, C., Pelt, E., 2007, Time-scales of sedimentary transfer and weathering processes from U-series nuclides: clues from the Himalayan rivers. *Earth Planet. Sci. Lett.* 261 (3– 4), 389–406.
- Hogan, J.F., Phillips, F.M., Mills, S.K., Hendrickx, J.M.H., Ruiz, J., Chesley, J.T., and Asmerom, Y., 2007, Geologic origins of salinization in a semi-arid river: The role of sedimentary basin brines: *Geology*, v. 35, p. 1063–1066, doi:10.1130/G23976A.1.
- Ivanovich, M. and Harmon, R.S., 1992, Uranium-series disequilibrium: Applications to earth, marine, and environmental sciences. Clarendon Press, Oxford University Press.
- Jweda, J., Bolge, L., Class, C., and Goldstein, S. L., 2015, High precision Sr-Nd-Hf-Pb isotopic compositions of USGS reference material BCR-2: *Geostandards and Geoanalytical Research*, v. 40, n. 1, p. 101–115, <https://doi.org/10.1111/j.1751-908X.2015.00342.x>

- Johnson, C.M. and Thompson, R.A., 1991, Isotopic composition of Oligocene mafic volcanic rocks in the northern Rio Grande rift: evidence for contributions of ancient intraplate and subduction magmatism to evolution of the lithosphere. *Journal of Geophysical Research: Solid Earth*, 96(B8), pp.13593-13608.
- Johnson, P.S., Koning, D.J., Partey, F.K., 2013, Shallow groundwater geochemistry in the Española Basin, Rio Grande rift, New Mexico: evidence for structural control of a deep thermal source. *Geol. Soc. Am. Spec. Pap.* 494, 261–301. [https://doi.org/10.1130/2013.2494\(11\)](https://doi.org/10.1130/2013.2494(11)).
- Kirkland, D.W., Denison, R.E., and Evans, R., 1995, Middle Jurassic Todilto Formation of Northern New Mexico and Southwestern Colorado: Marine or Nonmarine?: *New Mexico Bureau of Mines and Mineral Resources Bulletin* 147, 37 p.
- Konter, J.G., Storm, L.P., 2014, High precision $^{87}\text{Sr}/^{86}\text{Sr}$ measurements by MC-ICP-MS, simultaneously solving for Kr interferences and mass-based fractionation, *Chemical Geology*, 385, 26-34.
- Kronfeld, J., Gradsztajn, E., Muller, H. W., Radin, J., Yaniv, A., and Zach, R., 1975, Excess ^{234}U : An aging effect in confined waters: *Earth and Planetary Science Letters*, v. 27, p. 342–345.
- Kronfeld, J., Vogel, J.C. and Talma, A.S., 1994, A new explanation for extreme $^{234}\text{U}/^{238}\text{U}$ disequilibria in a dolomitic aquifer. *Earth and Planetary Science Letters*, 123(1-3), pp.81-93.
- May, S.J., Kelley, S.A., and Russell, L.R., 1994, Footwall unloading and rift shoulder uplifts in the Albuquerque Basin: Their relation to syn-rift fanglomerates and apatite fission-track ages, in Keller, G.R., and Cather, S.M., eds., *Basins of the Rio Grande Rift: Structure,*

- Stratigraphy, and Tectonic Setting: Geological Society of America, Special Paper 291, p. 125–134.
- McArthur, J.M., Howarth, R.J., and Bailey, T.R., 2001, Strontium isotope stratigraphy: LOWESS Version 3: Best fit to the marine Sr isotope curve for 0–509 Ma and accompanying look-up table for deriving numerical age: *Journal of Geology*, v. 109, p. 155–170, doi:10.1086/319243.
- McMillan, N. J., A. P. Dickin, and D. Haag, 2000, Evolution of magma source regions in the Rio Grande rift, southern New Mexico, *Geol. Soc. Am. Bull.*, 112, 1582 – 1593.
- McGibbon, C., Crossey, L.J., Karlstrom, K.E., Grulke, T., 2018, Carbonic springs as distal manifestations of geothermal system, highlighting the importance of fault pathways and hydrochemical mixing: example from the Jemez Mountains, New Mexico. *Appl. Geochem.* 98, 45–57. <https://doi.org/10.1016/j.apgeochem.2018.08.015>.
- Morgan, P., Seager, W.R., and Golombek, M.P., 1986, Cenozoic thermal, mechanical, and tectonic evolution of the Rio Grande rift: *Journal of Geophysical Research*, v. 91, p. 6263-6276, <https://doi.org/10.1029/JB091iB06p06263>.
- Mukhopadhyay, B. and Brookins, D.G., 1976, Strontium isotopic composition of the Madera Formation (Pennsylvanian) near Albuquerque, New Mexico. *Geochimica et Cosmochimica Acta*, 40(6), pp.611-616.
- Newell, D.L., Crossey, L.J., Karlstrom, K., Fischer, T., and Hilton, D., 2005, Evidence for continental-scale links between the mantle and groundwater systems of the Western United States based on hydrogeochemistry of travertine-depositing springs and regional synthesis of helium isotopic data: *GSA Today*, v. 15, no. 12, p. 4-10.

- Nyachoti, S.K., 2016, Application of uranium and strontium isotopes as salinity and paleo-environmental conditions tracers: Insight from the Rio Grande River and pedogenic carbonates in drylands soils of Southwest, USA. The University of Texas at El Paso.
- Paces, J. B. and Wurster, F. C., 2014, Natural uranium and strontium isotope tracers of water sources and surface water–groundwater interactions in arid wetlands–Pahrnagat Valley, Nevada, USA. *Journal of Hydrology*, 517, 213-225.
- Pelt, E., Chabaux, F., Innocent, C., Navarre-Sitchler, A.K., Sak, P.B., and Brantley, S.L., 2008, Uranium thorium chronometry of weathering rinds: rock alteration rate and paleo-isotopic record of weathering fluids: *Earth and Planetary Science Letters*, v. 276, p. 98-105.
- Pett-Ridge, J.C., Derry, L.A., and Kurtz, A.C., 2009, Sr isotopes as a tracer of weathering processes and dust inputs in a tropical granitoid watershed, Luquillo Mountains, Puerto Rico: *Geochimica et Cosmochimica Acta* 73.1 (2009): 25-43.
- Priewisch, A., Crossey, L. J., Karlstrom, K. E., Polyak, V. J., Asmerom, Y., Nereson, A., & Ricketts, J. W. 2014, U-series geochronology of large-volume Quaternary travertine deposits of the southeastern Colorado Plateau: Evaluating episodicity and tectonic and paleohydrologic controls. *Geosphere*, 10(2), 401-423.
- Reiter, M., Chamberlin, R.M., and Love, D.W., 2010, New data reflect on the thermal antiquity of the Socorro magma body locale, Rio Grande Rift, New Mexico: *Lithosphere*, v. 2, p. 447–453, doi:10.1130/L115.1.
- Ricketts, J.W., Karlstrom, K.E., Priewisch, A., Crossey, L.J., Polyak, V.J., and Asmerom, Y., 2014, Quaternary extension in the Rio Grande rift at elevated strain rates recorded in travertine deposits, central New Mexico: *Lithosphere*, v. 6, p. 3–16, doi: 10.1130/L278.1.

- Rosholt, J.N., 1976, $^{230}\text{Th}/^{234}\text{U}$ dating of travertine and caliche rinds, GSA abstr. Prog. 8, 1076.
- Ricketts, J.W. and Karlstrom, K.E., 2014, Geologic map of the South Garcia SE 7.5-minute Quadrangle, Valencia County, New Mexico. New Mexico Bureau of Geology and Mineral Resources Open-File Geologic Map 246, scale 1: 24,000.
- Schmandt, B., and Humphreys, E., 2010, Complex subduction and small-scale convection revealed by body-wave tomography of the western United States upper mantle: *Earth and Planetary Science Letters*, v. 297, p. 435– 445, doi:10.1016/j.epsl.2010.06.047.
- Sims K.W.W., Gill, J.B., Dosseto, A., Hoffmann, D.L., Lundstrom, C.C., Williams, R.W., Ball, L., Tollstrup, D., Turner, S., Pyrtulak, J., Glessner, J.G., Standish, J.J., Elliott, T., 2008, An Inter-Laboratory Assessment of the Thorium Isotopic Composition of Synthetic and Rock Reference Materials. *Geostandards and Geoanalytical Research* 32(1), 65-91.
- Szynkiewicz, A., Borrok, D.M., Ganjgunte, G.K., Skrzypek, G., Ma, L., Rearick, M.S., Perkins, G.B. 2015. Isotopic studies of the Upper and Middle Rio Grande. Part 2- Salt loads and human impacts in south New Mexico and west Texas, *Chemical Geology*, <http://dx.doi.org/10.1016/j.chemgeo.2015.05.023>.
- Taggart, J.E., and Brookins, D.G., 1975, Rb-Sr whole rock age determinations for Sandia granite and Cibola gneiss, New Mexico: *Isochron/West*, no. 12, p. 5–8.
- Williams, A.J., Crossey, L.J., Karlstrom, K.E., Newell, D., Person, M., and Woolsey, E., 2013, Hydrogeochemistry of the Middle Rio Grande aquifer system—Fluid mixing and salinization of the Rio Grande due to fault inputs: *Chemical Geology*, v. 351, p. 281–298, doi:10.1016/j.chemgeo.2013.05.029.

- Williams, R.T., Goodwin, L.B., Mozley, P.S., Beard, B.L., and Johnson, C.M., 2015, Tectonic controls on fault zone flow pathways in the Rio Grande rift, New Mexico, USA: *Geology*, v. 43, p. 723–726, doi:10.1130/G36799.1.
- Williams, R. T., Beard, B. L., Goodwin, L. B., Sharp, W. D., Johnson, C. M., & Mozley, P. S., 2018, Radiogenic isotopes record a “drop in a bucket”—A fingerprint of multikilometer-scale fluid pathways inferred to drive fault-valve behavior. *Journal of Structural Geology*, 125, 262–269. <https://doi.org/10.1016/j.jsg.2018.07.023>
- Young, B. W., & Chan, M. A., 2017, Gypsum veins in Triassic Moenkopi mudrocks of southern Utah: Analogs to calcium sulfate veins on Mars. *Journal of Geophysical Research: Planets*, 122, 150– 171. <https://doi.org/10.1002/2016JE005118>
- Zieliński, M., Dopieralska, J., Belka, Z., Walczak, A., Siepak, M., Jakubowicz, M., 2016, Sr isotope tracing of multiple water sources in a complex river system, Noteć River, central Poland. *Science of the Total Environment*, 548-549, 307–316. <https://doi.org/10.1016/j.scitotenv.2016.01.0363.9>
- Zimmerer, M.J., Laffety, J., and Coble, M.A., 2016, The eruptive and magmatic history of the youngest pulse of volcanism at the Valles caldera: Implications for successfully dating late Quaternary eruptions: *Journal of Volcanology and Geothermal Research*, v. 310, p. 50–57, <https://doi.org/10.1016/j.jvolgeores.2015.11.021>.

4.9 TABLES

Table 4.1 Spring and River Data

Sample Name	Latitude	Longitude	Sample Type	Date Collected	Elevation (m)	pH	Temp (°C)	DO (%)	Cond (us/cm)	TDS (mg/L)
PLTS01	34.804333	-107.087139	Travertine Spring	10/6/18	1663	7.08	nr	2.9	32755	34629
PLTS02	34.804333	-107.087139	Travertine Spring	10/6/18	1664	7.15	nr	98.1	34952	33607
PLTS03	34.808194	-107.090333	Travertine Spring	10/6/18	1704	8.41	nr	54.8	2906	33498
PLTS04	34.808139	-107.091028	Travertine Spring	10/6/18	1707	7.73	nr	55.0	29009	29715
PLTS05	34.808722	-107.088917	Travertine Spring	10/6/18	1677	8.23	nr	48.7	24803	25346
PLTS06	34.812194	-107.08850	Travertine Spring	10/6/18	1684	7.98	nr	47.3	30324	30289
PLTS07	34.815167	-107.089028	Travertine Spring	10/6/18	1668	8.13	nr	43.8	33801	33271
PLTS08	34.827056	-107.085687	Travertine Spring	10/6/18	1616	8.01	nr	31.1	41378	35854
PLTS09	34.850000	-107.089472	Travertine Spring	10/6/18	1670	7.27	12	9.5	32620	30226
PLTS10	34.852722	-107.087528	Travertine Spring	10/6/18	1643	7.64	nr	8.3	35052	30205
PLTS11	34.856681	-107.085858	Travertine Spring	3/30/17	1630	8.03	15.4	8.9	33836	30216
PLTS12	34.859621	-107.084795	Travertine Spring	3/30/17	1625	7.98	16.7	50.5	33854	34118
PLTS13	34.857981	-107.094684	Travertine Spring	3/30/17	1684	8.13	16.8	35.1	34063	31674
RP01	34.793344	-106.989566	Rio Puerco	4/1/17	1528	8.11	3.4	4.6	1237	1268
RP02	34.796667	-106.990667	Rio Puerco	10/6/18	1528	8.94	nr	4.6	1333	1295
RP03	34.409587	-106.853537	Rio Puerco	10/6/18	1444	8.89	nr	nr	1155	1239
RG01	34.803408	-106.718205	Rio Grande	10/6/18	1480	8.77	nr	4.2	379	445
RG02	34.347975	-106.856422	Rio Grande	10/6/18	1440	8.77	nr	nr	705	763

nr = not recorded

Table 4.2 Isotope Data

Sample Name	Sample Type	U (ppb)	(²³⁴ U/ ²³⁸ U)	± 2se	Sr (ppm)	(⁸⁷ Sr/ ⁸⁶ Sr) _c	± 2se
PLTS01	Travertine Spring	15.579	4.028	0.004	12.259	0.71606	0.00002
PLTS02	Travertine Spring	15.326	4.018	0.004	12.087	0.71604	0.00003
PLTS03	Travertine Spring	20.007	3.147	0.006	9.190	0.71516	0.00016
PLTS04	Travertine Spring	21.489	3.246	0.002	11.828	0.71538	0.00002
PLTS05	Travertine Spring	11.549	3.174	0.003	9.288	0.71399	0.00014
PLTS06	Travertine Spring	12.961	3.720	0.003	11.255	0.71636	0.00001
PLTS07	Travertine Spring	23.081	2.966	0.002	10.232	0.71482	0.00003
PLTS08	Travertine Spring	11.855	4.128	0.002	4.521	0.71697	0.00005
PLTS09	Travertine Spring	14.460	4.017	0.003	11.319	0.71699	0.00006
PLTS10	Travertine Spring	11.403	4.454	0.003	10.605	0.71695	0.00003
PLTS11	Travertine Spring	18.656	3.782	0.002	10.962	0.71691	0.00002
PLTS12	Travertine Spring	18.176	3.249	0.002	12.173	0.71588	0.00003
PLTS13	Travertine Spring	18.311	5.406	0.004	11.429	0.71544	0.00003
RP01	Rio Puerco	8.791	1.875	0.002	3.226	0.70972	0.00002
RP02	Rio Puerco	3.403	1.923	0.003	1.169	0.70926	0.00005
RP03	Rio Puerco	4.088	1.859	0.003	1.137	0.70926	0.00006
RG01	Rio Grande	2.065	1.698	0.003	0.491	0.71012	0.00014
RG02	Rio Grande	3.929	1.708	0.002	0.615	0.70960	0.00008

Table 4.3 Major Ion Chemistry (ppm)

Sample Name	Sample Type	Ca	Mg	Na	K	HCO ₃ ⁻	SO ₄	Cl	Si	NO3	F
PLTS01	Travertine Spring	613	187	9420	234	6481	7408	10473	6	11	3
PLTS02	Travertine Spring	623	186	9306	225	12140	4723	6589	6	7	1
PLTS03	Travertine Spring	373	207	8885	207	6058	7969	10007	13	9	1
PLTS04	Travertine Spring	667	179	7960	191	5610	6670	8617	9	8	2
PLTS05	Travertine Spring	539	154	6809	164	9495	3935	4405	7	9	1
PLTS06	Travertine Spring	338	132	8553	223	7558	5421	8196	7	9	2
PLTS07	Travertine Spring	438	143	7681	193	7180	5881	7228	7	8	2
PLTS08	Travertine Spring	157	135	10626	294	5176	7721	11881	9	11	3
PLTS09	Travertine Spring	579	125	8488	242	5573	6214	9130	8	-	3
PLTS10	Travertine Spring	424	104	8267	247	6453	5959	8856	10	-	3
PLTS11	Travertine Spring	502	115	8377	244	6013	6086	8993	9	9	3
PLTS12	Travertine Spring	618	187	9363	230	6699	6066	8531	6	9	2
PLTS13	Travertine Spring	549	143	8760	238	6184	5810	8420	8	8	3
RP01	Rio Puerco	105	26	164	5	498	443	43	1	8	1
RP02	Rio Puerco	104	25	167	5	562	408	50	2	5	1
RP03	Rio Puerco	105	24	162	4	435	496	37	1	10	1
RG01	Rio Grande	34	7	42	4	285	58	22	9	4	1
RG02	Rio Grande	68	7	91	3	352	204	45	7	95	2

4.10 FIGURES

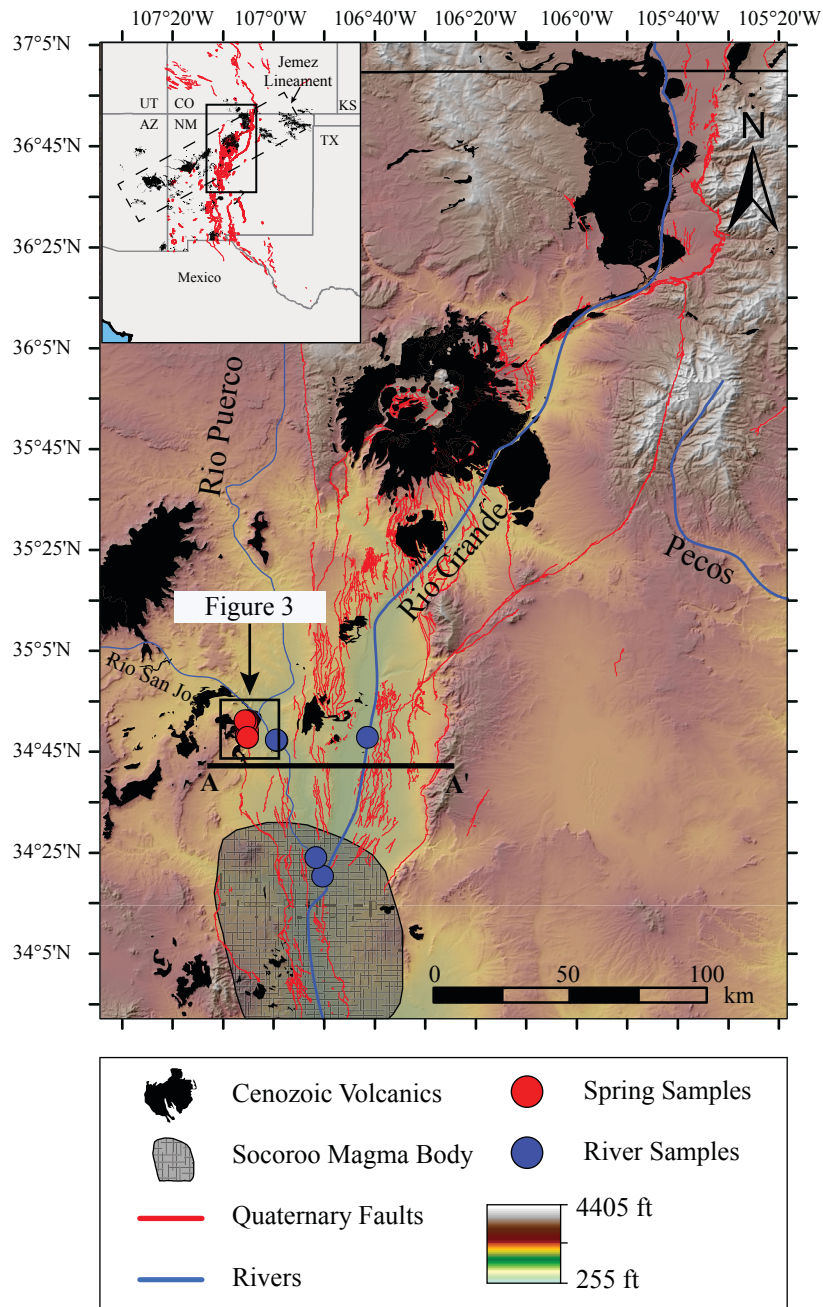


Figure 4.1 Digital elevation model showing location of travertine-precipitating springs and river samples collected in this study. Also shown are faults associated with the Rio Grande rift (red lines), the Jemez Lineament (black blobs), and the outline of the Socorro Magma Body (faded grey circle).

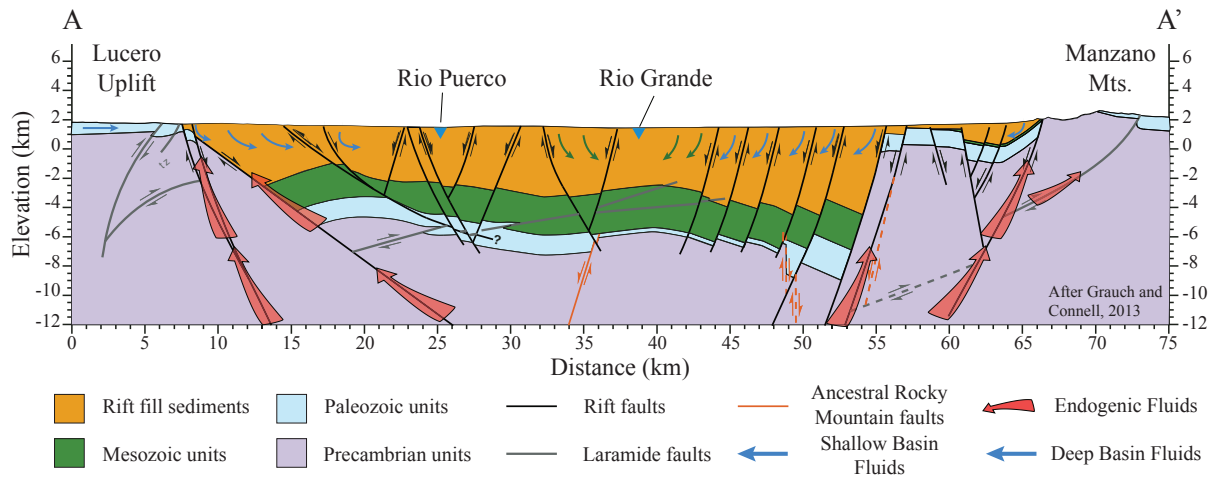


Figure 4.2 Geologic cross-section line A-A' from map on Figure 1 showing asymmetrical basins bounded by major rift bounding faults as well as smaller intrabasin faults. Hypothesized fluid flow types are shown in red arrows to represent endogenic fluids, blue arrows represent epigenic fluids in shallow basins adjacent to major rift bounding faults, and green arrows represent epigenic fluids in deeper basins of the Rio Grande rift system. Potential lithology endmembers include Precambrian (crystalline basement), Paleozoic (mainly carbonates), Mesozoic (mix of sedimentary rocks), and Quaternary (rift fill) units.

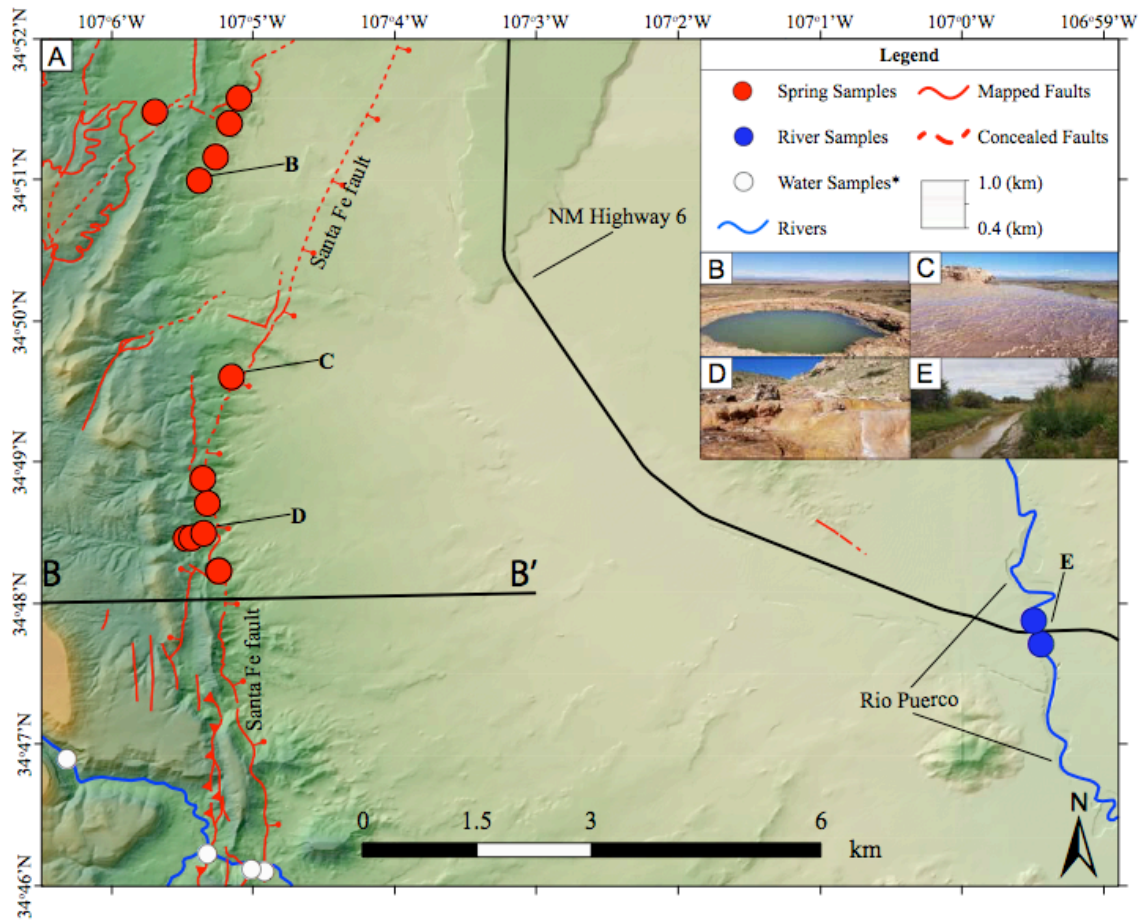


Figure 4.3 Digital elevation map of study area depicting faults (red solid and dashed lines) of the Santa Fe fault system. Location of collected travertine-precipitating springs are represented by red circles while two river samples collected from the Rio Puerco are represented by blue circles. Three more river samples were collected but are not observable at the scale of this map. Refer to Figure 1 for location of other river samples of this study. White circles are river and spring samples from Williams et al., (2013).

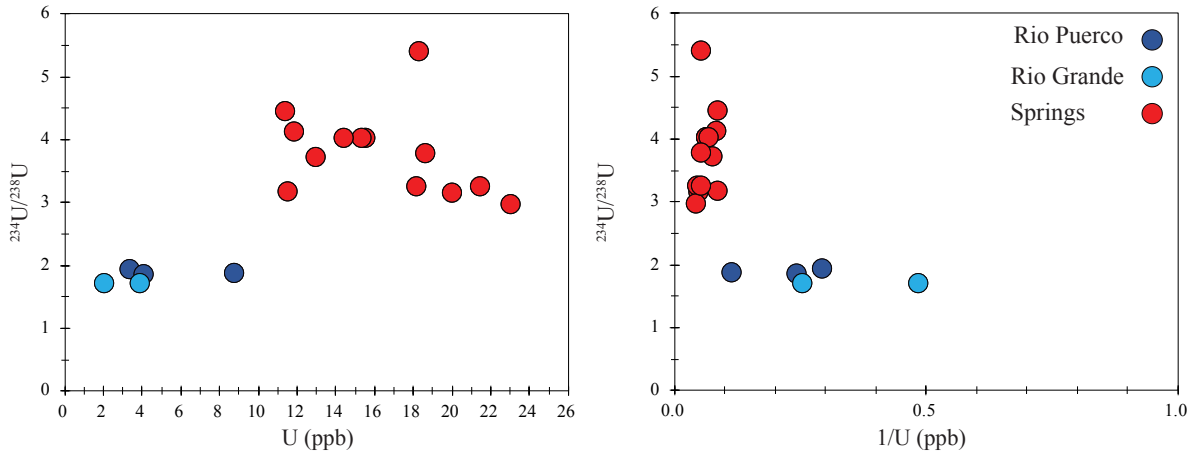


Figure 4.4 Left: $^{234}\text{U}/^{238}\text{U}$ vs U (ppb) plot. Spring samples (red circles) tend to have higher $^{234}\text{U}/^{238}\text{U}$ ratios and U concentrations compared to river samples (blue and light blue circles). Right: $^{234}\text{U}/^{238}\text{U}$ vs $1/\text{U}$ (ppb) plot.

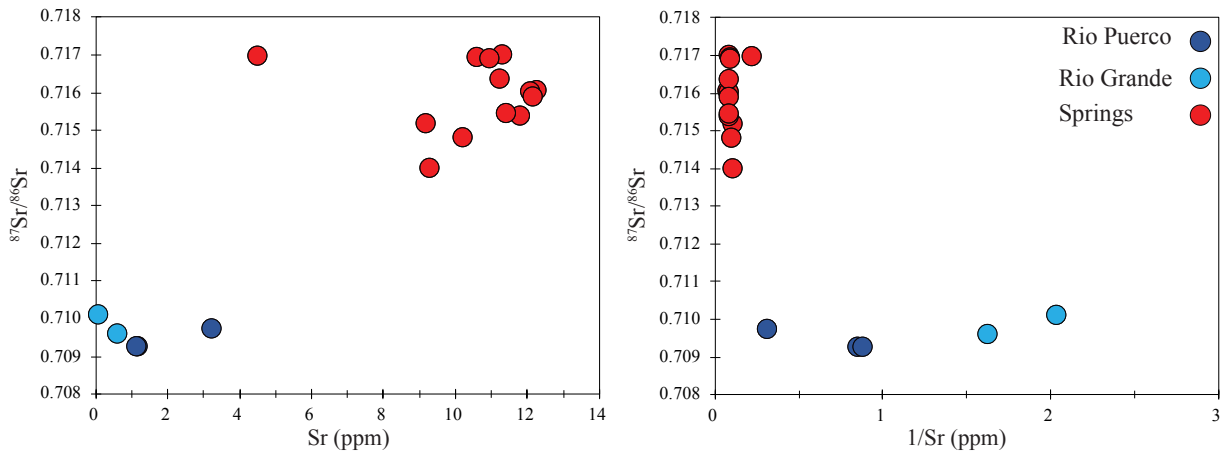


Figure 4.5 $^{87}\text{Sr}/^{86}\text{Sr}$ vs Sr (ppm) plot. Spring samples (red circles) tend to have higher $^{87}\text{Sr}/^{86}\text{Sr}$ ratios and Sr concentrations compared to river samples (blue and light blue circles).

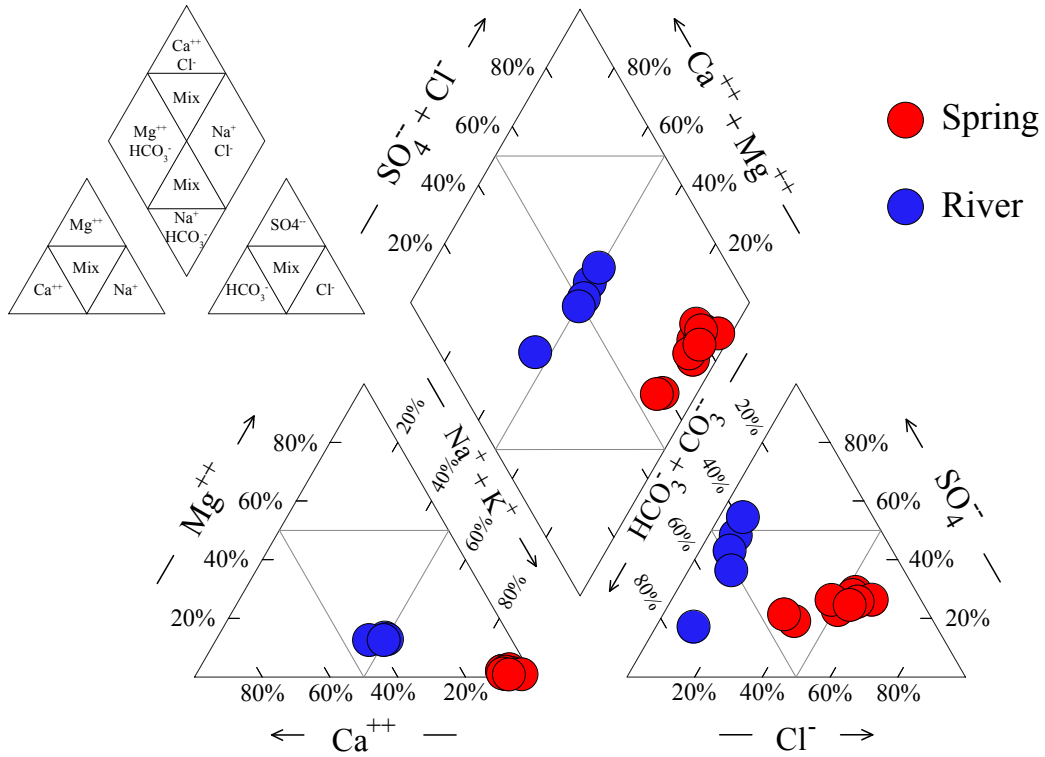
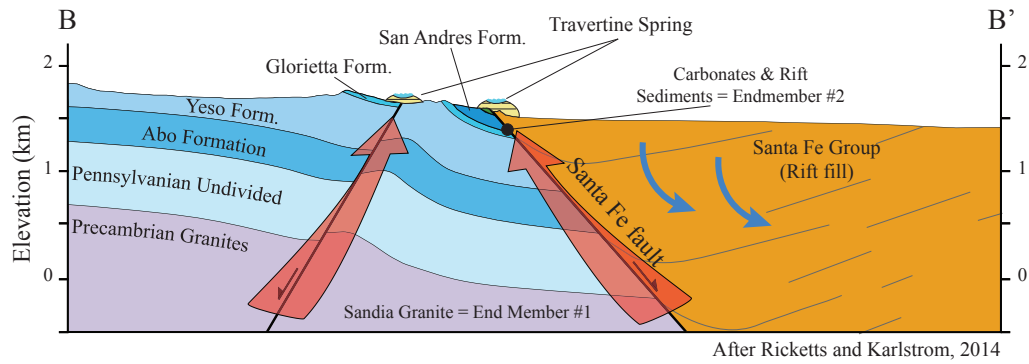


Figure 4.6 Piper diagram of study area showing two distinct hydrogeochemical facies. Travertine-precipitating spring samples lie within an endogenic facies with high amounts of Na and Cl relative to other ions. River samples lie within a mixed cation group representing epigenic facies.



	$(^{234}\text{U}/^{238}\text{U})$	$(^{87}\text{Sr}/^{86}\text{Sr})$		$(^{234}\text{U}/^{238}\text{U})$	$(^{87}\text{Sr}/^{86}\text{Sr})$
Mesozoic Units	---	0.706 - 0.709	Endogenic Fluids	> 2.00	0.735 - 0.748
Paleozoic Units	---	0.706 - 0.711	Shallow Basin Fluids	1.00 - 2.31	0.709 - 0.711
Precambrian Granites	> 2.00	0.735 - 0.748	Travertine Deposits	3.51 - 9.29	0.711 - 0.735

Figure 4.7 Cross section B-B' from Figure 3 showing lithology that hypothetical endogenic fluid flow paths would encounter in the Santa Fe fault system. Also shown are $^{234}\text{U}/^{238}\text{U}$ and $^{87}\text{Sr}/^{86}\text{Sr}$ signature of the different end members and lithologies located in our study. Sandia Granite (Endmember #1): $^{87}\text{Sr}/^{86}\text{Sr} = 0.748$, $[\text{Sr}] = 220$ ppm, $(^{234}\text{U}/^{238}\text{U})_i = 10$, $[\text{U}] = 4.7$ ppm; Rio Grande (Endmember #2): $^{87}\text{Sr}/^{86}\text{Sr} = 0.709$, $[\text{Sr}] = 0.490$ ppm, $(^{234}\text{U}/^{238}\text{U})_i = 1.69$, $[\text{U}] = 0.002$ ppm. Endmember #1 and #2 isotopic ratios and concentrations from Brookins and Majundir (1988), Brookins and Majundir (1982), Crossey et al., 2006, and this study. See text for references for other isotopic signatures.

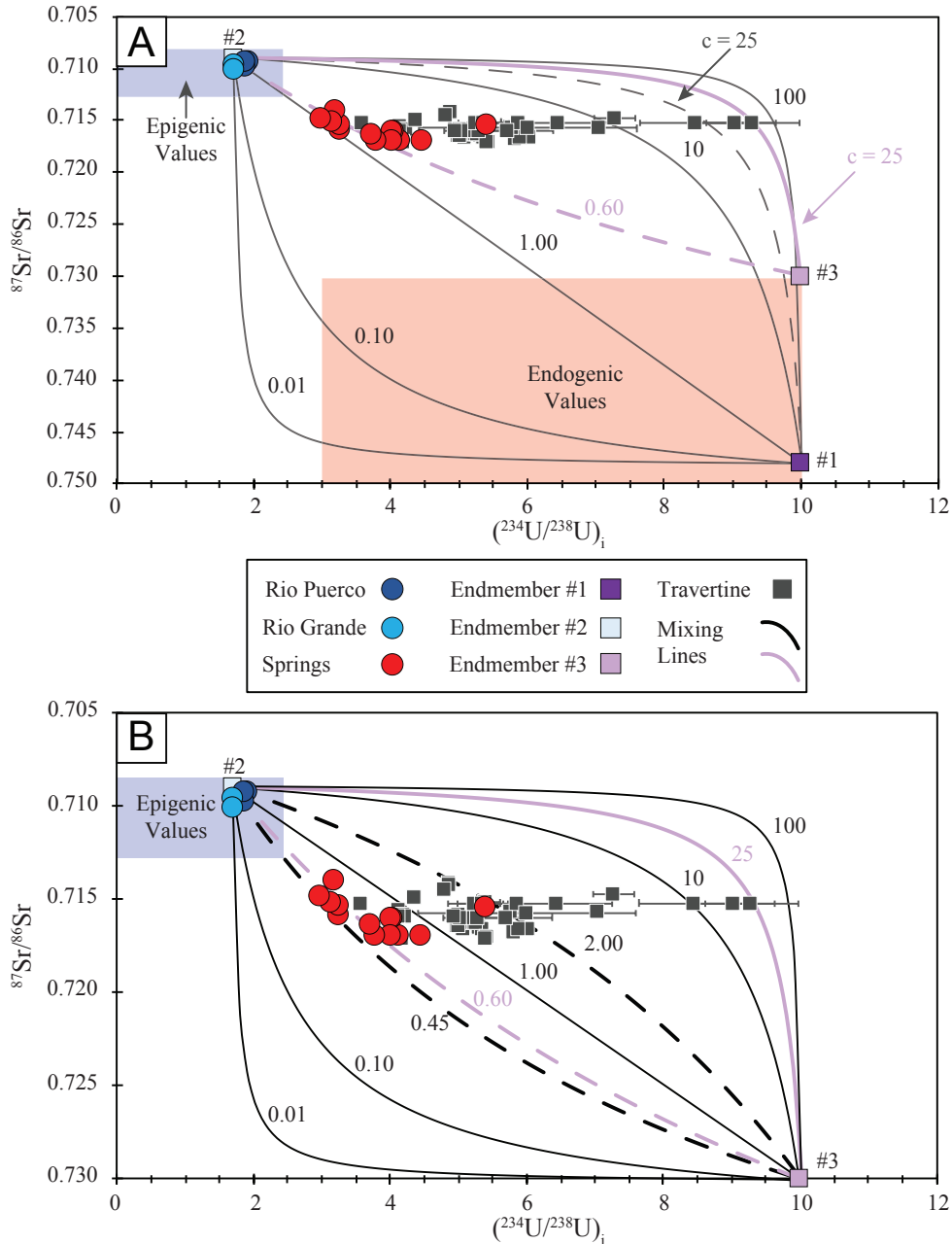


Figure 4.8 $^{87}\text{Sr}/^{86}\text{Sr}$ vs. $(^{234}\text{U}/^{238}\text{U})_i$ isotopic compositions mixing model between travertine-precipitating springs, river, and travertine samples. Three endmembers were considered for mixing lines. Endmember #1 = highly radiogenic crystalline basement, #2 = shallow meteoric fluids, and #3 less radiogenic crystalline basement. A) Mixing lines are shown for endmember #1 and #2. B) Various mixing lines between endmembers #2 and #3 are shown. Light red shaded rectangle is the region in which endogenic derived fluids would lie on this model. Light blue shaded rectangle is the region in which epigenic (i.e. meteoric) fluids would lie. Crystalline basement (Endmember #1): $^{87}\text{Sr}/^{86}\text{Sr} = 0.748$, $[\text{Sr}] = 220$ ppm, $(^{234}\text{U}/^{238}\text{U})_i = 10$, $[\text{U}] = 4.7$ ppm; Rio Grande (Endmember #2): $^{87}\text{Sr}/^{86}\text{Sr} = 0.709$, $[\text{Sr}] = 0.490$ ppm, $(^{234}\text{U}/^{238}\text{U})_i = 1.69$, $[\text{U}] = 0.002$ ppm; Crystalline basement (Endmember #3): $^{87}\text{Sr}/^{86}\text{Sr} = 0.730$, $[\text{Sr}] = 220$ ppm, $(^{234}\text{U}/^{238}\text{U})_i = 10$, $[\text{U}] = 4.7$ ppm.

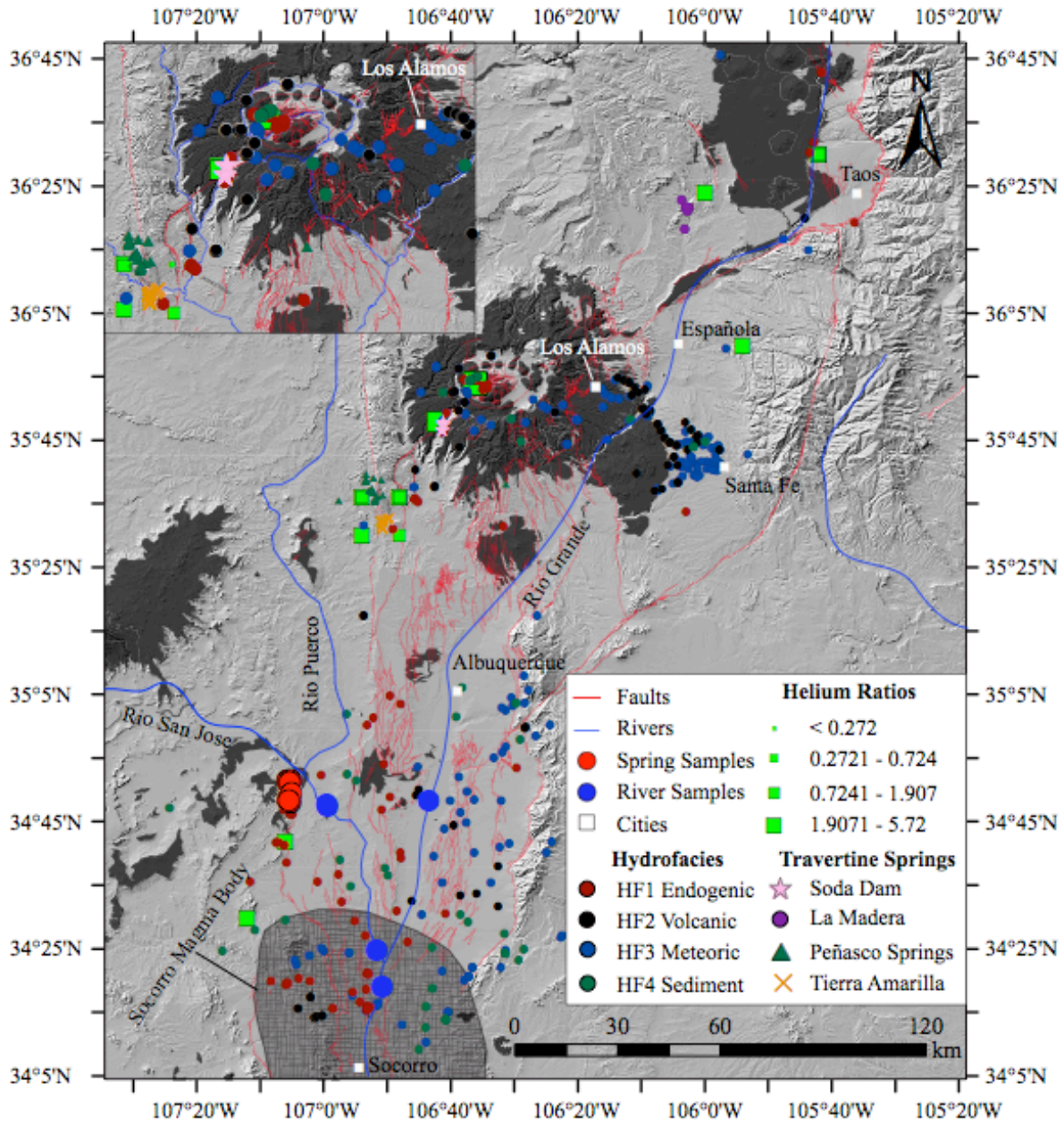


Figure 4.9 Water types of various spring, river, and well samples of the San Luis, Española, Albuquerque, and Socorro basin. Water types based on which hydrogeochemical facies data points plotted in on Figure 10. Classification scheme is very similar to those used by Goff and Shevenell, 1987, Williams et al., 2013, McGibbon et al., 2018, and Blomgren et al., 2019. Also pictured are $^3\text{He}/^4\text{He}$ ratios from Newell et al., 2005 showing anomalously high He ratios associated with localized mantle degassing underneath the Rio Grande rift. Travertine-precipitating springs all have endogenic signatures; different symbols are used to stand out their locations.

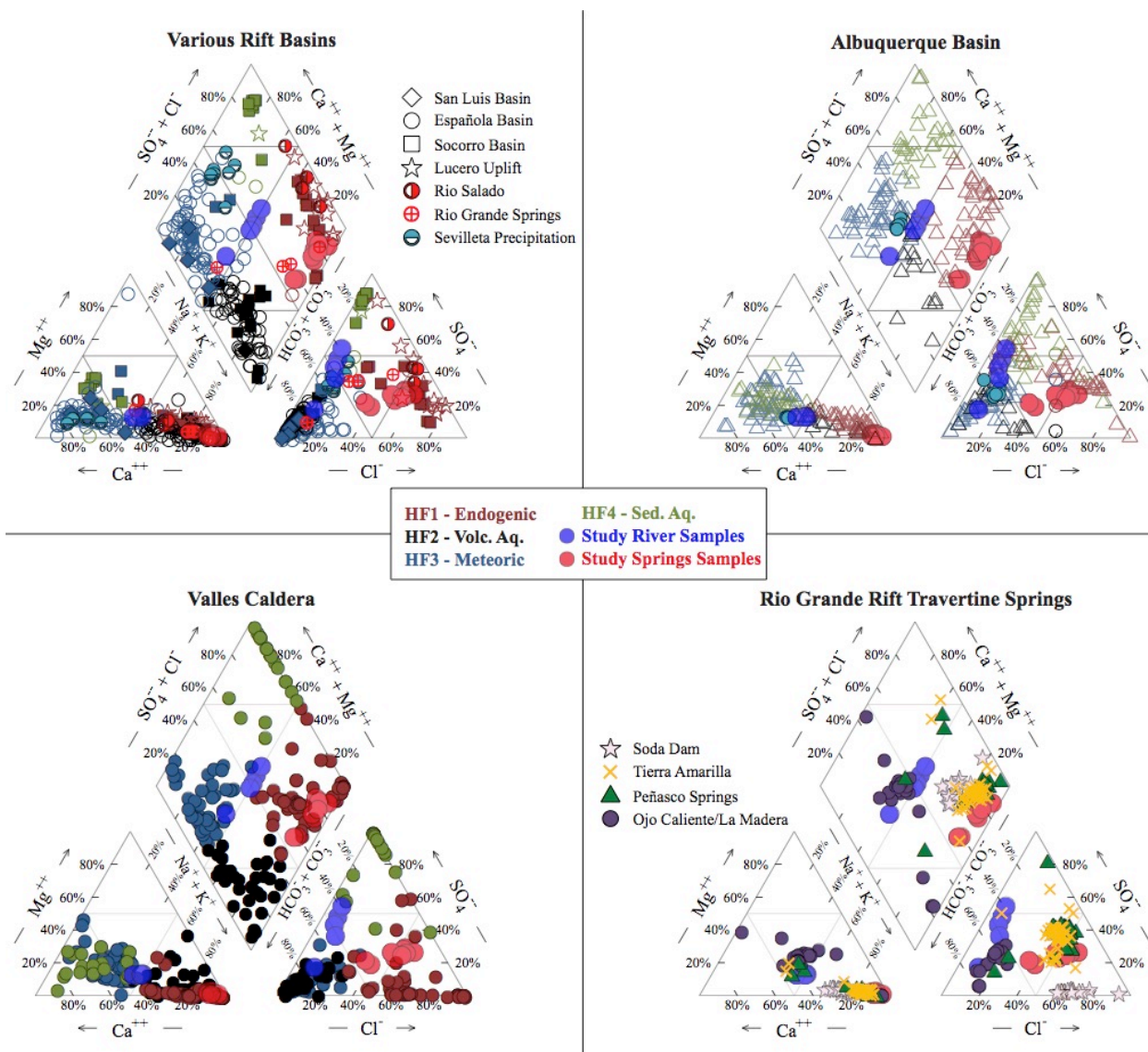


Figure 4.10 Piper diagram of water types from multiple studies of the Rio Grande rift. Color refers to which hydrogeochemical facies samples plot in (e.g. HF1-endogenic = red colors, HF2-volcanic = black colors, etc.) Shape refers to location. Top left: Water data from the San Luis, Española, and Socorro basin. HF1 facies tend to be located along the western margin of the Rio Grande rift (see Figure 9). Top right: Water data from the Albuquerque basin. HF1 facies are generally located near the western margin of the Rio Grande rift and along intrabasin faults near the western margin. Bottom left: Water data from Valles Caldera. HF1 data is from geothermal well data and from various springs of the Valles Caldera system. Bottom right: Travertine-precipitating springs of the Rio Grande rift. The majority of the springs plot in the HF1 facies with the exception of Ojo Caliente/La Madera springs, which have a bigger influence from meteoric fluids. Data from Goff and Shevenell, 1987; Crossey et al., 2011; Williams et al., 2013; McGibbon et al., 2018; Blomgren et al., 2019.

Appendix

Preliminary Case Study: Jornada Basin Pedogenic Carbonates

Introduction

The Rio Grande rift is dominated by arid and semi-arid climates, particularly in central and southern New Mexico, locally known as the Chihuahuan Desert. This region is characterized by low annual rainfall and high evapotranspiration rates, which result in increased water salinity and the precipitation of pedogenic carbonates in shallow soils of urban, rural, and undisturbed regions. In natural regions, pedogenic carbonates accumulate progressively into six morphological stages that are dependent on moisture content, Ca^{2+} concentration, and CO_2 influxes into soils (Tanner, 2010; Monger et al., 2015).

Consequently, studying accumulations of pedogenic carbonates has the potential to reveal paleo-environmental conditions during the formation of these carbonates. A large pedogenic carbonate horizon in the Jornada Basin near Las Cruces, New Mexico offers the perfect opportunity to learn about past climate conditions in the area (Figure 1). Previous studies have attempted to reconstruct paleo-climate conditions and carbonate formation rates in this area but those studies were considered preliminary in nature by the authors (Nyachoti et al., 2016).

More detailed and focused studies to link the formation of pedogenic carbonates to past water flow paths and fault zone locations are needed. In this study, we explore pedogenic carbonate formation in the Jornada Basin using U-series, ^{13}C , and ^{18}O methods to: 1) determine controls and rates of pedogenic carbonate formation and 2) reconstruct paleo-environmental conditions during the Quaternary. Five pedogenic carbonate samples were collected from a vertical profile, where the mound is thickest, for analyses. An additional sample was collected from a hand dug pit (~1 m below current exposure) to see how deeper carbonates vary. Aerial imagery was collected using a

DJI Mavic Pro to create a 3D model using AGIS Photoscan so that data collected from this mound have accurate vertical context.

Geologic Setting

The Jornada Basin is part of the Chihuahuan Desert and is located about 37 km northeast of Las Cruces, New Mexico (Figure 3). It consists of the Jornada Basin Long Term Ecological Research program, the Jornada Experimental Range, and the Chihuahuan Desert Rangeland Research Center, all of which aim to quantify the key factors and processes controlling ecosystem dynamics and patterns in the Chihuahuan Desert. These research areas are all adjacent to each other and are bounded by the Rio Grande river to the west, Dona Ana Mountains to the southwest, and the San Andres Mountains to the east. Tectonically, the Jornada Basin is within the physiographic provinces of the Basin and Range and Rio Grande rift. Both provinces consist of north-south trending mountain ranges, fault systems, and broad desert basins but Rio Grande rift activity is known to be the most influential active tectonism ongoing in the region (Seager et al., 1984; Mack et al., 1998). Rio Grande rift extension remains an important geologic process in the Jornada Basin today.

Our study site is located in the Jornada Experimental Range and consists of the La Mesa surface (5-0.8 Ma), which overlays the Camp Rice formation, in which many pedogenic carbonate horizons ranging from stage III (15-700 ka) to stage V (800 ka to 2 Ma) have developed (Figure 3; Monger et al., 2006). The study site consists of a previously excavated trench (15 m wide x 2.5 m deep) at the La Mesa surface, which exposes a pedogenic carbonate horizon. The pedogenic horizon is thickest at the center (~2 m), decreases in thickness to the sides suggesting possible surficial disturbance by erosion, sedimentation, or rooting and bioturbation (Nyachoti et al., 2016).

The pedogenic carbonate horizon is also extensively fractured and has an abrupt upper boundary with the topsoil, which consists of unconsolidated sandy sediments (~30 cm thick) and stage I carbonates. The sharp boundary is characterized by brittle to massively calcified, smooth micritic carbonate laminae (Robinson et al., 2015). In some areas, morphology of the pedogenic carbonate horizon is botryoidal suggesting possible growth into open space or more likely are evidence of dissolution pipes that have been partially infilled by round concretionary masses (pisoids) that cemented together by overlapping carbonate laminae (Robinson et al., 2015). The base of the pedogenic carbonate horizon is gradational into brecciated and friable stage III carbonates (~1 m thick) with pumice rich alluvium.

Preliminary Results

The U-series isotope signatures of pedogenic carbonates were derived from the typical isochron diagrams (e.g. Rosholt type or Osmond type; Ludwig, 2003). Five samples were dated but only three samples were within U-series range (Table 1; Figure 2). The two samples for which an age could not have been derived could be due to the samples being older than 600 ka (U-series age limit) or more likely, those samples contain too much detrital material, which did not allow for a measurable age. Ages vary from 16 ± 13 ka to 66 ± 0.02 ka with large errors associated (Table 1). The three dated samples do not follow a chronologic order. ^{13}C and ^{18}O isotope compositions (VPDB) range from about -5‰ to -3‰ and -8‰ to -5‰, respectively (Table 1).

Recommendation

Only three samples returned ages for this study. Ages were not in correct stratigraphic position, which is likely due to the complex cycling between precipitation and dissolution in pedogenic carbonates. Future work should focus on individual layers within collected samples instead of bulk analyses to get better results. Additionally, Sr isotopes and trace element chemistry

should be employed to get a better understanding on pedogenic carbonate formation in desert regions.

References

- Ludwig, K.R., 2003, Mathematical-statistical treatment of data and errors for Th-230/U geochronology. Uranium- Series Geochemistry, Reviews in Mineralogy and Geochemistry, 52: 631-656.
- Mack, G.H., Salyards, S.L., McIntosh, W.C., and Leeder, M.R., 1998, Reversal magnetostratigraphy and radio- isotopic geochronology of the Plio-Pleistocene Camp Rice and Palomas Formation, southern Rio Grande Rift, in Mack, G.H., Austin, G.S., and Barker, J.M., eds., 49th Field Conference Guidebook; Las Cruces Country II: Socorro, New Mexico Geological Society, p. 229–236.
- Monger, H. C., 2006, Soil development in the Jornada Basin. Structure and function of a Chihuahuan Desert ecosystem: The Jornada Basin Long Term Ecological Research site. Oxford Univ. Press, New York, 81-106.
- Monger, H. C., Kraimer, R. A., Cole, D. R., Wang, X., Wang, J., 2015, Sequestration of inorganic carbon in soil and groundwater. *Geology*, 43(5), 375-378.
- Nyachoti, S.K., 2016, Application of uranium and strontium isotopes as salinity and paleo-environmental conditions tracers: Insight from the Rio Grande River and pedogenic carbonates in drylands soils of Southwest, USA. The University of Texas at El Paso.
- Robins, C.R., Deurlington, A., Buck, B.J. and Brock-Hon, A.L., 2015, Micromorphology and formation of pedogenic ooids in calcic soils and petrocalcic horizons. *Geoderma*, 251, pp.10-23.

Seager, W.R., Shafiqullah, M., Hawley, J.W., and Marvin, R.F., 1984, New K-Ar dates from basalts and the evolution of the southern Rio Grande rift: Geological Society of America Bulletin, v. 95, p. 87-99.

Tanner, L., 2010, Continental carbonates as indicators of paleoclimate. Developments in sedimentology, 62, 181 – 188. ISSN 0070-4571, DOI 10.1016/S0070-4571 (09) 06204-9

Tables and Figures

Table 1. Isotope and Age Summary Table.

DATA OF DATED JORNADA SAMPLES

Sample Number	$(^{234}\text{U}/^{238}\text{U})_{\text{Initial}}$	±	Age (ka)	±	d 13C (VPDB)	d13C/12C (Std Dev)	d 18O (VPDB)	d18O/16O (Std Dev)
J1	1.43	0	66	0.02	-3.81	0.01	-7.01	0.02
J2	1.6	0.61	16	13	-3.70	0.01	-7.37	0.01
J3	-	-	-	-	-4.02	0.01	-6.94	0.01
J4	-	-	-	-	-	-	-	-
J5	1.30	1.500	44	270	-4.41	0.02	-6.73	0.02
J6	-	-	-	-	-2.50	0.02	-7.26	0.01
J7	-	-	-	-	-3.71	0.01	-5.78	0.01

Note: Minus sign (-) = No data due to sample being out of U-series dating range

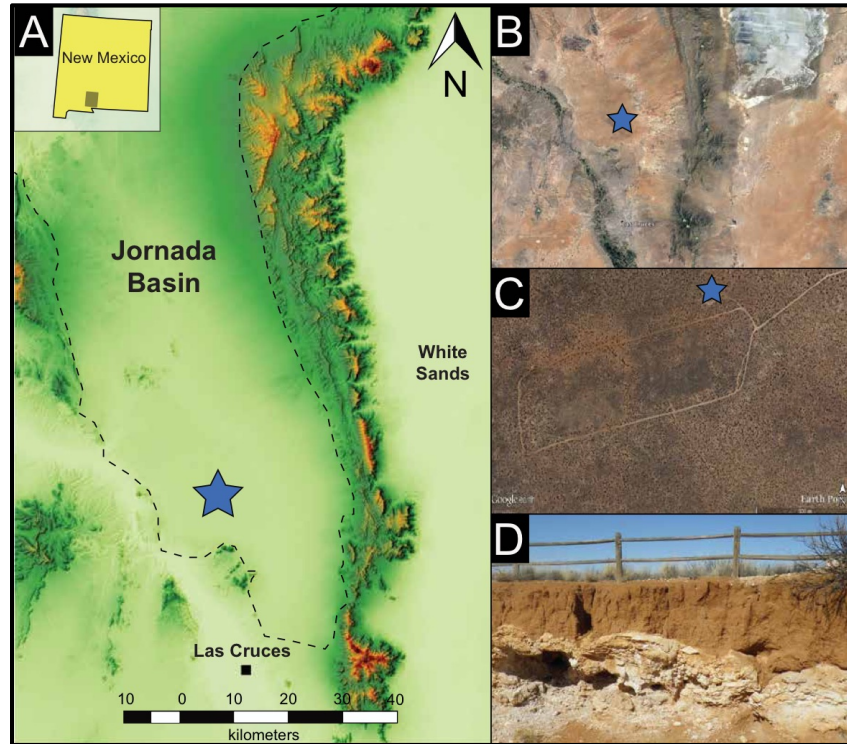


Figure 1. A) Digital elevation model of the Jornada Basin. Blue star = study area. B) Google earth image of study area. Note White sands in the top right corner. C) Zoomed in Google Earth image of study site in the Jornada Basin. D) Pedogenic carbonate horizon.

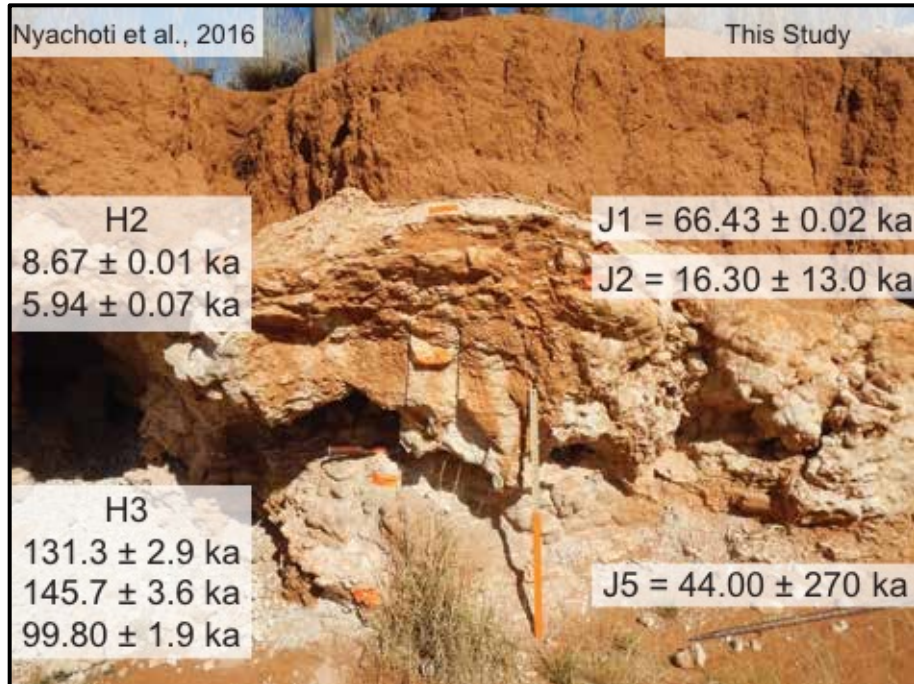


Figure 2. Pedogenic carbonate horizon from the Jornada Basin. Orange tape shows locations where we collected samples from in this study. Ages, on right side, correlate with location in which samples were collected from. Samples J3 – J4 did not give an age likely due to being out of U-series range. Ages on the left are from Nyachoti et al., 2016.

Vita

Victor Higareda Garcia was proudly raised in Montana Vista, Texas and completed his Bachelor of Science degree in Geological Sciences at the University of Texas at El Paso (UTEP) in 2014. He then completed his Master of Science degree in Geosciences at the University of Arizona in 2016. Victor then enrolled at his undergraduate alma mater to pursue a doctoral degree in Geological Sciences. During his time at UTEP, Victor mentored many undergraduate students, was deeply involved in community outreach, and was the recipient of multiple scholarships and awards, culminating with the prestigious Natalicio Dissertation Fellowship for academic year 2019-2020. Victor completed his doctoral degree in June 2020 and looks forward to the next chapters of his life.

Contact Information: vhgarcia4@gmail.com